Christian-Albrechts Universität zu Kiel
Institut für Theoretische Physik und Astrophysik

Diploma thesis

First-principle simulation of classical charged particles in traps

Hanno Kählert

Kiel, October 2008

Supervisor/1st examiner: Prof. Dr. Michael Bonitz

2nd examiner: _____

Contents

1. Introduction

1.1. Topics and goal of the thesis

Charged particles are omnipresent in nature – from plasmas in the sun, the solar wind, the interstellar medium and the ionosphere to lightning and the polar lights. Most often they are unconfined and occur in astronomically large numbers in gaseous form. In this thesis the focus lies on *small* systems of equally charged particles (one-component plasma, OCP) confined by an external potential well.

The typical particle numbers range from approximately ten to only a few hundred. The considered systems show finite size effects and, compared to large systems, their properties strongly depend on the exact particle number. In addition the particles are confined by an external trapping potential whose form also affects the physics. Examples for these systems include

- electron-hole bilayers,
- cold ions in Paul or Penning traps,
- dusty plasmas.

An important aspect of this work is strong correlation effects. In conventional plasmas the particles often have a high kinetic energy and can be treated as an ideal gas. For laser cooled ions, to name one example, this is not true. Even though the ions interact through the Coulomb potential the physics of these systems strongly differs from that of a hot plasma. Instead of being in a gaseous state these systems occur as strongly coupled liquids or even form crystalline structures.

While for weakly coupled systems analytical methods can often be employed, this is usually not the case for strongly correlated systems. One thus has to refer to numerical methods such as molecular dynamics or Monte Carlo simulations which have become increasingly important with the availability of low cost computer power in the last decade(s). They are able to treat the interaction between the particles from first principles and are not restricted to approximate solutions.

The main part of this thesis is devoted to dusty plasmas. This relatively new field of plasma physics allows one to directly study strongly correlated charged particles in laboratory experiments and track the motion of single particles with standard video microscopy. This allows for a detailed microscopic investigation and yields, at least in principle, the position-velocity distribution function $f(\mathbf{r}, \mathbf{v}, t)$ in phase space. A better understanding of these systems could also lead to progress in the research on other

strongly correlated systems where direct observation methods are not feasible. This is the reason why dusty plasma physics has attracted considerable attention.

An important experiment in this field was performed at the Institute for Experimental and Applied Physics at the University of Kiel in 2004 [1]. For the first time it was possible to create spherical three-dimensional dust crystals without void regions or chain-like order. The observed shell structures were similar to those of trapped ions.

The goal of this work is to use numerical methods for the description of dust particles in an external confinement and to understand and explain recent experimental observations regarding the crystallization of the particles, especially the observed shell structures. While these systems are well described by means of first-principle molecular dynamics simulations, an accurate description in terms of a shell model has only been achieved for systems with Coulomb interaction (e.g. trapped ions) so far. For dusty plasmas such a model has recently been proposed [2] and will be investigated here.

Another goal is a deeper understanding of the processes and mechanisms that determine the stationary state probabilities of dusty plasma crystals, which have recently been measured in experiments [3]. Even though the results have been compared to molecular dynamics simulations, no theoretical explanation has been given. Here this question is addressed with both, simulations and an analytical method. The analysis aims at finding the relevant parameters that determine the results and an explanation for the unexpectedly high occurrence of metastable states.

1.2. Outline

This thesis is organized as follows:

Chapter 2 gives an introduction to the physics of strongly coupled charged particles and a brief historic review on the creation of dust crystals in laboratory experiments. The charging of dust particles and their mutual interaction in a plasma environment is discussed as it will be important for the theoretical model used in this work. Additionally the experimental setup for producing spherical dust crystals is introduced to establish a link between the experiments on the one hand and the present theoretical work on the other hand. Special attention is paid to the observed shell structures.

Chapter 3 deals with the theoretical model the analysis in this thesis is based on and reviews some recent theoretical results. The required simulation methods are discussed in Chapter 4. Among them are classical molecular dynamics, which is ideally suited to investigate time dependent and dynamical quantities, and classical Monte Carlo, typically used to study equilibrium properties. Here it is primarily used for minimization purposes. As a third method Langevin dynamics is discussed which serves as a tool for investigating dissipative systems such as the dust particles considered here.

Results are discussed in Chapters 5–7. A shell model for spherical dust balls is introduced in Chapter 5. It is investigated with respect to its capability to reproduce the

exact results obtained in molecular dynamics simulations. Especially the radii of the shells and their occupation numbers are compared.

Chapter 6 is concerned with the probability of metastable states in Yukawa balls. The model system is extended to account for friction effects as they occur in dusty plasmas. The effects of friction, screening and temperature on the probabilities are discussed in detail. A simple analytical model is employed to give a physically intuitive explanation for the results. The connection between the analytical model and the molecular dynamics simulations is established by resorting to the time evolution of the velocity distribution function.

Chapter 7 discusses and reviews some of the aspects that are associated with the eigenfrequency spectrum of strongly correlated systems in the presence of friction. Especially the Fourier spectrum of undamped and damped systems is compared.

The last chapter summarizes the results of this work followed by some remarks on unsolved problems, possible improvements of the model and an outlook on future work.

The appendix gives some details on the calculation of the shell radii in the Yukawa shell model and the derivation of the analytical model used in Chapter 6.

2. Classical charged particles in traps

2.1. Strongly coupled Coulomb systems

In the last decades strongly coupled Coulomb systems have been of great interest in many fields, e.g. Z-pinches, inertial confinement fusion or electrons at the surface of liquid helium, for an overview see Ref. [4]. This chapter discusses some of the main aspects of strongly coupled Coulomb systems and specifically the physics of dusty plasmas.

Classical plasmas are characterized by the dimensionless coupling parameter

$$\Gamma = \frac{|\langle U_{\text{corr}} \rangle|}{k_B T} \sim \frac{Q^2}{\langle r \rangle k_B T}, \tag{2.1}$$

which determines whether a system is strongly or weakly coupled. Here k_B denotes Boltzmann's constant, T the temperature, Q the particles' charge and $\langle r \rangle$ their mean separation. In a strongly coupled system the average correlation energy U_{corr} exceeds the thermal energy $k_B T$, i.e. $\Gamma > 1$, whereas in a weakly coupled system $\Gamma < 1$. The required coupling parameter at which crystallization occurs depends on the specific system at hand. For a macroscopic 3D one-component plasma the phase transition occurs at $\Gamma \approx 175$ [5], while in 2D a coupling strength of $\Gamma \approx 137$ is sufficient [6]. For small systems with only ten to a few hundred particles finite size effects can strongly influence the stability and melting points of crystals [7]. Especially so called 'magic' clusters with a high symmetry often have an unusually high melting temperature.

While in weakly coupled systems it is often sufficient to treat the particle-particle interaction approximatively, this is not possible in the strong coupling limit. Instead of starting with the ideal gas (i.e. $\Gamma = 0$), often used as a model system for a hot plasma, one may consider the opposite limit of infinite coupling ($\Gamma \to \infty$). In this situation the (classical) particles are located at their equilibrium positions and small oscillations can be introduced via the harmonic approximation of the potential, for which many analytical results are known. Thus strongly coupled Coulomb systems resemble plasmas on the one hand, due to their Coulomb interaction, but on the other hand also have similarities with systems in the solid state, where the second method is often employed for the study of lattice vibrations. If none of the two approaches can be used, numerical simulations come into play which can handle arbitrary coupling strengths. In the frame of this work it turned out that the combination of both techniques yields reliable results on the one hand and a deeper understanding of the underlying physics on the other hand.

Coulomb crystals

One of the first works on Coulomb crystal formation was published by Wigner in 1934 [8], who predicted that electrons in a solid would form a body-centered cubic (bcc) lattice if they had no kinetic energy. More recent examples for systems with strong Coulomb interaction include ion crystals in Paul or Penning traps, which have been observed in Refs. [9, 10]. Here lasers are used to cool ions to temperatures of a few mK where strong correlation effects dominate over thermal fluctuations and crystallization becomes feasible. The number of ions can vary from only a few to tens of thousands. In Ref. [10] shell structures were found which agreed well with theoretical predictions.

Further examples include electrons in quantum dots [11], electron-hole bilayers [12] and dusty plasmas [1]. In this work the emphasis is laid on finite classical systems in external traps when quantum effects are negligible. While the major part is devoted to dusty plasmas, the results are also relevant for ion crystals in the appropriate limits of the model parameters.

In the following the physics of dusty plasmas will be considered in more detail.

2.2. Dusty plasmas

2.2.1. Introduction

In contrast to conventional plasmas consisting of ions, electrons and neutral gas particles, dusty (or complex) plasmas contain a fourth particle species which is referred to as the 'dust' component. Besides laboratory experiments dusty plasmas widely occur in nature, e.g. astrophysical systems such as planetary rings [13] or cometary tails [14]. In the microchip industry dust particles can be a serious problem in the plasma production processes.

While the crystallization of the dust subsystem was predicted theoretically in 1986 by Ikezi [15], the first observations of dusty plasma crystals in laboratory experiments were reported almost ten years later in 1994 by Chu and I [16], Thomas et al. [17] and Melzer et al. [18]. They were able to produce two-dimensional crystals in radio frequency (rf) discharges. These findings had a dramatic impact on the research on dusty plasmas.

In experiments the dust typically consists of μm sized particles and has a mass being much higher than that of the ions. This makes dusty plasmas an ideal system for studying dynamical properties in the strong coupling limit, since their motion occurs on a 'macroscopic' timescale and can be recorded with ordinary video microscopy. While ions must be cooled to temperatures in the mK regime for crystallization to occur, dust crystals can be observed at room temperature. The reason for this is their much higher charge of thousands of electrons, which may give rise to a coupling parameter $\Gamma \gg 1$ even at $T \approx 300\,\mathrm{K}$.

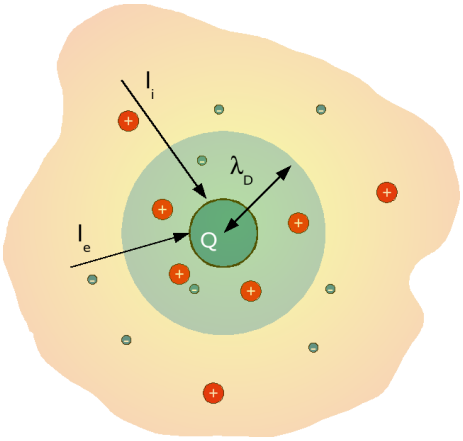

Figure 2.1.: *Illustration of a dust particle immersed in a plasma. The negatively charged grain is surrounded by a cloud of positive ions and negative electrons shielding the bare Coulomb potential. The grain charge is determined by the ion and electron currents $I_{i,e}$. The Debye length λ_D indicates the effective range of the dust potential.*

2.2.2. Grain charging

Due to the high mobility of the electrons (compared to ions) in the plasma the dust rapidly acquires a high negative charge Q of thousands of elementary charges. A simple theory of the charging process that calculates the ion and electron currents to the grain is the OML (orbit motion limited) theory, for a recent overview see Ref. [19]. Its main assumptions are the conservation of energy and angular momentum and that every electron or ion hitting the grain surface will be absorbed. Goree stated the conditions for its applicability as $a \ll \lambda_D \ll l_{e,i}$ [20], where a is the grain radius, λ_D the screening length (see next paragraph) and $l_{e,i}$ the electron (ion) mean free path. Furthermore it is assumed that the grain is isolated in a sense that it does not affect the orbits of electrons and ions in its vicinity [4], i.e. the dust density is low. Another mechanism that could be relevant for the grain charge in the presence of an external source of radiation is photo-emission of electrons [19]. For an illustration of the charging process see Fig. 2.1.

2.2.3. Electrostatic potential

The surrounding plasma environment changes the (effective) electrostatic potential of the dust particles from a bare Coulomb potential $\Phi_C(r) = Q/r$ to a *screened* Coulomb (Yukawa) potential

$$\Phi_Y(r) = \frac{Q}{r} e^{-\kappa r}, \tag{2.2}$$

if dynamical screening and nonlinear effects are neglected. Instead of the screening parameter κ the Debye length λ_D is often used to denote the screening strength. The two parameters are simply related by $\kappa = \lambda_D^{-1}$.

This form of the interaction potential can be derived from Poisson's equation

$$\Delta\Phi = -4\pi e(n_i - n_e) - 4\pi Q\delta(\mathbf{r}) \tag{2.3}$$

for a single test charge Q embedded in a plasma with electron density n_e, ion density

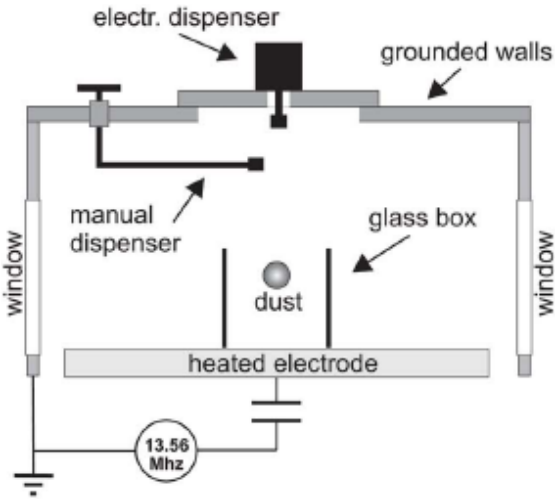

Figure 2.2.: *Sketch of the experimental setup used to create spherical dust balls. The dust is confined in a glass box on the lower electrode. Particles can be injected from the top of the setup from a dust dispenser. From Ref. [25].*

n_i and the corresponding temperatures $T_{e,i}$. Assuming a Boltzmann distribution for electrons and (singly charged) ions, $n_{e,i} = n_0 e^{\pm e\Phi(r)/(k_B T_{e,i})}$, and linearizing the densities according to $n_{e,i} \approx n_0[1 \pm e\Phi(r)/(k_B T_{e,i})]$ yields the (linearized) Poisson equation for the potential $\Phi(r)$. The electron and ion densities far away from the dust grain are denoted by n_0 and are assumed to be equal. This procedure requires the condition $|e\Phi/k_B T_{e,i}| \ll 1$ to be fulfilled.

The solution is given by Eq. (2.2) and the screening parameter can be determined from the plasma parameters according to

$$\kappa^2 = \lambda_D^{-2} = \frac{4\pi n_0 e^2}{k_B}\left(\frac{1}{T_e} + \frac{1}{T_i}\right) = \lambda_{De}^{-2} + \lambda_{Di}^{-2}. \tag{2.4}$$

In experiments κ is mostly determined by the inverse ion Debye length, $\kappa^{\mathrm{exp}} \approx \lambda_{Di}^{-1}$, since the electron temperature is usually much higher than that of the ions. As it is difficult to determine the screening parameter in the experiments, κ must be determined from a comparison with the simulation results. Besides dusty plasmas Yukawa interaction can also be found in colloidal suspensions [21].

Other forms of the interaction potential and their influence on dust crystallization have been widely discussed in the literature, e.g. Refs. [22–24]. Especially the effect of streaming ions creating an attractive wakefield potential and ion focusing effects have been of great interest. In the experiments of Ref. [3], to which the results of this thesis will specifically be compared, the clusters are well described by simple Debye screening. There the effect of streaming ions is negligible since the dust levitates high above the lower electrode (the experimental setup is shown in Fig. 2.2) where the electric field is weak and the ion flow subsonic. In addition no vertical chains have been observed which typically occur in experiments with strong ion flows [25]. Thus the use of the isotropic Yukawa potential is well justified. Collective effects arising from the presence of other grains are not included in this model since they do not play a significant role here.

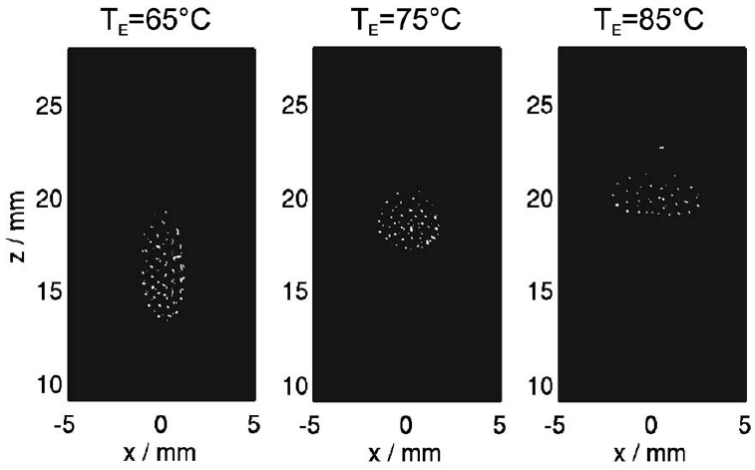

Figure 2.3.: *Vertical section through a confined Yukawa ball at different temperatures T_E of the lower electrode. The structure changes from prolate to oblate as the temperature is varied. From Ref. [25].*

In fact the charging process and the grain potential are closely related and influence each other. This problem is still an issue of current research [19].

2.2.4. Experiments

Dust confinement and recording

While the first experiments with dusty plasmas produced 2D monolayer crystals, the formation of 3D crystals posed a greater challenge. Usually the dust resides above the lower electrode in an rf discharge, where the vertical gravitational force is balanced by an electric field. Even though multilayered 2D crystals with attractive forces between the layers could be observed [26], real 3D crystals always had to struggle with gravity pushing the particles towards the lower electrode.

In microgravity experiments [27] or laboratory experiments where a thermophoretic force was used to compensate gravity [28], the formation of three-dimensional clusters was hindered by the occurrence of voids in the center region of the dust cloud. The breakthrough in producing spherical, three-dimensional clusters with many particles was achieved in 2004 by Arp et al. [1, 25] who used a combination of thermophoretic force and dielectric walls to confine the dust. The experimental setup is shown in Fig. 2.2.

The experiment is conducted in a capacitively coupled rf discharge [25]. Argon gas is used with a typical pressure of $20 - 120\,\mathrm{Pa}$. Windows in the side walls allow for a direct observation of the injected dust particles. The lower electrode can be heated to create a temperature gradient and thus a thermophoretic force in the vertical direction. Together with the electric field it compensates the gravitational force. A glass box is placed on the lower electrode in which the dust balls are confined. On the one hand it serves as a plasma loss area and therefore the net plasma production in the box is minimal [25]. This effectively suppresses the formation of voids due to outward streaming ions. On the other hand a sheath is formed in front of the walls with an electric field that adds to

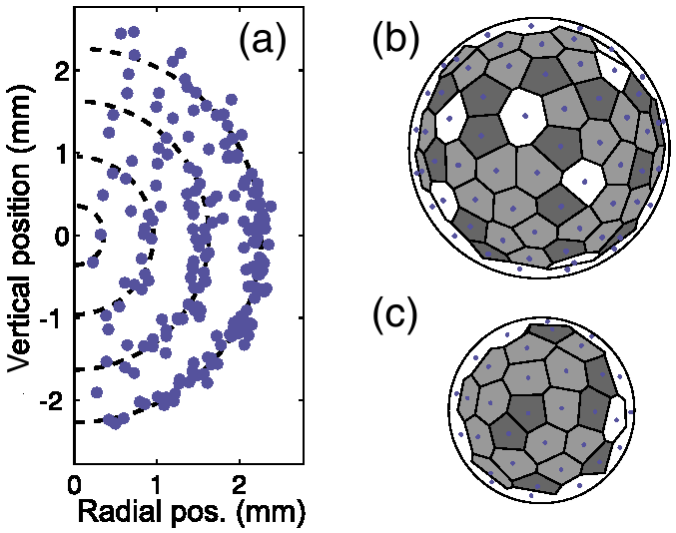

Figure 2.4.: *Experimental cluster with $N = 190$. In a) the particles are projected into the (ρ, z) plane (cylindrical coordinates). Parts (b) and (c) show a bottom view of the two outer shells together with a Voronoi cell analysis. Hexagons and pentagons are indicated by light gray and dark gray, respectively. From Ref. [1].*

the horizontal confinement of the dust cloud. The ion-drag force is more than two orders of magnitude smaller than the electric field force and does not influence the topology of the trap. The overall confinement was shown to be parabolic and almost isotropic [25].

In the experiments it is possible to record the motion of single dust particles and obtain their trajectories $\{\mathbf{r}_i(t)\}$. One therefore has the complete phase space information which allows for the study of dynamical quantities such as normal mode excitations or wave phenomena. While in the first experiments standard video microscopy was used [25], more sophisticated monitoring methods are based on stereoscopy [3].

The particles are found to arrange themselves in a nested shell structure very similar to that of trapped ions, but with different shell occupation numbers. Examples are shown in Fig. 2.3 and Fig. 2.4. On the shells the particles mostly have five or six neighbors (pentagons and hexagons) but also defect structures with seven neighbors can be observed.

3. Theoretical model

3.1. Hamiltonian

The theoretical model used throughout this thesis aims at describing the dust balls found in the experiments of Ref. [1]. The Hamiltonian for this system consists of the kinetic energy part, the external confinement and the interaction between the particles.

As was pointed out before, the external confinement for the experiments performed in Kiel was shown to be isotropic and harmonic [25]. The interaction between the dust particles in a plasma is approximately given by the Yukawa potential (2.2). Then the Hamiltonian for the system of N equal dust particles with charge Q and mass m reads

$$H = \sum_{i=1}^{N} \left\{ \frac{p_i^2}{2m} + V_{\text{ext}}(r_i) \right\} + \sum_{i>j}^{N} V(|\mathbf{r}_i - \mathbf{r}_j|), \tag{3.1}$$

where

$$V_{\text{ext}}(r) = \frac{m}{2}\omega_0^2 r^2 \tag{3.2}$$

is the external confinement potential and the interaction potential is given by

$$V(r) = \frac{Q^2}{r} e^{-\kappa r}. \tag{3.3}$$

Despite its simplicity this model is of relevance for many systems, such as colloids, and has proven to accurately describe the spherical dust crystals (Yukawa balls) observed in experiments [29]. If the Yukawa potential is replaced by a bare Coulomb potential the model can also be used to study ions in external traps.

3.2. Dimensionless units

The Hamiltonian (3.1) appears to involve a wide number of parameters, namely the charge Q, mass m, trap frequency ω_0 and the screening parameter κ. In fact, the number of variables can be reduced to only one by introducing dimensionless units.

An energy scale can easily be obtained by equating the external confinement energy and the bare Coulomb interaction between two particles, i.e. $\frac{m}{2}\omega_0^2 r_0^2 = \frac{Q^2}{r_0}$. From this expression one derives the length unit $r_0 = \sqrt[3]{\frac{2Q^2}{m\omega_0^2}}$, which denotes the stable distance

Table 3.1.: *Overview on the system of units used throughout this work.*

distance r_0	$\sqrt[3]{2Q^2/m\omega_0^2}$	energy E_0	Q^2/r_0
temperature T_0	E_0/k_B	time t_0	ω_0^{-1}
force F_0	$m\omega_0^2 r_0$	screening parameter κ_0	r_0^{-1}

between two particles in the absence of screening, and the corresponding energy unit $E_0 = Q^2/r_0 = \frac{m}{2}\omega_0^2 r_0^2$. The inverse trap frequency is a convenient time unit $t_0 = \omega_0^{-1}$. Forces will be given in units of $F_0 = m\omega_0^2 r_0$, while the unit of temperature is closely related to the unit of energy by $T_0 = E_0/k_B$. The system of units is summarized in Table 3.1.

By performing the transformation $H \to H/E_0$, $r \to r/r_0$, $\kappa \to \kappa r_0$, $p \to p/(mr_0\omega_0)$ the Hamiltonian (3.1) can be recast in the form

$$H = \sum_{i=1}^{N} p_i^2 + \sum_{i=1}^{N} r_i^2 + \sum_{i>j}^{N} \frac{e^{-\kappa|\mathbf{r}_i - \mathbf{r}_j|}}{|\mathbf{r}_i - \mathbf{r}_j|}. \tag{3.4}$$

The only remaining parameter is the screening parameter κ. Since it cannot be measured in the experiments directly it must be chosen to match the experimental results. The other parameters such as mass or charge only determine the scaling of the variables but are completely eliminated from the problem otherwise.

3.3. Review of recent results

Ground states and influence of screening

The Hamiltonian (3.1) has been widely studied in the literature. A detailed analysis of the ground states of 3D Coulomb clusters was presented in Refs. [30, 31]. Besides the ground state also metastable states with a slightly larger energy were found in the simulations [30–32]. Furthermore a fine structure was observed, i.e. states with the same number of particles on the shells, but with a different arrangement on the same shell [30]. The eigenfrequency spectrum of Coulomb and Yukawa balls has been studied extensively in Ref. [32].

The ground states of small spherical Yukawa clusters for a wide range of the screening parameter can be found in Ref. [33]. It was shown that the ground state configuration strongly depends on the screening parameter, cf. Fig. 3.2. The general trend is that with increased screening particles move from outer to inner shells. Upon increase of the particle number the additional particle usually goes to one of the existing shells or moves into the center. However, there are a few exceptions to this behavior. Three kinds of anomalies have been identified (cf. Fig. 3.2):

1. Correlated two-particle transitions (increase of the particle number leads to a structural transition involving two particles).
2. Reduction of inner shell population upon increase of N.
3. Reentrant shell transition upon increase of κ (a previous ground state at lower κ reappears at a higher screening parameter).

In Refs. [29, 34] the influence of screening has been studied by considering the two-particle system. It was shown that the ground state distance r_κ is a monotonically decreasing function of the screening parameter. This is in agreement with the observation that increased screening leads to a compression of the clusters.

Expanding the potential energy around the equilibrium positions to second order one obtains a local trap frequency Ω with

$$\Omega^2(\kappa) = \frac{6}{m}\frac{Q^2}{r_\kappa^3} f_2(\kappa), \tag{3.5}$$

$$f_2(\kappa) = e^{-\kappa r_\kappa}(1 + \kappa r_\kappa + \kappa^2 r_\kappa^2/3). \tag{3.6}$$

The variance of the particle distance fluctuations for two particles was shown to be $\sigma_r = \sqrt{\frac{2k_BT}{m\Omega^2(\kappa)}}$, which leads to the conclusion, that the shell width grows with temperature as $\sqrt{T}$, while screening reduces the shell width [29, 34]. However, the distance between the shells also decreases with κ, which is the reason why screening effectively destabilizes the clusters against melting since transitions between shells become more likely.

Compared to Coulomb systems, where the coupling parameter Γ_C is defined by Eq. (2.1), Yukawa systems interact with a *screened* Coulomb potential and their coupling parameter has to be modified accordingly. Instead of simply adding the Yukawa factor $\mathrm{e}^{-\kappa r}$, the authors of Ref. [29] proposed

$$\Gamma_\kappa = \Gamma_C f_2(\kappa), \tag{3.7}$$

which is related to the relative distance fluctuations of the two-particle system by

$$u_r^2 = \frac{\sigma_r^2}{r_\kappa^2} = \frac{1}{3}\frac{1}{\Gamma_\kappa} \tag{3.8}$$

and is very similar to that of the macroscopic Yukawa system [35].

Melting

Since the considered systems consist of only ten to a few hundred particles their properties are strongly influenced by finite size effects. This is especially apparent when one considers the cluster stability. There exists a number of so-called 'magic' clusters with highly symmetric configurations that have very high melting points, see Fig. 3.1. This

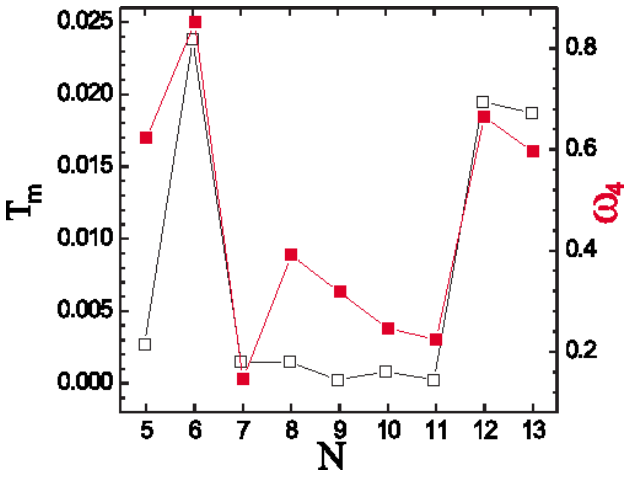

Figure 3.1.: *Melting temperatures for the first melting process in small Coulomb balls (left axis, black open squares) and lowest nonzero eigenfrequency (right axis, red filled squares) for systems with 5 to 13 particles. From Ref. [36].*

issue has been studied in detail in Ref. [36]. The magic clusters were identified as those with $N = 6, 12, 13$ and $N = 38$ particles. The melting process mainly evolves through two different mechanisms: intrashell melting and radial melting. An intermediate process has been found for the magic cluster with 38 particles. For clusters in an anisotropic confinement the melting process was found to be inhomogeneous and depends on the spatial location of the particles in the cluster [37].

Analytical results for the density profile

An analytical theory for confined Yukawa systems has been developed in References [2, 38]. Compared to Coulomb systems, which have a constant radial density profile in a parabolic confinement, Yukawa systems exhibit a parabolically decreasing profile with the highest density in the center of the trap. These results have been obtained in a mean field approach neglecting correlation effects [2]. While the agreement with exact results from molecular dynamics simulations is very good for low screening, deviations occur for larger values of κ. In this case the density profile is well described by the local density approximation (LDA) [38]. In both cases the density in the trap center is increased upon increase of κ which is in agreement with the higher population of inner shells as was observed in finite crystals.

Further details can be found in the cited papers and the references therein.

Comparison with Lennard-Jones clusters[1]

The main difference between Lennard-Jones (LJ) clusters and Yukawa balls is the nature of the interaction potential. While particles with the purely repulsive Yukawa interaction necessarily require an external confinement to form crystals, this is not true for the LJ

[1] This discussion is published in Ref. [33]

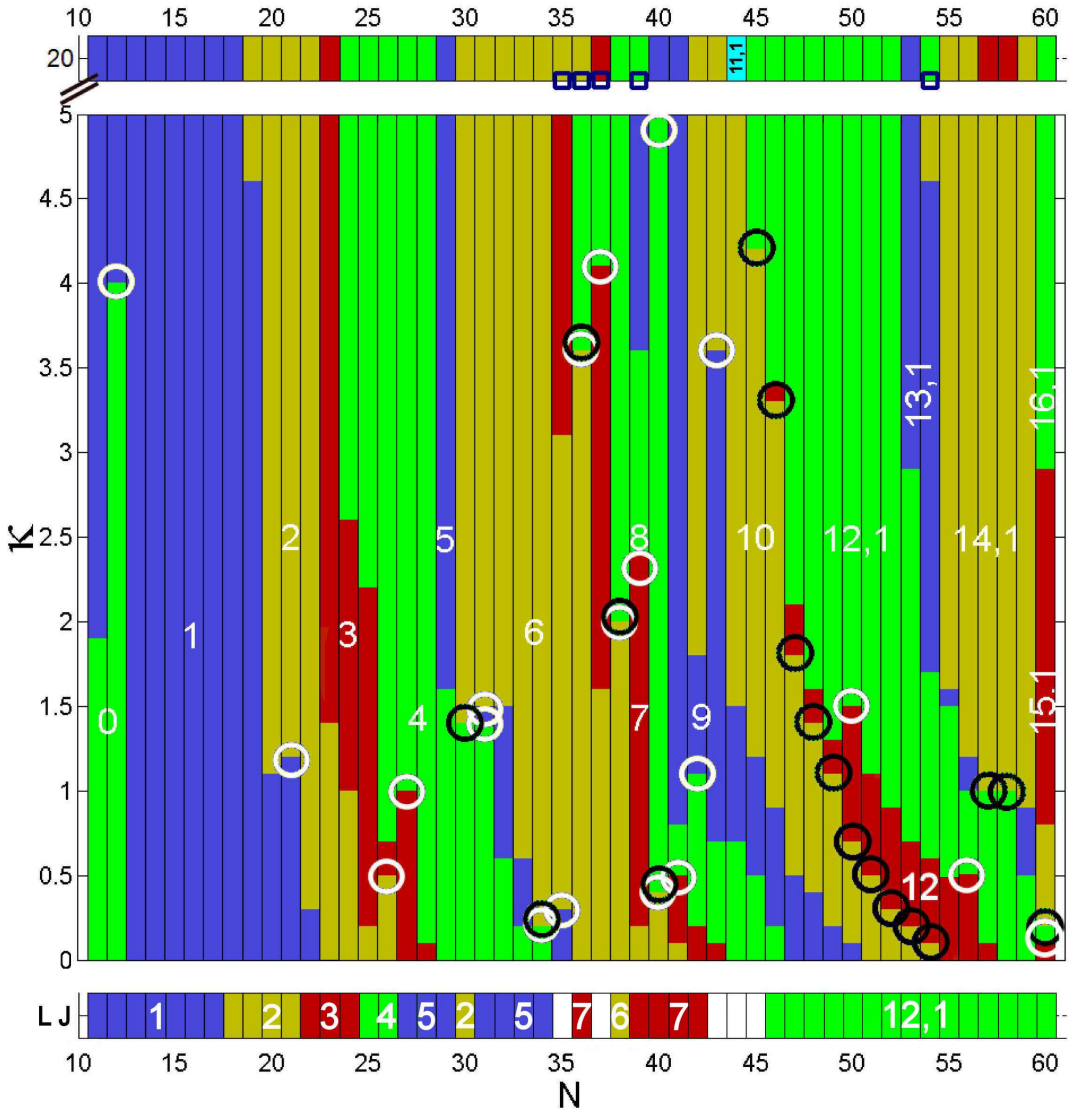

Figure 3.2.: *Ground states of Yukawa balls for a screening parameter* $0.0 \leq \kappa \leq 5.0$ *and particle numbers* $11 \leq N \leq 60$. *The white numbers denote the number of particles on the inner shell(s). The black circles indicate anomalies of the 1st kind. The white circles denote the end of the screening range, where anomalies of the 2nd kind appear. The ground states for a screening parameter* $\kappa = 20.0$ *are plotted above the diagram. The cyan bar for* $N = 44$ *at* $\kappa = 20.0$ *refers to a ground state of* $(11, 1)$ *in the center region. The dark blue squares just below* $\kappa = 20.0$ *indicate anomalies of the 3rd kind, where a ground state configuration reappears with increased screening. For comparison the ground state configurations for Lennard-Jones (LJ) interaction are plotted below the diagram, where possible. In the cases* $N = 35, 37, 43 - 45$ *it is not possible to define radial shells in the LJ systems. From Ref. [33]*

potential as it has an attractive tail. The ground states of LJ clusters have been studied extensively and are summarized in Ref. [39] for $N \leq 110$.

In contrast to Yukawa balls which always have a shell structure, the form of LJ clusters is somewhat different [33]. For most $N \leq 60$ the global minimum consists of a Mackay icosahedron surrounded by a low energy layer of the remaining particles [39]. Closed shells are observed for $N = 13$ and $N = 55$ with an icosahedral structure and a particle in the center of the cluster. Compared to Yukawa balls, where adding one particle to a closed-shell configuration leads to a new *inner* shell, adding one particle here often gives rise to a new *outer* 'shell'. This is the reason why the first closed-shell configuration is found for $N = 13$ (LJ) – with a particle in the center, while Yukawa balls have their first closed-shell configurations for $N = 11$ or $N = 12$ (depending on κ) – without a center particle. The same behavior is found for the second closed-shell configuration with $N = 55$ (LJ), which is never observed for Yukawa balls with this particle number.

In Fig. 3.2 only the innermost shells of LJ systems are shown where a shell determination is possible. The particles of clusters without closed-shell configurations are not uniformly distributed on the shells. As an example consider the transition $N = 13 \rightarrow 14$. The 14th particle is not added to the first shell but is attached to the surface of the $N = 13$ cluster and forms a new outer 'shell' with an occupation number of one. In the case of Yukawa balls the additional particle would generally open a new inner shell (center particle) or would be added to one of the existing shells. The positions of the particles on this shell would be changed such that the particles stay as far away from each other as possible, with the strongest tendency for Coulomb interaction and a diminishing effect for larger κ. A single particle on an outer shell is unfavorable due to the symmetry of the trap and the purely repulsive forces. A trend similar to LJ clusters is only observed for very high κ where sub-shells can be found with an occupation number higher than those of nearby outer shells. It would be interesting to analyze the effect of an external trap on the structure of LJ clusters without closed-shell configurations to further investigate the influence of a confinement on the emergence of shells as found in Yukawa balls.

4. Simulation methods for classical particles

4.1. Relations to Statistical Physics

In Statistical Physics thermodynamic averages are obtained by averaging a quantity A over independent realizations of the same system. To describe different situations of interest there exist various ensembles for which certain parameters are fixed. Among them, two often employed ensembles are the microcanonical and the canonical ensemble.

The former describes an isolated system of N particles at constant total energy E. The fundamental hypothesis of Statistical Physics is that for a closed system in equilibrium, every microstate s, in the classical case defined by the particles' positions $\{\mathbf{r}_i\}$ and momenta $\{\mathbf{p}_i\}$, has the same probability. The equilibrium state is defined as the state in which the distribution of states does not change with time and consequently macroscopic quantities remain constant [40].

In the canonical ensemble the system under consideration can exchange energy with a large heat bath such that it maintains a constant temperature. While for small systems the microcanonical and the canonical ensemble describe very different situations, the differences are negligibly small for large systems with many particles where it is not important whether the energy or the temperature is fixed [40].

In the canonical ensemble the probability of a state with phase space coordinates $\mathbf{R} = (\mathbf{r}_1, \ldots, \mathbf{r}_N)$ and $\mathbf{P} = (\mathbf{p}_1, \ldots, \mathbf{p}_N)$ is determined by

$$\rho_{\mathrm{ce}}(\mathbf{P}, \mathbf{R}) = \frac{e^{-\beta H(\mathbf{P},\mathbf{R})}}{Z(N,T)}, \tag{4.1}$$

where $\beta = 1/k_B T$. In the classical limit the canonical partition function $Z(N,T)$ reads [40]

$$Z(N,T) = \frac{1}{(2\pi\hbar)^{3N}} \int_\Omega d\mathbf{P}\, d\mathbf{R}\, e^{-\beta H(\mathbf{P},\mathbf{R})}. \tag{4.2}$$

The integral has to be evaluated over the entire phase space Ω. For identical particles one has to add the factor $1/N!$. In addition to N and T the canonical partition function can also depend on external parameters such as the volume V or the confining strength of an external trap.

Thermodynamic averages are calculated according to [40]

$$\langle A \rangle = \frac{1}{(2\pi\hbar)^{3N}} \int_{\Omega} d\mathbf{P}\, d\mathbf{R}\, \rho_{ce}(\mathbf{P},\mathbf{R})\, A(\mathbf{P},\mathbf{R}), \tag{4.3}$$

which shows that $\frac{\rho_{\mathrm{ce}}(\mathbf{P},\mathbf{R})}{(2\pi\hbar)^{3N}}$ can be regarded as the probability density in phase space.

The ergodic hypothesis states that an ensemble average is equivalent to a time average 'for a single system in equilibrium during the course of its natural evolution' [41]. While Monte Carlo simulations calculate ensemble averages, molecular dynamics simulations track the time evolution of a single system and calculate time averages of the form

$$\langle A \rangle = \lim_{\Delta t \to \infty} \frac{1}{\Delta t} \int_{t_0}^{t_0+\Delta t} dt\, A(t). \tag{4.4}$$

In the following the two simulation methods will be considered in more detail.

4.2. Molecular dynamics

4.2.1. Introduction and applications

In molecular dynamics (MD) simulations the trajectories of particles (e.g. atoms, molecules, planets etc.) are computed under the action of internal and external forces by solving the fundamental equations of motion of Classical Mechanics. This means one computes the trajectory of a system in the $3N$-dimensional phase space. Since for the general N-body problem analytical solutions do not exist, one has to rely on the numerical solution of Hamilton's equations.

MD is based on the idea that with a given set of initial conditions the system's evolution is completely determined by Hamilton's equations and any information can be extracted from the particles' trajectories. The method provides particle positions and momenta at all times and therefore a detailed microscopic description of the system. Given this information one can compute arbitrary macroscopic quantities such as pressure or temperature. The temperature is related to the kinetic energy of the system by the equipartition theorem

$$\frac{d}{2} N k_B T = E_{\mathrm{kin}} = \sum_{i=1}^{N} \frac{\mathbf{p}_i^2}{2m}, \tag{4.5}$$

where d denotes the dimensionality. Strictly speaking this is only valid in the thermodynamic limit $N \to \infty$. For finite systems the temperature has fluctuations of the order $\mathcal{O}(1/\sqrt{N})$ in the microcanonical ensemble [42].

The simplest form of MD assumes structureless particles, but it is possible to take into account internal degrees of freedom of molecules or geometric constraints as well. MD can be used to study fluids with different kinds of interaction, e.g. Yukawa [43, 44]

or Lennard-Jones [45], proteins [46] or hydrogen plasmas [47] and a wide variety of phenomena such as anomalous diffusion [44] or melting transitions [48].

Hamilton's equations of motion are purely classical. If one is interested in quantum effects, they can be incorporated by means of effective quantum pair potentials, as was done in Ref. [49]. Of course this is only possible to a limited extent and cannot include the same information as a full quantum mechanical treatment. This is why MD is usually used for problems where quantum effects are negligible or can approximately be accounted for.

Naturally MD simulations are performed at constant energy and constant N, i.e. they correspond to the microcanonical ensemble. However, there exist several techniques which extend MD simulations to constant pressure or temperature, but in these cases the equations of motion to be solved differ from the original form of Hamilton's equations. This issue will be dealt with in Section 4.3.

4.2.2. MD integrators

It is known that trajectories can be exponentially sensitive to small perturbations of the initial conditions. Thus the goal of MD simulations cannot be to yield exact trajectories since a finite timestep always introduces numerical errors and therefore small perturbations of the trajectories. A more sensitive quantity that measures the accuracy of the simulation is the total energy. For an explicitly time independent Lagrangian L with $\partial L/\partial t = 0$ Noether's theorem states that the total energy is a conserved quantity [50]. It should therefore also be conserved in the simulation. The criteria for choosing an integration scheme should be the degree of energy conservation and the ability to reproduce certain time- and space-dependent correlations [41]. Since energy conservation is connected with time-reversibility, integrators are classified according to this feature.

Leapfrog

Various schemes exist for the integration of the equations of motion. Among them are the leapfrog scheme and the Verlet algorithm which are both based on a Taylor expansion of the particle coordinates. The aim is to integrate Newton's equation of motion

$$m\ddot{\mathbf{r}}(t) = \mathbf{F}(\mathbf{r}(t), t), \tag{4.6}$$

where $\mathbf{F}(\mathbf{r}(t), t)$ denotes the force. For the coordinates $\mathbf{r}(t)$ and velocities $\mathbf{v}(t) = \dot{\mathbf{r}}(t)$ one may write [41]

$$\begin{aligned} \mathbf{r}(t+\Delta t) &= \mathbf{r}(t) + \mathbf{v}(t)\Delta t + \frac{\mathbf{F}(t)}{2m}\Delta t^2 + \mathcal{O}(\Delta t^3) \\ &= \mathbf{r}(t) + \left[\mathbf{v}(t) + \frac{\Delta t}{2m}\mathbf{F}(t)\right]\Delta t + \mathcal{O}(\Delta t^3). \end{aligned} \tag{4.7}$$

The term in brackets in the second line of Eq. (4.7) is just the first term in the Taylor expansion for $\mathbf{v}(t + \Delta t/2)$. Subtracting from $\mathbf{v}(t + \Delta t/2)$ the corresponding expression for $\mathbf{v}(t - \Delta t/2)$ one arrives at the leapfrog integration formulas

$$\begin{aligned} \mathbf{v}(t + \Delta t/2) &= \mathbf{v}(t - \Delta t/2) + \frac{\mathbf{F}(t)}{m}\Delta t \\ \mathbf{r}(t + \Delta t) &= \mathbf{r}(t) + \mathbf{v}(t + \Delta t/2)\Delta t. \end{aligned} \tag{4.8}$$

Here it is inconvenient to have coordinates and velocities at different times even though this does not pose a real problem since one can easily calculate $\mathbf{v}(t)$ from $\mathbf{v}(t - \Delta t/2)$ and the acceleration at time t. A more elegant way which avoids this issue is a two step method of the following form, which is algebraically equivalent to the original leapfrog method.

$$\begin{aligned} \mathbf{v}(t + \Delta t/2) &= \mathbf{v}(t) + \frac{\mathbf{F}(t)}{2m}\Delta t \\ \mathbf{r}(t + \Delta t) &= \mathbf{r}(t) + \mathbf{v}(t + \Delta t/2)\Delta t \\ \mathbf{v}(t + \Delta t) &= \mathbf{v}(t + \Delta t/2) + \frac{\mathbf{F}(t + \Delta t)}{2m}\Delta t. \end{aligned} \tag{4.9}$$

In this scheme the value of $\mathbf{v}(t + \Delta t)$ is calculated using the new force at time $t + \Delta t$ after the first velocity halfstep. This scheme will appear again in a similar fashion in the chapter on Langevin dynamics simulations.

The Verlet algorithm can be derived in a similar manner. Both, the leapfrog and Verlet algorithm, are time-reversible.

Runge-Kutta

Another often used technique which can generally be used to integrate ordinary differential equations (ODEs) is the Runge-Kutta method. For ODEs it is always possible to reduce an equation of higher order to a set of first order equations. Newton's equation of motion (4.6) can be written as

$$\begin{aligned} \dot{\mathbf{r}}(t) &= \mathbf{v}(t) \\ \dot{\mathbf{v}}(t) &= \frac{\mathbf{F}(\mathbf{r}(t), \mathbf{v}(t), t)}{m}. \end{aligned} \tag{4.10}$$

The three *second order* equations (4.6) have been reduced to six coupled equations (4.10) of *first order*. The force can be a function of the velocity $\mathbf{v}(t)$ or, in the N-particle case, also a function of the coordinates of all other particles. Two examples for velocity dependent forces are the Lorentz force on charged particles in the presence of magnetic fields or friction forces.

Let us now discuss the general numerical scheme of solving equations of the form

$$\frac{dy_i(t)}{dt} = f_i(t, y_1, \ldots, y_L), \qquad i = 1 \ldots L, \tag{4.11}$$

for the functions $y_1, \ldots, y_L$. The functions f_i on the right hand side of Eq. (4.11) are assumed to be known. This is the most general form of a system of L coupled first order differential equations such as (4.10).

Let $\mathbf{y}_n$ and $\mathbf{f}_n$ denote the vectors of the y_i and f_i at $t = t_n$. Runge-Kutta methods advance the solution from the point $\mathbf{y}_n = \mathbf{y}(t_n)$ to the point $\mathbf{y}_{n+1} = \mathbf{y}(t_{n+1})$ by using the derivatives of $\mathbf{y}$ at one or more points in the interval $[t_n, t_{n+1}]$. The simplest method for the integration of (4.11) reads

$$\mathbf{y}_{n+1} = \mathbf{y}_n + \mathbf{f}(t_n, \mathbf{y}_n)\Delta t, \tag{4.12}$$

where Δt is the step size. It is commonly known as the Euler method. The method is unsymmetrical since it uses only the derivative of $\mathbf{y}$ at the left point of the interval. The integration error is of the order $\mathcal{O}(\Delta t^2)$, i.e. the scheme calculates $\mathbf{y}_{n+1}$ up to first order in Δt.

The so-called mid-point method initially makes a step halfway across the interval to use the values of t and $\mathbf{y}$ at that point to calculate $\mathbf{y}$ at the right point of the interval. This method is of second order.

The following scheme is the Runge-Kutta method of fourth order and is one of the most often used integrators. The formula reads

$$\begin{aligned}
\mathbf{k}_1 &= \mathbf{f}(t_n, \mathbf{y}_n)\Delta t \\
\mathbf{k}_2 &= \mathbf{f}(t_n + \frac{\Delta t}{2}, \mathbf{y}_n + \frac{\mathbf{k}_1}{2})\Delta t \\
\mathbf{k}_3 &= \mathbf{f}(t_n + \frac{\Delta t}{2}, \mathbf{y}_n + \frac{\mathbf{k}_2}{2})\Delta t \\
\mathbf{k}_4 &= \mathbf{f}(t_n + \Delta t, \mathbf{y}_n + \mathbf{k}_3)\Delta t \\
\mathbf{y}_{n+1} &= \mathbf{y}_n + \frac{\mathbf{k}_1}{6} + \frac{\mathbf{k}_2}{3} + \frac{\mathbf{k}_3}{3} + \frac{\mathbf{k}_4}{6} + \mathcal{O}(\Delta t^5).
\end{aligned} \tag{4.13}$$

It requires four evaluations of the functions $\mathbf{f}$ per timestep. Runge-Kutta methods of order $M > 4$ always require more than M function evaluations which explains the popularity of the fourth order scheme.

As was mentioned before, higher order schemes are not always superior to low order schemes. Typically they perform better if the timestep can be chosen such that the advantage of the larger timestep is not foiled by the necessity of several force evaluations. For further gain of performance for a given limit of accuracy variable timestep methods have been developed [51]. For regions where the forces are rapidly varying a small timestep must be chosen. On the other hand, in regions where the forces are well behaved and vary considerably only on larger distances, one can get away with a larger

timestep. This can significantly enhance the performance of numerical integrators. One such method is described in Ref. [51].

The 'embedded Runge-Kutta method' calculates six coefficients which can be combined to yield a formula of fourth or fifth order. The integration error is then estimated as the difference between the two. Since it does not require explicit function evaluations for each order separately, it is superior to schemes that estimate the error based on step doubling. The MD code used in this work uses the Cash-Karp parameters as given in Ref. [51]. The code was written by Patrick Ludwig and was modified for the needs of this work. Additional information can be found in Ref. [52].

4.3. Langevin dynamics

4.3.1. Introduction

Langevin dynamics is a method similar to molecular dynamics but takes into account additional forces caused by a surrounding medium [53]. This could be air, a solvent or neutral gas particles in a dusty plasma. The motion of these particles is usually very fast due to their small mass and often of little interest. A complete simulation with these particles included explicitly in the equation of motion would require a very small timestep and thus would greatly increase the computational effort. In addition the particles will be present in much larger numbers than those of interest. In these cases one can adopt an approximate method, which models the effect of the surrounding medium as a combination of random and frictional forces.

The theoretical basis for the simplified equations of motion was given by Zwanzig [54–56] and Mori [57, 58]. They used a projection operator method to obtain a reduced description of the problem. Their approaches are equivalent and the relation between the two similar to that between the Heisenberg and the Schrödinger picture in Quantum Mechanics [53]. While Mori used projection operator methods for the time evolution of the dynamical variables $\mathcal{A}_i$ (e.g. the phase-space coordinates of the particles of interest), Zwanzig introduced the operators for the evolution of the phase space distribution function [53].

4.3.2. Langevin equation of motion

The Langevin equation of motion is

$$m\ddot{\mathbf{r}}_i = -\nabla_i U(\mathbf{r}_1, \ldots, \mathbf{r}_N) - m\nu\dot{\mathbf{r}}_i + \mathbf{f}_i(t), \tag{4.14}$$

where $i, j \in \{1, \ldots, N\}$ denote the particle index.

Compared to Newton's equation of motion it has an additional damping term with friction coefficient ν and a stochastic force $\mathbf{f}_i$ having a Gaussian distribution with zero

mean and correlation

$$\left\langle \mathbf{f}_i^{\alpha}(t)\mathbf{f}_j^{\beta}(t')\right\rangle = 2m\nu k_B T\delta_{ij}\delta_{\alpha\beta}\delta(t-t'). \tag{4.15}$$

This noise term is uncorrelated in time and there exists no correlation between different particles i, j and particle coordinates α, β. The friction and noise term balance each other to yield a particle temperature T. The coupling to the heat bath is determined by the value of the friction parameter ν.

To integrate Eq. (4.14) the quasi-symplectic SLO (symplectic low order) algorithm of Ref. [59] is used. The goal in deriving this integration scheme was to obtain an algorithm that becomes symplectic in the deterministic, frictionless case $\nu = 0$, $T = 0$ and to reproduce the equilibrium distribution function as closely as possible. So far these two conditions had not been enforced in the derivation of integration schemes at the same time.

The algorithm reads

$$\begin{aligned}
\tilde{\mathbf{r}}_i &= \mathbf{r}_i(t) + \frac{\mathbf{v}_i(t)}{2}\Delta t, \\
\mathbf{v}_i(t+\Delta t) &= c_2\left[c_1\mathbf{v}_i(t) - \frac{\nabla_i\, U(\mathbf{r}_1,\ldots,\mathbf{r}_N)|_{\mathbf{r}=\tilde{\mathbf{r}}}}{m}\Delta t + d\mathbf{w}_i\right], \\
\mathbf{r}_i(t+\Delta t) &= \tilde{\mathbf{r}}_i + \frac{\mathbf{v}_i(t+\Delta t)}{2}\Delta t,
\end{aligned} \tag{4.16}$$

and the coefficients are given by

$$c_1 = 1 - \frac{\nu\Delta t}{2}, \qquad c_2 = \frac{1}{1+\frac{\nu\Delta t}{2}}, \qquad d = \sqrt{2m\nu k_B T}. \tag{4.17}$$

$\mathbf{w}_i$ is a random Gaussian deviate with standard deviation one and zero mean. It is generated here by a GSL (GNU Scientific Library) routine using the Box-Müller algorithm.

In the limit $T \to 0, \nu \to 0$ this algorithm becomes symplectic and is similar to the leapfrog algorithm (4.9). The author of Ref. [59] showed that the algorithm can run very fast since it allows for a rather large timestep and only needs one random deviate and one force evaluation per integration step. Compared with other popular integration schemes the SLO algorithm often performs better in both speed and accuracy. In addition it is very easy to program.

4.3.3. Fokker Planck equation

The distribution function $f(x, v, t)$ for the particles that obey the Langevin equation (4.14) can be described by a Fokker Planck equation. The simplest form for non-interacting particles in 1D without external potential is given by [60]

$$\frac{\partial f}{\partial t} + v\frac{\partial f}{\partial x} = \nu\left[\frac{\partial (vf)}{\partial v} + \frac{kT}{m}\frac{\partial^2 f}{\partial v^2}\right]. \tag{4.18}$$

The first term on the right hand side is called the drift term whereas the second term describes diffusion in velocity space. A simpler form of Eq. (4.18) can be derived by neglecting inertial effects in the high damping regime. Then it is possible to obtain an equation for the evolution of the distribution function in configuration space only. Here it is assumed that after a very short time $\sim \nu^{-1}$ a Maxwellian velocity distribution is established. This simplified equation is known as the Smoluchowski equation [60].

Eq. (4.18) has the canonical distribution as stationary solution which is the reason why the Langevin approach can be used for MD simulations at constant temperature (instead of constant energy). Other thermostats with different approaches such as the extended system method or the constraint method are discussed in Ref. [53].

4.4. Monte Carlo

4.4.1. Introduction and applications

Classical Monte Carlo methods follow a different approach to obtain thermodynamic quantities. Instead of calculating time averages they directly evaluate the integral (4.3). The classical Metropolis algorithm [61] can be used to efficiently sample the configurational space of a given system and calculate thermodynamic averages. In their traditional form Monte Carlo methods are restricted to equilibrium situations. Applications include spin lattices [62], Lennard-Jones fluids [63] and especially melting [64].

Besides time-independent equilibrium calculations Monte Carlo methods can also be used for time-dependent phenomena [65], such as surface growth, surface diffusion or defect diffusion in solids. These problems usually involve a multi-timescale problem. The harmonic vibrations of atoms around their lattice positions occur on a time-scale which is much shorter than that on which transitions of atoms between lattice points occur (infrequent events). MD simulations would waste computational time simulating the fast harmonic motion of atoms that require a small timestep. *Kinetic Monte Carlo* (KMC) solves this issue by using transition probabilities between different states of the system and does not require the resolution of the fast atomic motions [65].

Monte Carlo methods have been extended to treat problems where quantum effects play a dominant role. Besides Variational Monte Carlo (VMC), which uses the minimum energy principle of the ground state wavefunction, there exists the *Path Integral Monte Carlo* (PIMC) method, based on Feynman's path integral formalism [66]. It treats quantum mechanical problems from first principles. Applications include electrons in quantum dots [11], electron-hole plasmas [67], superfluidity [68] or the Kosterlitz-Thouless transition of a trapped Bose gas [69].

In this thesis the classical Monte Carlo method will be used to find the global minimum of a function by the method of *simulated annealing*.

4.4.2. Monte Carlo integration

Solving a high-dimensional integral can be a challenging task. Traditional discretization methods will fail because they would require a large number K of function evaluations [42]. Monte Carlo methods choose a different way. Instead of evaluating the function at predefined points they are chosen randomly from a probability distribution [42, 66]. This can greatly improve the performance of numerical integration for high dimensions if the probability distribution is chosen appropriately. A one-dimensional integral of a function $f(x)$ can be evaluated according to

$$\int_a^b f(x)dx = \int_a^b \frac{f(x)}{p(x)}p(x)dx \approx \frac{1}{K}\sum_{i=1}^{K}\frac{f(\tilde{x}_i)}{p(\tilde{x}_i)}. \tag{4.19}$$

The integral is regarded as the mean of the new function $f(x)/p(x)$ and the $\{\tilde{x}_i\}$ are chosen from the probability density $p(x)$. The idea is to choose $p(x)$ such that the function is sampled at points where the main contribution to the integral comes from. This is called *importance sampling*. A uniform probability density corresponds to *straightforward sampling*.

In Statistical Physics one has to evaluate integrals of the form

$$I = \int_{-\infty}^{\infty} f(x)p(x)dx, \qquad I^{\mathrm{MC}} \approx \frac{1}{K}\sum_{i=1}^{K} f(\tilde{x}_i). \tag{4.20}$$

Here the error of the MC integration is proportional to $\sigma/\sqrt{K}$, where K is the number of function evaluations and $\sigma^2 = \int_{-\infty}^{\infty} f^2(x)p(x)dx - I^2$ is the variance of the integral of the function $f(x)$. Reducing the error can be achieved by either choosing $p(x)$ to reduce σ or/and increasing K.

One can show that for traditional integration methods, such as Simpson's rule, the error for a d-dimensional integration decreases as $K^{-a/d}$ if the error for a 1D integration decreases as K^{-a}. For MC methods the error *always* decreases as $K^{-1/2}$. Thus MC integration has its advantages for high dimensions (typically $d \gtrsim 5$) whereas for low dimensions ordinary methods are often advantageous [66].

4.4.3. Markov-chain and Metropolis algorithm

For Hamiltonians of the form $H = \sum_{i=1}^{N} \frac{\mathbf{p}_i^2}{2m} + U(\mathbf{R})$ and if the quantity A does not depend on $\mathbf{P}$, the momentum integration in the integral (4.3) can be performed analytically and can be canceled (the integral also appears in ρ_{ce}). Only the coordinate

part including the potential energy $U(\mathbf{R})$ has to be solved. The probability density is a function of the coordinates only.

The remaining integral can then be evaluated using the idea of importance sampling [66] according to

$$\langle A \rangle = \int_{-\infty}^{\infty} d\mathbf{R}\, A(\mathbf{R}) p(\mathbf{R}) \approx \frac{1}{K} \sum_{i=1}^{K} A(\mathbf{R}_i). \tag{4.21}$$

Here the $\mathbf{R}_i$ must be chosen from the probability density

$$p(\mathbf{R}) = \frac{e^{-\beta U(\mathbf{R})}}{\int_{-\infty}^{\infty} d\mathbf{R}\, e^{-\beta U(\mathbf{R})}}. \tag{4.22}$$

Unfortunately $p(\mathbf{R})$ is not known a priori since it requires the evaluation of the integral in Eq. (4.22).

This is where Metropolis proposed the idea of using a Markov chain in 1953 [61]. In the Markov chain only transition probabilities from a state with coordinates $\mathbf{R}_i$ to a new state with coordinates $\mathbf{R}_{i+1}$ are specified [66]. If the transition probability $v(\mathbf{R}_i, \mathbf{R}_{i+1})$ obeys the following restrictions $(1) - (4)$, it can be shown that the $\mathbf{R}_i$ are distributed according to the given probability density $p(\mathbf{R})$. This is not restricted to the one given by Eq. (4.22).

(1) Conservation law: $\sum_{\mathbf{R}_{i+1}} v(\mathbf{R}_i, \mathbf{R}_{i+1}) = 1$ for all $\mathbf{R}_i$

(2) Convergence to a unique equilibrium state: $\sum_{\mathbf{R}_i} p(\mathbf{R}_i) v(\mathbf{R}_i, \mathbf{R}_{i+1}) = p(\mathbf{R}_{i+1})$

(3) Ergodicity: One can go from any state to any other state in a finite number of steps.

(4) Non-negative transition probabilities: $v(\mathbf{R}_i, \mathbf{R}_{i+1}) \geq 0$ for all $\mathbf{R}_i$

The time evolution of the probability density is given by the *Master equation*

$$\frac{dp(\mathbf{R}_i)}{dt} = \sum_{\mathbf{R}_{i+1}} v(\mathbf{R}_{i+1}, \mathbf{R}_i) p(\mathbf{R}_{i+1}) - \sum_{\mathbf{R}_{i+1}} v(\mathbf{R}_i, \mathbf{R}_{i+1}) p(\mathbf{R}_i), \tag{4.23}$$

which describes the in- and outgoing probability flow into the state $\mathbf{R}_i$. The stationary solution of the Master equation with $\frac{dp(\mathbf{R}_i)}{dt} = 0$ corresponds to thermodynamic equilibrium.

If the condition of *detailed balance* is imposed,

$$p(\mathbf{R}_i) v(\mathbf{R}_i, \mathbf{R}_{i+1}) = p(\mathbf{R}_{i+1}) v(\mathbf{R}_{i+1}, \mathbf{R}_i), \tag{4.24}$$

and ergodicity is assumed to be guaranteed, the sampling with the transition probability $v(\mathbf{R}_i, \mathbf{R}_{i+1})$ will yield the correct distribution $p(\mathbf{R})$.

For the special case of the canonical ensemble with $p(\mathbf{R})$ given by Eq. (4.22) one can

make the particular choice of

$$v(\mathbf{R}_i, \mathbf{R}_{i+1}) = \begin{cases} e^{-\beta \Delta U}, & \text{if } \Delta U = U(\mathbf{R}_{i+1}) - U(\mathbf{R}_i) \geq 0 \\ 1, & \text{otherwise} \end{cases} \tag{4.25}$$

This choice for the transition probabilities has a very intuitive physical meaning. On the one hand MC moves that decrease the potential energy are always accepted. On the other hand moves that increase U are only accepted with a probability given by the Boltzmann factor and thus depend on the specified temperature of the system. If these moves were always rejected this could lead to trapping of the system in a metastable state and would violate the detailed balance condition (4.24).

4.4.4. Simulated annealing

The simulated annealing procedure [51, 70] can be used to find the global (energy) minimum of a function $U(N_1, \ldots, N_L)$ of L variables. While local optimization methods can easily be trapped in a local minimum [51], the simulated annealing method does not suffer from this problem in general. It is often used when a global minimum is hidden among many other local minima.

The procedure is similar to crystallization processes that occur in nature [51]. A liquid metal may be trapped in an amorphous state with a higher energy rather than the ground state when cooled very quickly. While for high temperatures the atoms can move freely and do not 'feel' the potential energy surface, they lose their mobility for low temperatures. The probability distribution is given by the Boltzmann distribution $p \sim e^{-U/k_B T}$. Even for low temperatures there is a chance that the system is in a state with high energy. Most methods can only go 'downhill' until they reach a local minimum. In the simulated annealing approach the system is also allowed to go 'uphill' and thus can escape from a local minimum. This is only possible if the probability of 'uphill' moves is sufficiently high. Thus the temperature, directly related to the probability of these moves, must be decreased very slowly. The procedure works as follows.

Starting with an initial set of parameters the Metropolis algorithm is used to create a set of new parameters while the temperature of the system is slowly being decreased. Since MC moves can be accepted even for steps that do not decrease the energy, trapping in a local minimum can often be avoided. As the temperature decreases, the probability of accepting states with higher energy decreases. For $T = 0$ only moves with $\Delta U < 0$ will be accepted. If the initial temperature is chosen sufficiently high and is decreased very slowly, the probability of finding the global minimum is high. Since for a finite simulation length the probability is always less than one, the procedure has to be repeated several times to ensure the correctness of the obtained (global) minimum.

5. Shell model of Yukawa balls

5.1. Introduction

The problem of finding the ground state for a system consisting of a large number of particles can be a demanding task since one has to find the global minimum of the potential energy U, which is a function of $3N$ variables. For Coulomb or Yukawa balls one can directly make use of the observed shell structures in the experiments and the simulations to obtain a simplified description. Instead of keeping track of all particle positions one is only interested in the occupation numbers of the shells and their radii. This dramatically reduces the complexity of the problem. This description is known as the shell model. It was first introduced by Hasse and Avilov in 1991 for particles with Coulomb interaction [71]. Here a recently developed shell model for particles with Yukawa interaction [2] is investigated and compared to MD simulations [1].

5.2. Derivation

Shell models are based on the assumption that the particles are located on concentric, spherical shells of zero thickness and that the charge is uniformly distributed on the shells [73], see Fig. 5.1. While this is a rather crude assumption for only two particles,

[1] The results of this chapter are published in Ref. [72]. MD results were provided by Volodymyr Golubnychiy.

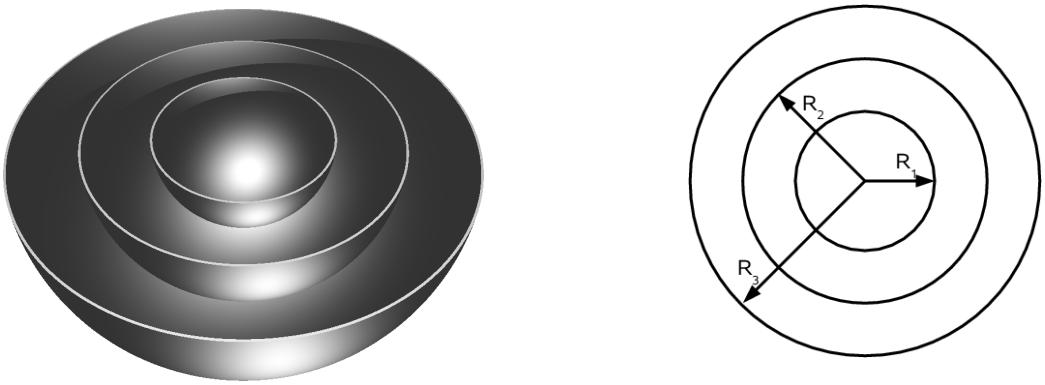

Figure 5.1.: *Illustration of the charge distribution in the shell model. A cluster with three shells and a discrete charge distribution is mapped onto a system with a uniform charge distribution.*

the charge distribution should become more homogeneous when the particle number is increased.

In the case of a continuum model [2], where physical quantities are a function of the density, the energy at $T = 0$ can be written as

$$E[n] = \int d^3r\, u(\mathbf{r}). \tag{5.1}$$

In the mean field approximation, where correlations are neglected, the potential energy density is given by

$$u(\mathbf{r}) = n(\mathbf{r})\left\{ V_{\text{ext}}(\mathbf{r}) + \frac{N-1}{2N} \int d^3\mathbf{r}'\, n(\mathbf{r}') V(|\mathbf{r} - \mathbf{r}'|) \right\}, \tag{5.2}$$

where $V_{\text{ext}}(\mathbf{r})$ denotes the contribution of an external confinement and $V(r)$ the interaction between the particles.

By making the ansatz that the density is composed of L concentric, spherical shells with shell occupation numbers N_ν and radii R_ν,

$$n_s(\mathbf{r}) = n_s(r) = \sum_{\nu=1}^{L} \frac{N_\nu}{4\pi R_\nu^2}\, \delta(r - R_\nu), \tag{5.3}$$

a shell model can be derived from Eq. (5.2). The energy in this model for Yukawa interaction is [2]

$$\begin{aligned} E_s(\{N_\nu\}, \{R_\nu\}, \kappa) = \sum_{\nu=1}^{L} N_\nu \Bigg\{ V_{\text{ext}}(R_\nu) + Q^2 \frac{e^{-\kappa R_\nu}}{R_\nu} \times \\ \left(\frac{\sinh(\kappa R_\nu)}{\kappa R_\nu} \frac{N_\nu - 1}{2} + \zeta + \sum_{\mu<\nu} \frac{\sinh(\kappa R_\mu)}{\kappa R_\mu} N_\mu \right) \Bigg\}. \end{aligned} \tag{5.4}$$

$\zeta \in \{0, 1\}$ denotes the possibility of a particle being located in the center of the cluster.

However, the expression obtained from the mean field model neglects correlation effects. In Ref. [73] correlations were taken into account for the Coulomb model by modifying the term for the intrashell energy $s(N_\nu)$ according to $s(N_\nu) = N_\nu - 1 \to N_\nu - \epsilon_\nu(N, \kappa)\sqrt{N_\nu}$. Here $\epsilon_\nu(N, \kappa)$ is a fit parameter that allows for an excellent agreement with MD simulations.

Following the same procedure for Yukawa interaction one obtains the energy

$$\begin{aligned} E_s(\{N_\nu\}, \{R_\nu\}, \kappa) = \sum_{\nu=1}^{L} N_\nu \Bigg\{ V_{\text{ext}}(R_\nu) + Q^2 \frac{e^{-\kappa R_\nu}}{R_\nu} \times \\ \left(\frac{\sinh(\kappa R_\nu)}{\kappa R_\nu} \frac{N_\nu - \epsilon_\nu(N, \kappa)\sqrt{N_\nu}}{2} + \zeta + \sum_{\mu<\nu} \frac{\sinh(\kappa R_\mu)}{\kappa R_\mu} N_\mu \right) \Bigg\}. \end{aligned} \tag{5.5}$$

In the limit $\kappa \to 0$ (Coulomb interaction) one recovers [73]

$$E_s(\{N_\nu\},\{R_\nu\}) = \sum_{\nu=1}^{L} N_\nu \left\{ V_{\text{ext}}(R_\nu) + \frac{Q^2}{R_\nu}\left(\frac{N_\nu - \epsilon_\nu(N)\sqrt{N_\nu}}{2} + \zeta + \sum_{\mu<\nu} N_\mu \right) \right\}, \quad (5.6)$$

which is similar to the shell model of Tsuruta and Ichimaru [74], where $\epsilon_\nu \equiv 1$, and the model of Hasse and Avilov [71], where the square root term is missing. Here the case of a parabolic confinement potential $V_{\text{ext}}(r) = \frac{m}{2}\omega_0^2 r^2$ is considered.

The first term in Eq. (5.6) denotes the contribution of the external confinement while the remaining two terms take into account the interaction between particles on the same shell and on different shells, respectively.

The different terms for Coulomb interaction can readily be understood in terms of simple formulas for spherical capacitors [73]. The energy of the intrashell term can be obtained by counting the number of pair interactions of particles on the same shell. A homogeneously charged sphere composed of $N_\nu - 1$ particles has a potential $(N_\nu - 1)Q/R_\nu$ at its surface giving an energy contribution of $N_\nu(N_\nu - 1)Q^2/(2R_\nu)$ for each shell. The factor $1/2$ simply avoids double counting. The square root in the intrashell term in Eq. (5.6) takes into account that each particle occupies a finite area $A_\nu = 4\pi R_\nu^2/N_\nu$ on the surface of the sphere which cannot be occupied by other particles [73, 74]. A justification for the parameter ϵ, which has been proposed by the authors of Ref. [73], has recently been given in Ref. [75], where the Coulomb shell model was developed by resorting to the Thomson problem. Here ϵ is used as a fit parameter.

The interaction energy between different shells (intershell) is determined by the charge inside a given shell. The shell ν 'feels' the potential of the charge $\sum_{\mu<\nu} N_\mu Q$ inside its radius which is just that of a point charge located at the origin. This explains the appearance of the double sum in Eq. (5.6). The center particle can also be attributed to this term.

In the case of Yukawa interaction the Coulomb potential $\sim 1/r$ is not simply replaced by the Yukawa potential $\sim \exp(-\kappa r)/r$ but contains an additional factor $\sinh(\kappa r)/(\kappa r)$.

5.3. Variation procedure and results for Coulomb interaction

The correlation parameter ϵ is used to fit the energy of the shell model to the MD energies. In the beginning it is assumed that $\epsilon_\nu \equiv \epsilon$ for all shells. The variation parameters L, N_ν, ζ, R_ν and $\epsilon_\nu(N)$ are obtained by minimizing the total energy (5.5) using the following procedure.

Shell radii

The computation of the energy (5.5) for a given set of shell occupancies requires the unknown shell radii. They can be determined from the condition

$$\frac{\partial E_s}{\partial R_\nu} = 0, \qquad \nu = 1, \ldots, L, \tag{5.7}$$

which yields a set of equations for the $\{R_\nu\}$. For Coulomb interaction the equations are uncoupled and the system (5.7) can be solved analytically. One obtains

$$\frac{R_\nu}{r_0} = 2^{-1/3} \left[\frac{N_\nu - \epsilon(N)\sqrt{N_\nu}}{2} + \zeta + \sum_{\mu<\nu} N_\mu \right]^{1/3}, \tag{5.8}$$

which shows that the radius of the shell ν is only determined by the charge inside the shell and on itself.

For Yukawa interaction this is not the case due to the R dependence of the sum over the inner shells in Eq. (5.5). Here Eq. (5.7) comprises a set of coupled nonlinear equations and must be solved numerically. This is done using the Newton-Raphson method [51]. Details on the procedure can be found in Appendix A.

Occupation numbers: Monte Carlo algorithm

The shell occupation numbers are found using a Monte Carlo method with simulated annealing. The initial configuration for the MC procedure is chosen randomly. In a Monte Carlo step the configuration is changed randomly and the Metropolis algorithm (cf. Section 4.4.3) is used to either accept or reject the new set of occupation numbers, based on their potential energy. Thereby the restriction $\sum_\nu N_\nu + \zeta = L$ must always be fulfilled.

As explained in Section 4.4.4, the temperature is slowly decreased at each step by rescaling T by a factor $f < 1$ (typically $f \approx 0.9995$). Depending on the number of particles, the number of MC steps ranges from approximately 10,000 – 30,000 for a single run.

The configuration with the lowest energy is recorded throughout the entire procedure. During a single calculation the number of shells L is not varied. However, one has to assure that a calculation with a greater number of allowed shells does not lead to a lower energy. Once an optimal set of occupation numbers has been found, the number of shells is increased by one and the optimization procedure is repeated. If this does not lead to a lower energy, the occupation numbers are accepted as the lowest energy configuration. To assure that the correct ground state has been found for a given L, the procedure is repeated several times with different initial configurations.

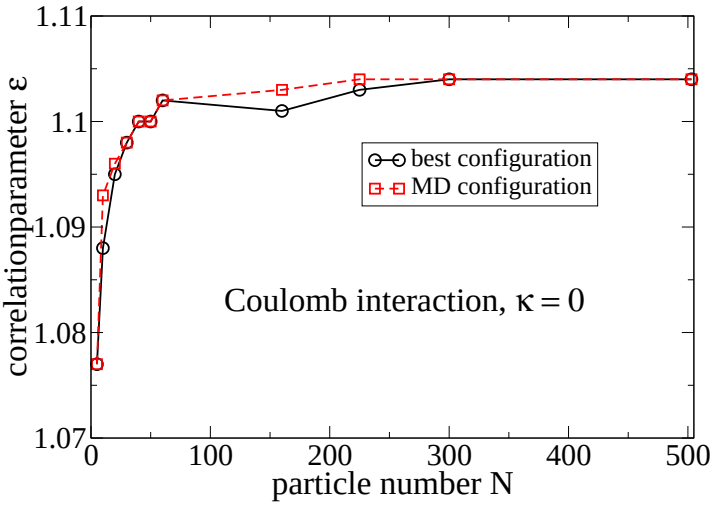

Figure 5.2.: *Correlation parameter ϵ as a function of total number of particles for Coulomb interaction, obtained from (a) MD configuration (squares), (b) ground state configuration of shell model (circles).*

Determination of the fit parameter ϵ

Three methods are used to determine the fit parameter ϵ:

1. The ground state MD configuration is fixed and used as input for the shell model. An ϵ is found such that the energy of the shell model $E_{\text{model}} = E_{\text{MD}}$. This is not possible for all MD configurations as one is limited by the constraint $\epsilon < \sqrt{N_\nu}$. Otherwise one would obtain unphysical negative energy contributions for the intrashell interaction term.

2. For a given ϵ the ground state of the shell model is determined and compared to the MD energy. Since the energy decreases with increasing ϵ, one starts with a value that gives an energy greater than the MD energy. Now ϵ is decreased to yield an energy $E_{\text{model}} = E_{\text{MD}}$. Again one can only take into account configurations with $\epsilon < \sqrt{N_\nu}$.

3. A fit is performed for the correlation parameters obtained for the ground state of method two. Beginning with the MD occupation numbers $\{N_\nu^{\text{MD}}\}$ the fit is used to calculate a single correlation parameter $\epsilon_\nu(N_\nu^{\text{MD}}, \kappa)$ for each shell. The ground state configuration is then determined for a limited number of shells given by the MD data.

For Coulomb interaction the results for methods 1 and 2 are shown in Fig. 5.2.

For large N the parameter ϵ tends to a constant value of 1.104. This is in agreement with Ref. [73].

Model	E/N	configuration
shell model	5.3914	$(10, 6, 1)$
without	5.3427	$(8, 5, 3, 1)$
correlations	5.3238	$(6, 5, 3, 2, 1)$
MD	4.5784	$(16, 1)$

Table 5.1.: *Effect of neglecting correlations in the shell model for a system of* $N = 17$ *particles and* $\kappa = 0.3$*. The number of allowed shells ranges from* 2 *to* 4*.*

5.4. Results for Yukawa interaction

The same procedure is applied to the case of Yukawa interaction. A system of $N = 12$ particles is considered first. The ground state according to the MD simulations is $(12, 0)$ for $\kappa \leq 4.1$ [33]. For larger screening parameters $(12, 0)$ becomes a metastable state. Fixing this configuration ϵ is determined to fit the energy of the MD simulations. Results are given in Fig. 5.3. Clearly ϵ strongly increases as κ is increased.

Fig. 5.4 shows the effect of neglecting the correlation term in the shell model. The energy of this model is constantly above the results of the MD simulations. In Tab. 5.1 the occupation numbers and energies computed with the shell model without the correlation term are given for a system of $N = 17$ particles. The number of shells is restricted to the value given in the table. The energy of this model is much larger than the energy of the MD simulations. Increasing the number of allowed shells results in a system with many shells and low occupation numbers, strongly deviating from the MD result.

In Fig. 5.5 the difference between the energy of the configurations $(12, 0)$ and $(11, 1)$ is shown for the shell model and the MD simulations. The configuration $(11, 1)$ is the ground state in the MD simulations only for $\kappa \geq 4.1$. In contrast, the shell model without the correlation term prefers the $(11, 1)$ state for all tested screening parameters. Including the correlation term (fitted for the $(12, 0)$ configuration and all κ) $(12, 0)$ remains the ground state up to $\kappa \approx 2.5$ being much closer to the exact behavior.

The radii for the different models are compared in Fig. 5.6. For Coulomb interaction the radii of the MD simulations and the shell model with correlations are approximately equal. For increasing screening parameters the deviations grow larger and the shell model predicts too small radii. Neglecting correlations the shell model yields too large radii for all tested screening parameters. However, the shape of the exact function is well reproduced.

Fig. 5.7 shows the obtained correlation parameters for different screening parameters and different numbers of particles. The ground state values (method 2) are used to obtain an analytical fit according to $\epsilon(N, \kappa) = a \cdot N^b$ with the fit parameters a, b. The

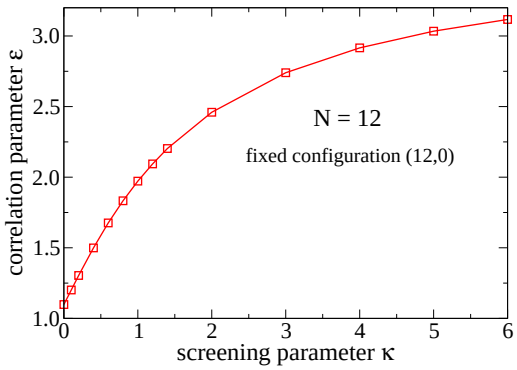

Figure 5.3.: *Correlation parameter ϵ as a function of the screening parameter κ for a fixed MD configuration (12,0).*

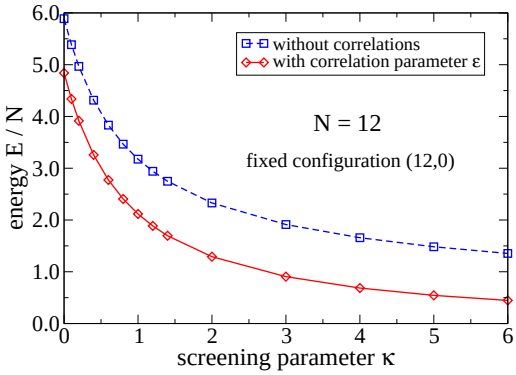

Figure 5.4.: *Effect of neglecting the correlation term in the shell model for a system of $N = 12$ particles for different screening parameters, fixed configuration $(12, 0)$. The energy of the MD simulations is equal to the graph including correlations.*

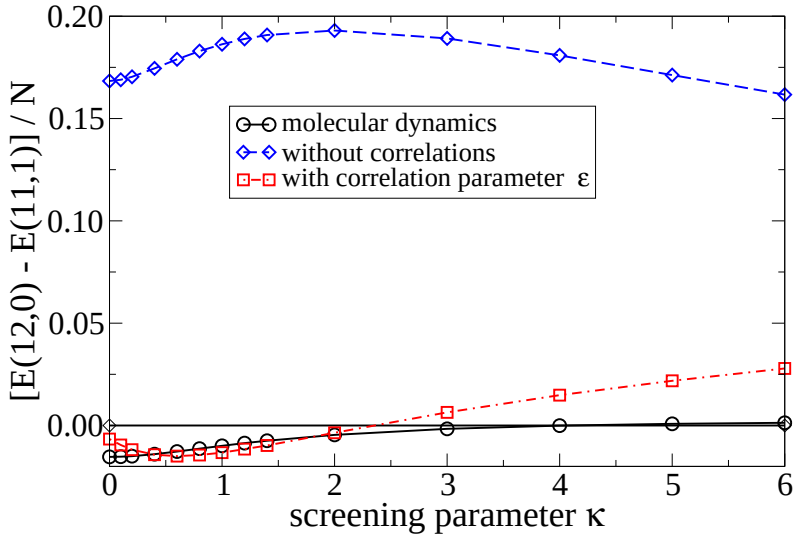

Figure 5.5.: *Preferred states for a system of $N = 12$ particles, (a) MD simulations (circles), (b) shell model neglecting the correlation term (diamonds), (c) shell model with the correlation parameter determined to fit the energy of the configuration (12,0) (squares).*

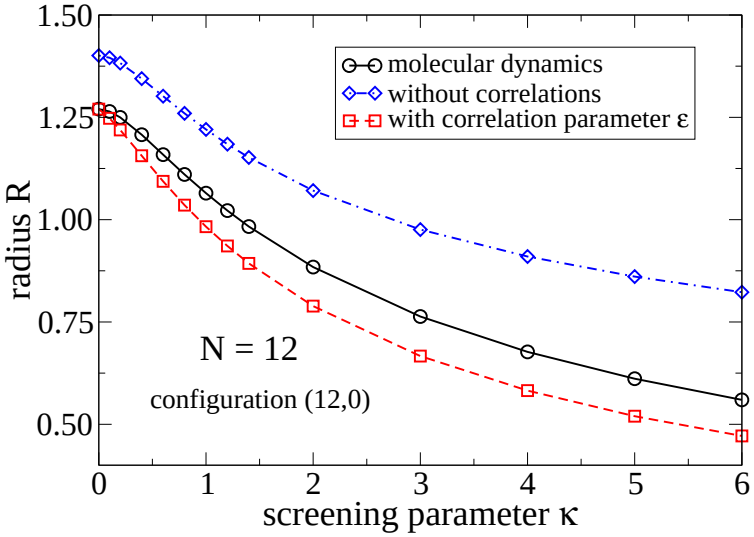

Figure 5.6.: *Radii for different screening parameters in the case of (a) MD simulations (circles), (b) shell model neglecting correlations (diamonds), (c) shell model including correlations (squares).*

fit results are, for three values of κ,

$$\begin{aligned} \epsilon(N, \kappa = 0.3) &= 0.891 \cdot N^{0.164}, \\ \epsilon(N, \kappa = 0.6) &= 0.957 \cdot N^{0.204}, \\ \epsilon(N, \kappa = 1.0) &= 1.001 \cdot N^{0.231}. \end{aligned} \tag{5.9}$$

The deviations between the values obtained from the MD configuration and the ground state of the shell model are small for $\kappa = 0.3$. For larger screening parameters ($\kappa = 0.6$ and $\kappa = 1.0$) one can clearly observe an increasing discrepancy. Instead of approaching a constant value as in the Coulomb case ϵ increases significantly with N.

In Table 5.2 some sample configurations are presented for different parameters. On the one hand, for small clusters the occupation numbers are comparable to the MD configurations. On the other hand, for larger clusters ($N = 278, 300$) substantial deviations occur. Here allowing for different ϵ_ν for different shells (method 3) produces better results. In general the radii of the outer shells are well predicted by the shell model. Using only one correlation parameter for all shells (method 2) leads to a very small radius of the first shell in the case of a low occupation number. As there are no energy contributions from other shells in this case, the term of the intrashell contribution is mostly compensated by the correlation term. Again, different ϵ_ν decrease

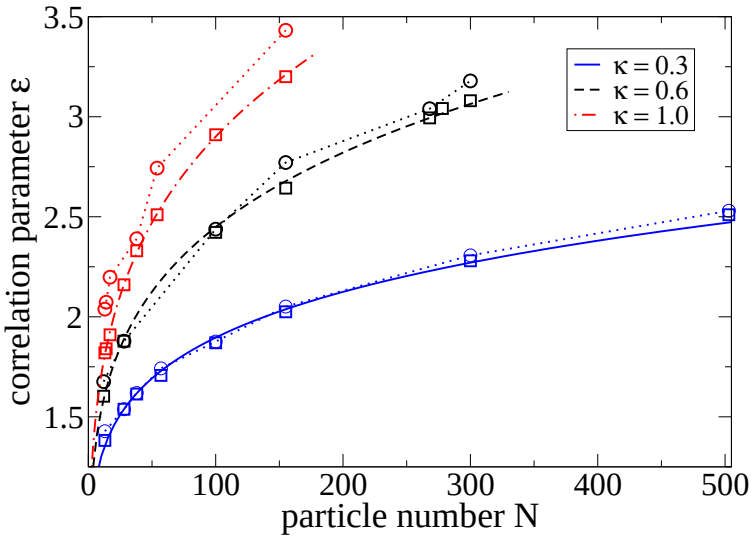

Figure 5.7.: *Correlation parameter ϵ as a function of total number of particles for Yukawa interaction, obtained from (a) MD configuration (method 1, circles), (b) ground state configuration of shell model (method 2, squares). The lines through the squares are the best fit, given by Eq. (5.9).*

κ	N	model	E/N	occupation numbers N_ν	shell radii R_ν
0.3	28	$\epsilon = 1.538$	6.4301	$(24, 4)$	1.7613 0.5872
0.3	28	MD	6.4292	$(24, 4)$	1.7915 0.7559
0.6	28	$\epsilon = 1.878$	4.8400	$(24, 4)$	1.6182 0.3543
0.6	28	MD	4.8397	$(24, 4)$	1.6575 0.6898
0.3	100	$\epsilon = 1.870$	14.0559	$(65, 31, 4)$	2.8838 1.7708 0.3678
0.3	100	MD	14.0554	$(69, 27, 4)$	2.8739 1.7696 0.7265
0.6	100	$\epsilon = 2.422$	10.0248	$(60, 34, 6)$	2.6231 1.6472 0.2121
0.6	100	MD	10.0245	$(67, 27, 6)$	2.5923 1.6326 0.7667
0.6	278	$\epsilon = 3.041$	16.9964	$(92, 81, 61, 34, 10)$	3.7530 3.1027 2.3773 1.5535 0.3445
0.6	278	diff. ϵ_ν	17.4250	$(134, 88, 45, 11)$	3.6139 2.6997 1.7756 0.8360
0.6	278	MD	16.9961	$(143, 80, 42, 12, 1)$	3.5836 2.6669 1.8400 1.0181
0.3	300	$\epsilon = 2.280$	25.9038	$(135, 97, 54, 14)$	4.2460 3.2798 2.1983 0.9573
0.3	300	diff. ϵ_ν	26.1995	$(152, 94, 44, 10)$	4.1925 3.1296 2.0471 0.9704
0.3	300	MD	25.9033	$(154, 90, 43, 12, 1)$	4.1947 3.1162 2.0611 1.1940

Table 5.2.: *Total energy from Eq. (5.5), shell occupation numbers N_ν and radii R_ν. The first line in each row corresponds to model 2, 'diff. ϵ_ν' denotes the use of different ϵ values for each shell.*

the deviations. Thus the best choice is the use of $\epsilon_\nu = \epsilon(N_\nu^{\mathrm{MD}}, \kappa)$ using the above fit formulas with the MD shell population.

5.5. Discussion

An improved shell model for Yukawa balls has been discussed. There, an additional correlation parameter $\epsilon(N, \kappa)$ is used to fit the energy of the shell model to the MD energies. The occupation numbers for this method are in the same range as the MD results but show deviations. While the results deviate by only a few particles for small N, the deviations can become rather large for higher particle numbers and larger κ. Allowing for different parameters for different shells, the model predicts the MD configurations much more accurately. Here the energies are different from the MD results whereas the radii are well reproduced. For a comparison to experiments with low screening ($\kappa \leq 0.6$) the shell model is able to predict shell populations within experimental errors. For higher screening and for usage as a diagnostic for determining the exact experimental screening, it is still recommended to use MD simulations.

The recently published article by Cioslowski et al. [75] gives an explanation for the appearance of the correlation parameter in the Coulomb shell model by resorting to the solution of the Thomson problem. Here the large N asymptote for the intrashell term is given by

$$s(N_\nu) \sim N_\nu - \xi_1 \sqrt{N_\nu} + \xi_2 N_\nu^{-1/2}, \tag{5.10}$$

which explains the success of the proposed fit parameter ϵ used in the present approach with $s(N_\nu) = N_\nu - \epsilon\sqrt{N_\nu}$. In addition the conjectured exact value of

$$\xi_1 = \frac{3^{3/4}}{\sqrt{2\pi}} \left[\zeta\left(\frac{1}{2}, \frac{2}{3}\right) - \zeta\left(\frac{1}{2}, \frac{1}{3}\right) \right] \zeta\left(\frac{1}{2}, 0\right) \approx 1.10610,$$

where $\zeta(s, a)$ denotes the generalized Riemann zeta function, is very close to the value found in Ref. [73], also cf. Fig. 5.2.

It should be possible to obtain better results for the Yukawa model by finding the correlation energy for each shell separately instead of determining it from a method that is based on a single function $\epsilon(N, \kappa)$ for all shells. The authors of Ref. [76] approximated the intrashell cohesive (correlation) energy in their shell model (with a different confinement potential) by that of a two-dimensional Yukawa lattice. Applied here this could expand the applicability of the model to comparison with the experiments.

A rigorous derivation for a Yukawa shell model including correlation effects is still missing.

6. Probability of metastable states

6.1. Introduction

Recently metastable states of Yukawa balls have been investigated in Ref. [3] for small particle numbers $N = 27$ and $N = 31$. It was found that often metastable states occurred with a higher probability than the ground state. This was confirmed by MD simulations but no theoretical explanation was given. This is the goal of this chapter [1]. Monte Carlo simulations (MC) as well as extensive molecular dynamics (MD) simulations are applied with a broader parameter range than before, confirming the main results of Ref. [3]. For a theoretical explanation an analytical method based on the classical canonical partition function [78] is employed. In addition to small clusters also a larger cluster with 190 particles is investigated and previous results, based on comparison of the ground state shell occupation numbers, are discussed.

[1] Most of the results in this chapter are published in Ref. [77]

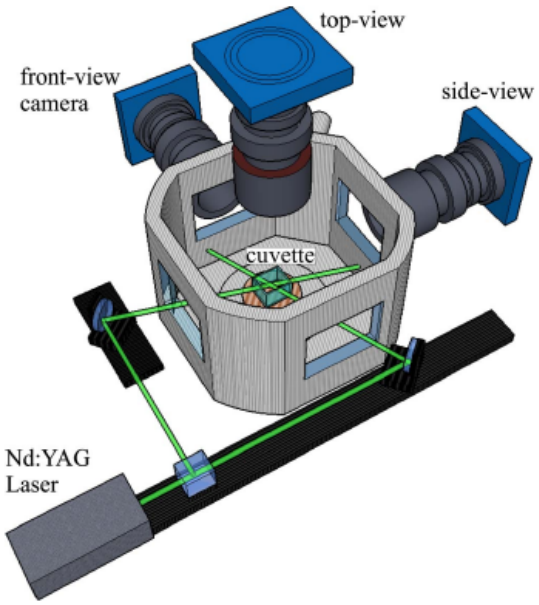

Figure 6.1.: *Camera setup used to record the motion of the dust particles. The particles are illuminated by two expanded laser beams from two directions. High-speed video cameras are used to record the dust particles inside the cuvette. From Ref. [79].*

6.2. Experiments

The experiments on metastable states [3] were conducted with the setup explained in Section 2.2.4. The clusters were illuminated with an expanded laser beam at a power of 600 mW and a wavelength of 532 nm. The dust particle motion was recorded with an improved stereoscopic setup consisting of three synchronized cameras with pairwise perpendicular orientation, see Fig. 6.1.

Small dust crystals with $N = 27$ and $N = 31$ were produced repeatedly. The particles were trapped by a nearly spherically isotropic confinement potential which was rapidly turned off and on. In this time the present cluster is destroyed and falls towards the lower electrode. Before the dust particles leave the discharge the confinement is reestablished and a new (possibly different) cluster is created, without memory of the previous configuration. This allowed to repeat the crystal formation frequently without changing the plasma parameters and to compute probabilities of stationary states (shell configurations) from the occurrence frequencies.

6.3. Model and simulation idea

6.3.1. Hamiltonian and potential energy

The system of dust particles is described by the Hamiltonian (3.1). The ground (metastable) states are the global (local) minima of the potential energy U,

$$U(\mathbf{r}_1, \ldots, \mathbf{r}_N) = \sum_{i=1}^{N} \frac{m}{2}\omega_0^2 r_i^2 + \sum_{i>j}^{N} \frac{Q^2}{|\mathbf{r}_i - \mathbf{r}_j|} e^{-\kappa|\mathbf{r}_i - \mathbf{r}_j|}. \tag{6.1}$$

In both cases the total force on all particles vanishes and the system is in a stable configuration, i.e. stable against small perturbations.

6.3.2. Monte Carlo (MC)[2]

The MC simulations use the standard Metropolis algorithm (Section 4.4) with the Hamiltonian (3.1), but without the kinetic energy part. Starting from the classical ground state at $T = 0$ the system is given a finite temperature. For a fixed temperature 10^7 MC steps are performed and the configuration is determined every 10^4th step. The temperature is then increased and the same procedure repeated. Ergodicity of the procedure was checked by using different initial configurations. Following this method the probability is calculated as a function of T from the number of occurrences of the different states.

[2]The MC simulations in this chapter were performed by Henning Baumgartner.

6.3.3. Molecular dynamics (MD)

In the MD simulations the approach is different. Here the equations of motion for particles in a parabolic trap interacting through the Yukawa potential (3.3) are solved but an additional damping term is included to simulate the annealing process the way it occurs in the experiment, as explained in Ref. [3]. This is different from the MC simulations where the particles are in contact with a heat bath and maintain a constant temperature. This also differs from the MD simulations in Ref. [3] which were also performed at finite temperature. Here, the performed simulations are substantially larger and a broader parameter range is scanned. For the ith particle the equation of motion is

$$m\ddot{\mathbf{r}}_i = -\nabla_i U(\mathbf{r}_1, ..., \mathbf{r}_N) - \nu m\dot{\mathbf{r}}_i, \tag{6.2}$$

where ν is the collision frequency, which will be given in units of ω_0. Eq. (6.2) is solved using the 'embedded Runge-Kutta method' as explained in Section 4.2.2. Due to the friction term the system described by Eq. (6.2) is non-Hamiltonian. In dusty plasmas friction is mainly due to the neutral gas.

The simulation is initialized with random particle positions and velocities in a square box. To stop the simulation and determine the configuration two similar, but not equivalent conditions are used:

(A) The particles' mean kinetic energy drops below a threshold value $\left\langle E_{\mathrm{kin}}^{\mathrm{min}} \right\rangle$ of typically $10^{-6} - 10^{-8}$.

(B) The force on each particle due to the confinement and the other particles decreases below 10^{-4}.

It is tempting to define (A) as a proper condition but it will be shown that (B) has to be used, although they look equivalent at first glance. The difference lies in the definition of a stable configuration. If the particles lose their initial kinetic energy before they have reached a local minimum, the simulation could be stopped before the particle motion has effectively ended. This problem can be circumvented by condition (B) which makes direct use of the definition of a stable state, namely that the force on each particle due to U vanishes.

The screening parameter, the friction coefficient as well as the lower limit for the mean kinetic energy are varied. For each parameter setting the simulation is repeated $3000 - 5000$ times to obtain accurate statistics. Systems with 31 and 27 particles are considered as was done in the experiment. As another example a cluster with 40 particles is used because here the ground state shell configuration abruptly changes from (34,6) to (32,8) at $\kappa = 0.415$ as the screening parameter is increased – without the configuration (33,7) ever being the ground state [33]. This gives rise to the question of how often this configuration can actually occur in experiments.

The Yukawa cluster with 190 particles has been investigated in detail in Ref. [29]. There the screening parameter was determined by comparing the experimental configuration with the ground state configuration of the simulations. It was thus assumed that the

Table 6.1.: *Energy difference between metastable states and the ground state (the ground state and its energy is given by italic numbers) as seen in Fig. 6.2. States with the same shell configuration but different energy differ only by the arrangement of the particles on the same shell (fine structure).*

$\Delta E/N$	configuration	$\Delta E/N$	configuration
3.030266	*(27,4)*	0.000479	(26,5)
0.000006	(27,4)	0.000499	(26,5)
0.000009	(27,4)	0.000530	(26,5)
0.000291	(26,5)	0.000656	(25,6)
0.000372	(26,5)	0.000669	(25,6)

experimentally found configuration was the ground state. Since it will turn out that often a metastable state has a higher probability this was not necessarily the case. For this reason the $N = 190$ cluster is investigated theoretically with respect to the occurrence probabilities in Section 6.4.3.

6.4. MD simulation results

In this section the results of the first-principle MD simulations are presented. The main parameters determining the occurrence frequencies of different metastable states for a given N are the screening parameter κ and the friction coefficient ν. The dependence on κ and ν is therefore discussed in detail. As an example of particular interest the parameter values of dusty plasma experiments will be considered which are in the range of $\kappa \approx 0.4 \ldots 1.0$ [3]. This case will be dealt with in Section 6.6.

The effect of the damping rate on the occurrence probabilities is discussed first. It will turn out that with a properly chosen rate one can produce very general results for different screening lengths which do not depend on the exact chosen damping coefficient and hold for any rate in the overdamped limit. The effect of screening will then be examined in the following section.

6.4.1. Effect of friction

A typical simulation result is shown in Fig. 6.2. For slow cooling ($\nu = 0.05$) the particles are not hindered by friction and can move according to the interparticle and confinement forces. They continuously lose kinetic energy until they are trapped in a local minimum of the potential energy U. Here they are further being damped until the simulation is stopped. It is interesting to see that there exist more metastable states than different shell occupations, as was first observed in Ref. [30], see also Ref. [32]. Details are given in Table 6.1.

In the case of strong damping ($\nu = 5.3$) the situation is different. Here the particles are readily slowed down after the initialization process in the box. Their motion is strongly

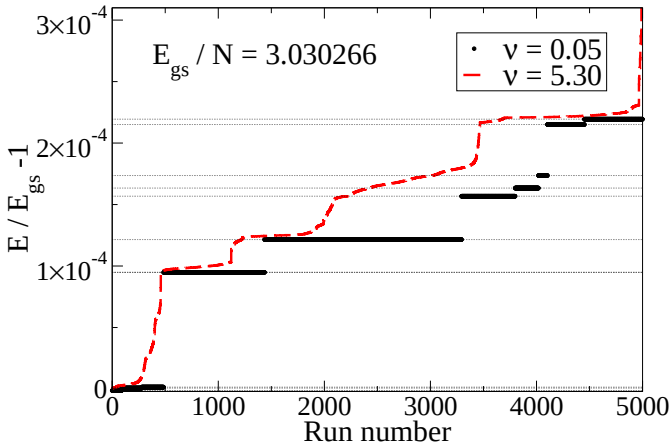

Figure 6.2.: *Stationary states observed in the MD simulations for* $N = 31$, $\kappa = 1.4$ *and* $\langle E_{\mathrm{kin}}^{\mathrm{min}} \rangle = 10^{-8}$. *The runs are sorted by the energy or the stationary state, see also Table 6.1.* E_{gs} *denotes the ground state energy. For slow cooling (black bars,* $\nu = 0.05$*) one can clearly see distinct states which correspond to the horizontal lines. The length of the bold lines is proportional to the occurrence probabilities. In the case of strong friction (red, dashed line,* $\nu = 5.3$*) the particles often lose their kinetic energy before they can settle into the equilibrium positions and the fine structure (different states with the same shell configuration) cannot be resolved.*

affected by friction and interrupted even before they may be trapped in a local minimum. If condition (A) is used to stop the simulation it is not clear if the particles are in a stable state. The reason is that due to the rapid damping they can be sufficiently slowed down even though they are not in a potential minimum but on a descending path and would reach the stable configuration at a later time.

Fig. 6.3 shows the influence of friction on the occurrence probabilities in more detail. For fixed screening the probability of finding the ground state configuration increases when the friction coefficient is decreased. Here the particles are cooled down more slowly and it is more likely that they reach the system's true ground state. During the cooling process they still have a sufficiently high kinetic energy and time to escape from a local minimum until the force on each particle vanishes.

In the case of strong friction the particles can fall into a nearby minimum and leaving it becomes more difficult due to the rapid loss of kinetic energy. The typical simulation time until the forces are small enough is longer than for intermediate friction strength. Once cooled down the particles are pushed along the gradient of the potential energy surface until they reach a stable state. Thus the results can depend on how far the system's temperature is decreased. One can see that for $\nu > 2$, i.e. in the overdamped regime, the probabilities have practically saturated. For fast cooling, i.e. large friction, metastable states can occur with a comparable or even higher probability than the ground state.

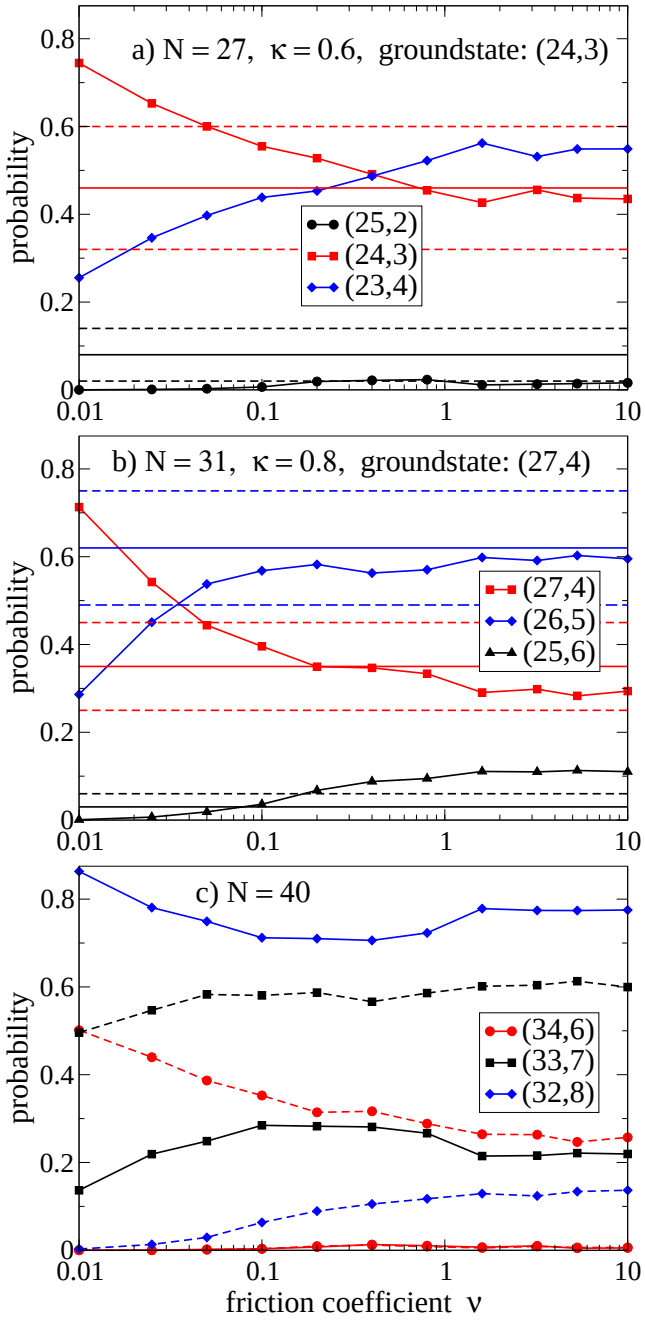

Figure 6.3.: *Effect of friction on the occurrence probabilities obtained with condition (B) for three different numbers of particles. In a) and b) horizontal solid and dashed lines indicate experimental mean and standard deviation, respectively [3]. For $N = 27$ the experimental values for the clusters (23,4) and (24,3) are the same. In c) solid lines indicate Yukawa interaction with $\kappa = 1.0$ [ground state (32,8)] whereas dashed lines show results for Coulomb interaction [ground state (34,6)]. In all cases slow cooling favors the ground state over metastable states.*

The $N = 40$ cluster shows a qualitatively different behavior compared to the $N = 27$, 31 clusters. In the case of $\kappa = 1.0$ the lines corresponding to different configurations do not intersect and the ground state is the most probable state regardless of the damping coefficient. In contrast, in the Coulomb limit $\kappa = 0$, the most probable state is always a metastable state, except for very small friction, $\nu \leq 0.01$.

The dusty plasma experiments of Yukawa balls are performed in the overdamped regime, i.e. here ν is of the order of $3 - 6$ [3]. Since in this limit the probabilities depend only very weakly on the damping rate the results presented in the next section for $\nu = 3.2$ should hold for any such damping coefficient. Even though this was shown only for a few examples this should also hold for other particle numbers and screening lengths.

6.4.2. Effect of screening

The screening dependence of the ground state shell configurations of spherical Yukawa clusters in the absence of damping has been analyzed in Ref. [29]. The general trend is that increased screening favors ground state configurations with more particles on the inner shell(s). A systematic analysis in a large range of particle numbers and screening parameters [33] confirms this trend (see Section 3.3). Here this analysis is extended to spherical crystals in the presence of damping and the screening dependence of the occurrence probability of metastable states is considered.

For a fixed friction coefficient in the overdamped limit the effect of screening is shown in Fig. 6.4. The different ground state configurations are indicated by the numbers with arrows in the figures. As in the undamped case, at some finite value of κ, a configuration with an additional particle on the inner shell becomes the ground state. Consider now the probability to observe the ground and metastable states. For weak screening the ground states (27,4) and (24,3) are the most probable states in the cases $N = 31$ and $N = 27$, respectively. At the same time in both cases, the probability of the configuration with one more particle on the inner shell grows with κ, until it eventually becomes even more probable than the ground state. Note that this occurs much earlier (at a significantly smaller value of κ) than the ground state change. For $N = 31$ this trend is observed twice: the probability of the configuration (26,5) first increases with κ and reaches a maximum around $\kappa \approx 1$. For $\kappa > 2$ this configuration becomes less probable than the configuration (25,6), i.e. again a configuration with an additional particle on the inner shell becomes more probable with increased screening.

Different behavior is observed for the $N = 40$ cluster where the ground state for weak screening (34,6) is never the most probable state. For large screening, $\kappa \geq 0.6$, the new ground state (32,8) has the highest probability, but this happens only substantially later (for larger κ) after this state has become the energetically lowest one. This is due to the existence of a third state (33,7) which has the highest probability for $\kappa \leq 0.6$, although it never has the lowest energy.

Fig. 6.5 shows the states with the highest probability for a wide range of particle numbers. The trend, that increased screening leads to a higher occupation of inner shells,

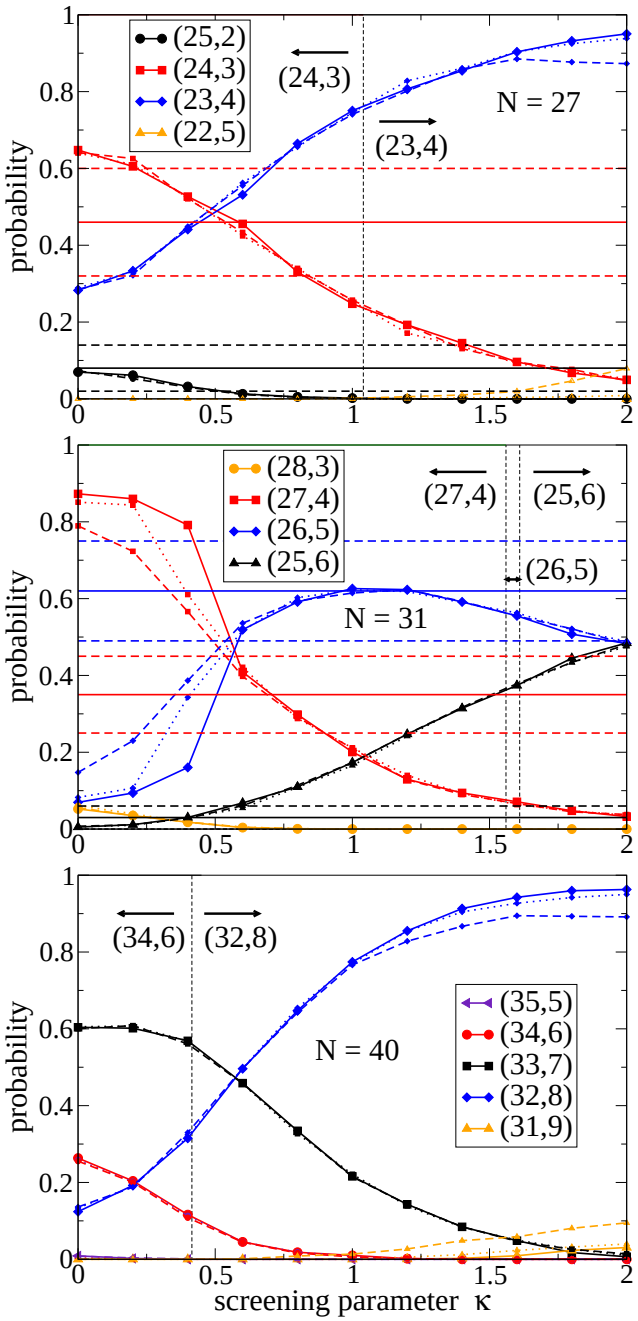

Figure 6.4.: *Effect of screening for $\nu = 3.2$. Solid lines show the results obtained with condition (B) while dotted and dashed lines indicate use of condition (A) with $\langle E_{\mathrm{kin}}^{\mathrm{min}} \rangle = 10^{-8}, 10^{-7}$, respectively. Arrows show the ground state configuration to the left or right from the vertical line. Where available horizontal solid and dashed lines indicate experimental mean and standard deviation [3]. For the $N = 27$ cluster the experimental values for the configurations (23,4) and (24,3) are the same.*

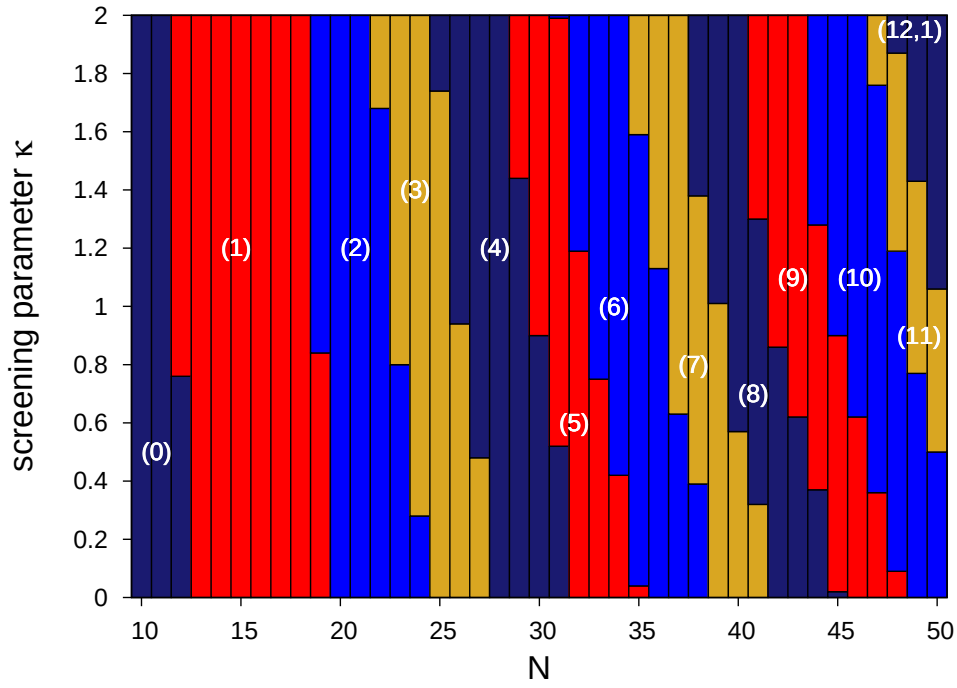

Figure 6.5.: *Most probable states as found in the MD simulations, obtained with a friction coefficient* $\nu = 3.2$ *and condition (B). Numbers in brackets denote the occupation of the innermost shell.*

is also observed here. This figure, together with Fig. 3.2 for the ground states, could be relevant for future experiments if one specifically wants to study states with a certain configuration and their screening dependence.

Comparison with Fig. 3.2 yields some interesting findings. In most cases the ground state itself is the most probable state or has one particle less on the inner shell than the most probable state. However, exceptions from this rule can be found. For 31 particles there exists an interval of the screening parameter where the ground state has more particles on the inner shell than the most probable state. This can also be observed for $N = 11, 26, 30, 33, 34, 40 - 42, 47 - 50$. In the case $N = 38$ the most probable state can have *two* more particles on the inner shell than the ground state. These 'anomalies' often arise from those in Fig. 3.2, especially from those where the ground state changes by two particles as κ is increased. Such a case has already been discussed for $N = 40$. In contrast, the shell filling mechanism in Fig. 6.5 is strictly monotonic upon increase of κ and N. Anomalous behavior is only observed for $N = 47 - 49$ and large screening where adding one particle gives rise to a configuration change involving two particles. Here the inner shell configuration of the most probable state changes from $(11, 0) \rightarrow (12, 1)$.

Summarizing, the observations confirm that in spherical Yukawa clusters the ground state is not necessarily the most probable state. Often, a metastable state with more particles on the inner shell is observed substantially (in some cases up to five times) more frequently. Further, increased screening tends to favor states with more particles on the inner shell. The interaction range and thus the effective size of the particles is decreased so they can be more closely packed. In addition the potential energy is lower near the center of the trap. A more detailed explanation for this behavior will be given in Section 6.5 by using an analytical model for the partition function.

Before doing this we comment on the technical details which are important in the present MD simulations: For certain intervals of the screening parameter the results for the probabilities depend on how far the system is cooled down. Here one state (generally the ground state) is favored over another the smaller $\left\langle E_{\mathrm{kin}}^{\mathrm{min}} \right\rangle$ is chosen. This also means increasing the mean simulation time. As discussed before the particles are heavily damped and lose their initial kinetic energy on a short time scale. Their motion is then determined by the shape of the energy surface. Using condition (B) to terminate the simulation one obtains converged results where the particles have reached a local minimum. Thus if the simulation was continued the configuration would remain the same. This is quite similar to the experimental procedure which is explained in detail in Ref. [79]. There the cluster is also given a long equilibration time to reach a stable state.

6.4.3. Results for $N = 190$

The results of MD simulations for $N = 190$ are given in Table 6.2 and Fig. 6.6. They are obtained in the same fashion as before in the overdamped limit with $\nu = 3.2$ and condition (B).

Since the simulations require a long run time the clusters are only cooled down 600 times, which makes the absolute values of the probabilities less reliable than before. The number of different states shown in Tab. 6.2 will only be a lower limit. The most probable state however can usually be clearly identified since it has a relatively high probability, keeping in mind the large number of different configurations. Only for $\kappa = 0.3$ there are two states with almost the same probability.

Fig. 6.6 shows the dependence of the shell occupation on the screening parameter. While on the outermost shell the most probable state has a smaller or equal number of particles than the ground state, the opposite is usually the case for the inner shells. The trend of a higher occupation of inner shells with increased screening also holds for this larger cluster. The relative deviations between the occupation of the most probable state and the ground state are rather small, except for the inner shell with only a few particles. The configuration found in the experiments has a non-zero probability only for a small interval of the screening parameter $0.4 \leq \kappa \leq 0.7$. The implications of these findings for previous results are discussed in Section 6.6.1.

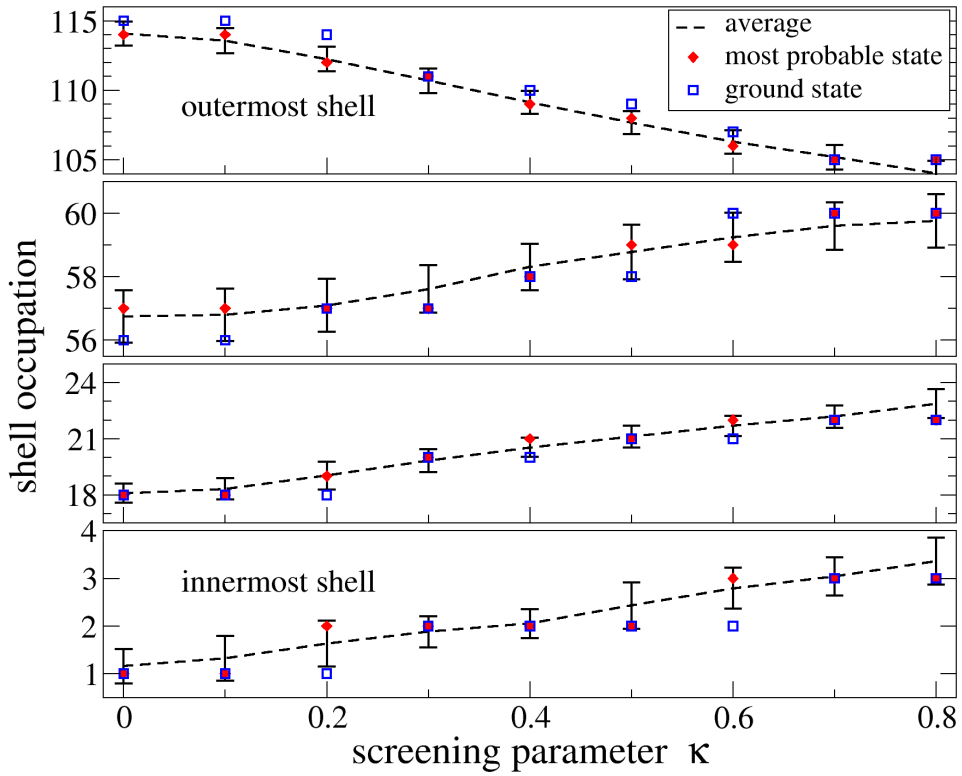

Figure 6.6.: *Ground state, mean shell configuration with standard deviation and most probable configuration in the MD simulations for* $N = 190$ *with* $\nu = 3.2$.

κ	# config.	ground state	most probable state m	$P(m)$	P(107,60,21,2)
0.0	≥ 30	(115,56,18,1)	(114,57,18,1)	0.33	0
0.1	≥ 29	(115,56,18,1)	(114,57,18,1)	0.25	0
0.2	≥ 26	(114,57,18,1)	(112,57,19,2)	0.18	0
0.3	≥ 30	(111,57,20,2)	(111,57,20,2)*	0.29	0
0.4	≥ 30	(110,58,20,2)	(109,58,21,2)	0.27	<0.01
0.5	≥ 25	(109,58,21,2)	(108,59,21,2)	0.23	0.11
0.6	≥ 29	(107,60,21,2)	(106,59,22,3)	0.30	0.07
0.7	≥ 35	(105,60,22,3)	(105,60,22,3)	0.36	0.01
0.8	≥ 29	(105,60,22,3)	(105,60,22,3)	0.17	0

Table 6.2.: *Results of MD simulations for* $N = 190$ *with* $\nu = 3.2$. *Shown is the number of different configurations found in the simulations, the ground state configuration, the most probable state, its probability and the probability of the experimentally found configuration (107,60,21,2). *) P(110,58,20,2)=0.28.*

6.5. Analytical theory of stationary state probabilities

6.5.1. Harmonic approximation

The analytical approach to calculating the occurrence probabilities is based on the classical canonical partition function $Z(T, \omega_0, N)$. Instead of the dependence on volume (or density) as in a homogeneous system, here thermodynamic quantities depend on the confining strength ω_0. The partition function can be evaluated analytically in the harmonic approximation, see e.g. Ref. [78]. Here the potential energy of a given state is expanded around a local minimum with energy E_s^0, where s denotes the ground or a metastable state. It can be written as

$$U_s \approx E_s^0 + \frac{1}{2} \sum_{i,j=1}^{N} \sum_{\alpha,\beta=1}^{3} \left. \frac{\partial^2 U(\mathbf{r})}{\partial \mathbf{r}_{i,\alpha} \partial \mathbf{r}_{j,\beta}} \right|_{\mathbf{r}=\mathbf{r}^{0s}} \delta\mathbf{r}_{i,\alpha} \delta\mathbf{r}_{j,\beta}, \tag{6.3}$$

where $\mathbf{r}^{0s} = (\mathbf{r}_1^{0s}, \ldots, \mathbf{r}_N^{0s})$ denotes the $3N$-dimensional vector of the particles' equilibrium positions and $\delta\mathbf{r}_{i,\alpha} = \mathbf{r}_{i,\alpha} - \mathbf{r}_{i,\alpha}^0$ the displacement vector. Transforming to normal coordinates $\xi_{s,i}$ this turns into a sum of decoupled harmonic oscillators

$$U_s \approx E_s^0 + \frac{1}{2} \sum_{i=1}^{f} m\omega_{s,i}^2 \xi_{s,i}^2, \quad f = 3N - 3. \tag{6.4}$$

The eigenfrequencies $\omega_{s,i}$ are the square roots of the eigenvalues of the Hessian matrix

$$U_{(i\alpha),(j\beta)} = \left. \frac{\partial^2 U(\mathbf{r})}{\partial \mathbf{r}_{i,\alpha} \partial \mathbf{r}_{j,\beta}} \right|_{\mathbf{r}=\mathbf{r}^{0s}}.$$

The expansion (6.4) includes the particles' three center of mass oscillations in the trap with $\omega = 1$ (in units of ω_0). Furthermore it is assumed that the vibrational and the three rotational modes of the whole system ($\omega = 0$) are decoupled, the latter are, therefore, eliminated from the sum (6.4). In the principal axes frame the rotational kinetic energy can then be expressed as

$$T_s^{\mathrm{rot}} = \sum_{i=1}^{3} \frac{L_{s,i}^2}{2I_{s,i}},$$

with angular momenta $L_{s,i}$ and constant principal moments of inertia $I_{s,i}$. In this approximation the full energy of the state s is, to second order in the displacements,

$$E_s = E_s^0 + \sum_{i=1}^{f} \left\{ \frac{p_{\xi_{s,i}}^2}{2m} + \frac{m}{2} \omega_{s,i}^2 \xi_{s,i}^2 \right\} + \sum_{i=1}^{3} \frac{L_{s,i}^2}{2I_{s,i}}. \tag{6.5}$$

The first term in parentheses denotes the vibrational kinetic energy T_s^{vib}.

The harmonic approximation is only applicable for low temperatures (or strong coupling) when the particles oscillate around the equilibrium positions with a small amplitude.

6.5.2. Partition function

The general form of the classical canonical partition function is

$$Z_s = \frac{n_s}{(2\pi\hbar)^{3N}} \int_{-\infty}^{\infty} dp^{3N} dq^{3N} e^{-\beta H^s(p_i,q_i)}. \tag{6.6}$$

Here it is written for a general Hamiltonian $H^s(p_i, q_i)$ with $3N$ degrees of freedom, generalized coordinates q_i and conjugate momenta p_i. Since in the present case the energy contributions are independent it can be factorized according to

$$Z_s = n_s Z_s^{\mathrm{int}} Z_s^{\mathrm{vib}} Z_s^{\mathrm{rot}} \tag{6.7}$$

with the internal partition function

$$Z_s^{\mathrm{int}} = e^{-\beta E_s^0} \tag{6.8}$$

and the degeneracy factor n_s calculated as

$$n_s = \frac{N!}{\prod_{i=1}^{L} N_i^s!}, \tag{6.9}$$

where L is the number of shells and N_i^s the occupation number of shell i with $\sum_{i=1}^{L} N_i^s = N$. The degeneracy factor n_s denotes the number of possibilities to form a configuration with shell occupation $(N_1, N_2, \ldots, N_L)$ from distinguishable particles.

Z_s^{vib} is the partition function for f independent harmonic oscillators while Z_s^{rot} is related to the rotational degrees of freedom. The results for the specific case with the energy given by Eq. (6.5) can be found in [78, 80] and read

$$Z_s^{\mathrm{vib}}(T) = \left(\frac{k_B T}{\hbar \Omega_s}\right)^f, \tag{6.10a}$$

$$Z_s^{\mathrm{rot}}(T) = \left(\frac{2\pi^{1/3} k_B T \bar{I}_s}{\hbar^2}\right)^{3/2}. \tag{6.10b}$$

The expressions include the mean geometric eigenfrequency $\Omega_s = (\prod_{i=1}^{f} \omega_{s,i})^{1/f}$ and the mean moment of inertia $\bar{I}_s = (I_{s,1} I_{s,2} I_{s,3})^{1/3}$. Details on the derivation are given in Appendix B.[3]

To obtain the total partition function $Z(T, \omega_0, N)$ the contributions of all M (metastable) states are summed up, i.e.

$$Z = \sum_{\sigma=1}^{M} Z_\sigma.$$

[3] The eigenfrequencies $\omega_{s,i}$ are calculated by using a Mathematica notebook created by Christian Henning.

Table 6.3.: *Mean shell radii R_1, R_2 of first and second shell for states observed in the MD simulations for $N = 27$ and $\kappa = 0.6$. The relative statistical weight $\tilde{q}_s = (\bar{I}_s/\bar{I}_1)^{3/2}$ caused by different moments of inertia can be neglected in the computation of the probabilities since $\tilde{q}_s \approx 1$ for all states.*

state s	configuration	R_2	R_1	$\tilde{q}_s$
1	(24,3)	1.6175	0.5977	1
2	(23,4)	1.6413	0.6963	1.0009
3	(23,4)	1.6413	0.6957	1.0009
4	(25,2)	1.5935	0.4542	1.0004
5	(25,2)	1.5934	0.4543	1.0004

6.5.3. Probability of stationary states

Collecting the results of Section 6.5.2, the stationary state probabilities are given by

$$P_s = \frac{Z_s}{Z} = \frac{Z_s}{\sum_{\sigma=1}^{M} Z_\sigma}. \tag{6.11}$$

For the clusters of interest with $27 - 40$ particles the moments of inertia for different states are equal to a good approximation (cf. Table 6.3 for $N = 27$) and can be canceled. Similar behavior is observed for $N = 31$, 40. For low particle numbers, $N \lesssim 10$, they should be included, since here a slight change of the configuration can alter the moment of inertia by a significant amount, but this is not of importance for the present analysis.

Using Eqs. (6.10) one obtains from Eq. (6.11)

$$P_s \approx \frac{n_s \Omega_s^{-f} e^{-\beta E_s^0}}{\sum_{\sigma=1}^{M} n_\sigma \Omega_\sigma^{-f} e^{-\beta E_\sigma^0}}. \tag{6.12}$$

To avoid computation of the full partition function [denominator of Eq. (6.12)] it is advantageous to compute probability ratios of two states s and s',

$$\begin{aligned} \frac{P_s}{P_{s'}} &= \frac{n_s}{n_{s'}} \left(\frac{\Omega_{s'}}{\Omega_s}\right)^f \left(\frac{\bar{I}_s}{\bar{I}_{s'}}\right)^{3/2} e^{-\beta(E_s^0 - E_{s'}^0)} \\ &\approx \frac{n_s}{n_{s'}} \left(\frac{\Omega_{s'}}{\Omega_s}\right)^f e^{-\beta(E_s^0 - E_{s'}^0)}. \end{aligned} \tag{6.13}$$

Thus the probability ratio of two states depends on three factors: their energy difference $E_s^0 - E_{s'}^0$, the ratio of the degeneracy factors $n_s/n_{s'}$ and the *inverse* ratio of their mean eigenfrequencies $\Omega_{s'}/\Omega_s$.

The Boltzmann factor $e^{-\beta(E_s^0 - E_{s'}^0)}$ gives preference to states with a low energy. For low temperatures it will be the most dominant factor but it becomes less important for higher temperatures when $k_B T \gg E_{s'}^0 - E_s^0$ and $e^{-\beta(E_s^0 - E_{s'}^0)} \approx 1$.

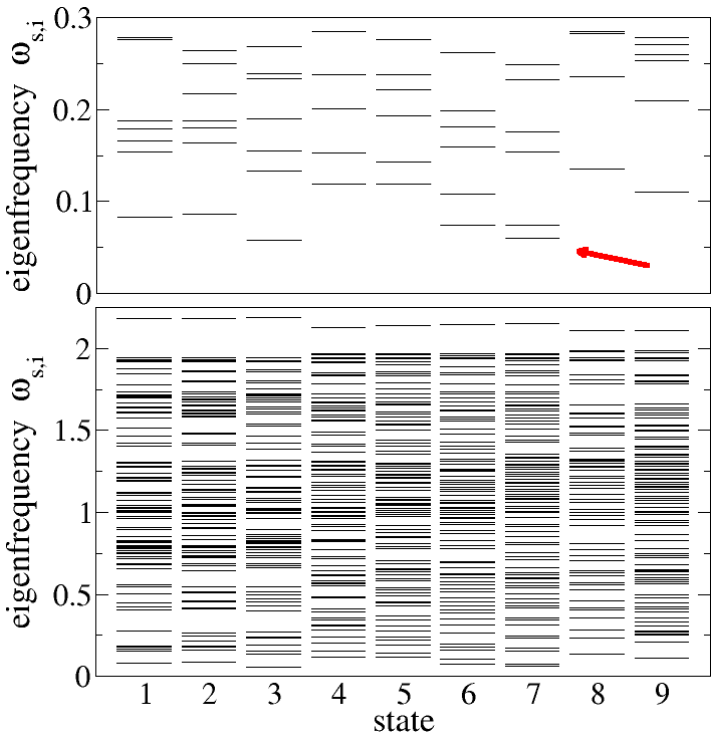

Figure 6.7.: *Spectrum of the eigenfrequencies for the 9 states shown in Table 6.5. The top figure shows the lowest modes in more detail.*

According to Eq. (6.9) the degeneracy factor assigns a large statistical weight to states with more particles on inner shells. As an example, for $N = 27$, one has $n_{(25,2)}/n_{(23,4)} = \frac{23!4!}{25!2!} = 1/50$. The configuration with only 2 particles on the inner shell is suppressed due to a lower degeneracy factor contrary to the states with an inner shell consisting of 4 particles, see also Table 6.4. The reason is that there exist more combinatorial possibilities to construct configurations when the difference between the single shell occupation numbers is small. For $N = 31$ (Table 6.6) this ratio can be even larger. This shows that (even for low temperatures) this factor can strongly influence the occurrence probabilities.

In the MD simulations one observes several states with the same shell configuration but different energies. Their energy difference can be as large as between states with different configurations (cf. Table. 6.1). In Eq. (6.11) all states with the same shell configuration are added with the same degeneracy factor.

Let us now consider the effect of the mean eigenfrequency, i.e. the effect of the local curvature of the potential energy surface. Written out explicitly, using Eq. (6.13), this factor reads

Table 6.4.: *Energy difference between metastable states and the ground state (ground state energy given in italic numbers) that are used to compute the partition function for $N = 27$ and $\kappa = 0.6$. Also shown is the relative statistical weight $\tilde{n}_s = n_s/n_1$ and the statistical weight due to the eigenfrequencies $\tilde{w}_s = (\Omega_1/\Omega_s)^f$ compared to the ground state.*

state s	configuration	$\Delta E_s/N$	$\tilde{n}_s$	$\tilde{w}_s$
1	(24,3)	*4.732856(4)*	1	1
2	(23,4)	0.001622(1)	6	0.24
3	(23,4)	0.001870(5)	6	0.67
4	(25,2)	0.004993(0)	3/25	14
5	(25,2)	0.004997(3)	3/25	3.3

$$\left(\frac{\Omega_{s'}}{\Omega_s}\right)^f = \frac{\prod_{i=1}^{f} \omega_{s',i}}{\prod_{i=1}^{f} \omega_{s,i}}, \tag{6.14}$$

i.e. it is the inverse ratio of the products of the eigenfrequencies. The main contribution here usually arises from the lowest eigenfrequencies. This can be seen in Fig. 6.7 showing the spectrum for the states of the cluster with $N = 31$, $\kappa = 0.8$. State #7 has two very low eigenfrequencies [cf. Fig. 6.7, red arrow] which strongly increase its statistical weight (see also Table 6.5).

For two states with the same shell configuration one has $n_s = n_{s'}$, and the probability ratio is only determined by their energy difference and eigenfrequencies. Even though a state has a higher energy it can have a higher probability provided it has a lower mean eigenfrequency. Fig. 6.8 shows the effect for $N = 27$, for the states listed in Table 6.4. The physical explanation of the eigenfrequency factor is very simple: states with low eigenfrequencies have a broad (flat) potential energy minimum and thus a larger phase space volume of attraction for the trajectories of N particles. Thus initially randomly distributed particles will have a higher probability to settle in a minimum with small Ω_s compared to another minimum (when the energies and degeneracy factors are similar).

Because the harmonic approximation only describes a minimum's local neighborhood one should be aware that this could overestimate the probability of states with broad minima and low escape paths [78], which are not taken into account in this approximation. This could be improved by changing the limits for the position integration in Eq. (6.6) according to the potential barrier height and the temperature. This was done for 2D clusters in Ref. [81] but requires knowledge of the barrier heights. This is not essential for the present analysis. Finally, the value of $\tilde{w}_s$ is sensitive to numerical errors in the computation of the eigenvalues of the Hessians since the mean eigenfrequency is a product of $3N - 3$ single values. In the present results the error is estimated not to exceed 5 % which is sufficient for the analysis.

Table 6.5.: *Same as Table 6.4 for $N = 31$ and $\kappa = 0.8$.*

state s	configuration	$\Delta E_s^0/N$	$\tilde{n}_s$	$\tilde{w}_s$
1	(27,4)	*4.397858(8)*	1	1
2	(27,4)	0.000008(7)	1	0.82
3	(27,4)	0.000035(8)	1	1.7
4	(26,5)	0.001810(1)	27/5	0.84
5	(26,5)	0.001850(9)	27/5	1.4
6	(26,5)	0.002000(0)	27/5	5.3
7	(26,5)	0.002091(6)	27/5	9.7
8	(25,6)	0.003583(7)	117/5	1.4
9	(25,6)	0.003586(7)	117/5	1.1

6.5.4. Analytical results and comparison with Monte Carlo simulations

Let us now come to the results of the analytical model and compare them to Monte Carlo simulations which were explained in Section 6.3.2. The MC results have first-principle character, in particular, they are not restricted to the harmonic approximation and fully include all anharmonic corrections. For $N = 27$ the MC results were additionally verified by a Langevin dynamics simulation using the SLO algorithm of Ref. [59], as explained in Section 4.3. Here the probabilities were obtained in an equilibrium calculation with a simulation time $t = 10^5\,\omega_0^{-1}$ by determining the configurations at fixed time intervals.

Results for three representative examples are shown in Fig. 6.9. The two examples $N = 27,\ \kappa = 0.6$ and $N = 31,\ \kappa = 0.8$ are chosen since these will turn out to be close to the situation in the dusty plasma experiments, see. Section 6.6. As a third example data for $N = 40$ with Coulomb interaction is presented. The input parameters of the analytical model, i.e. details on the (metastable) states are summarized in Tables 6.4–6.6. In Fig. 6.9 the occurrence probabilities are plotted as a function of temperature. This allows one to specifically study the effect of the depth of the potential energy minimum E_s^0. The latter effect should be dominant at low temperature, leading to a relatively high probability of the ground state. In contrast, this effect should become less important at high temperatures where the degeneracy factors and the eigenfrequency ratio should play a decisive role for the probabilities. This general trend is indeed observed in all three cases.

For $N = 27$, top part of Fig. 6.9, the effects of the degeneracy factor and the mean eigenfrequency act in opposite directions. While the state with 4 particles on the inner shell gains statistical weight by having a high degeneracy, this effect is almost compensated by narrow minima, and consequently a low $\tilde{w}_s$, cf. Tab. 6.4. Therefore, this state achieves comparable probability with the ground state (27,4) only at high temperatures $T \geq 0.03$ (in the MC simulation this is observed only for $T \geq 0.045$). For the configuration (25,2) the opposite is true. Here the degeneracy is low and the minima broad, but due to its high energy this configuration has a non-vanishing probability only for high

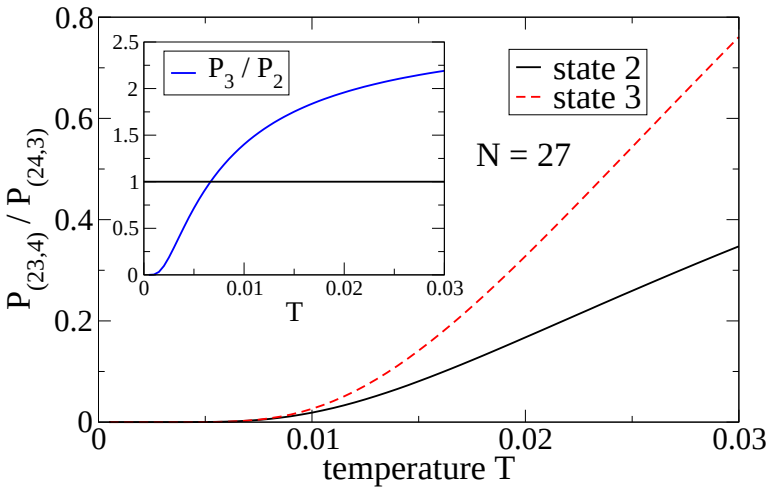

Figure 6.8.: *Probability of the two metastable states with configuration (23,4) compared to the ground state (24,3) for the Yukawa ball with $N = 27$. The inset shows the ratio of the probabilities for states 2 and 3 from Table 6.4 at low temperatures. Although state 3 has the same configuration and a higher energy the probability of finding state 3 is higher for $T \geq 0.007$ due to the effect of the eigenfrequencies.*

Table 6.6.: *Same as Table 6.4 for $N = 40$ and $\kappa = 0$ (Coulomb interaction).*

state s	configuration	$\Delta E_s^0/N$	$\tilde{n}_s$	$\tilde{w}_s$
1	(34,6)	*12.150162(9)*	1	1
2	(33,7)	0.001143(4)	34/7	2.3
3	(33,7)	0.001190(3)	34/7	2.8
4	(33,7)	0.001236(9)	34/7	8.3
5	(32,8)	0.001862(8)	561/28	13
6	(32,8)	0.001863(1)	561/28	3.5
7	(32,8)	0.003482(4)	561/28	6.7
8	(35,5)	0.004201(7)	6/35	5.2
9	(35,5)	0.004392(7)	6/35	32

temperatures $T \geq 0.03$. A stable state with configuration (22,5) could not be found in the simulations.

The situation for $N = 31$, central part of Fig. 6.9, is different. Here all metastable states have a higher degeneracy factor than the ground state configuration. In addition all states further gain statistical weight because of broad minima, except for state $s = 4$, cf. Tab. 6.5. Thus one should expect that metastable states have a high probability even at low temperatures. This is indeed observed in the model and the MC simulations already below $T = 0.02$.

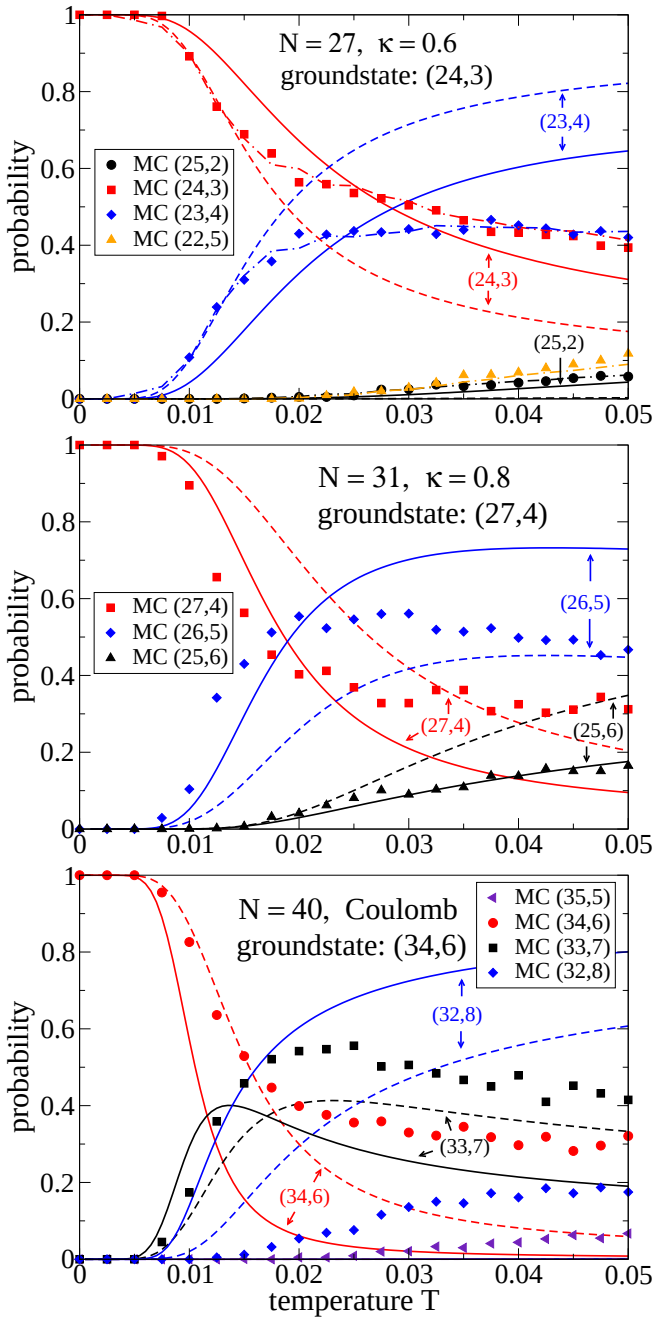

Figure 6.9.: *Analytical theory compared to MC results. The solid lines show the probabilities for the indicated configurations as obtained from Eq. (6.11). The dashed lines neglect the statistical weight factor caused by the eigenfrequencies, i.e. here* $\Omega_s \equiv 1$ *for all states. For* $N = 27$ *the dashed/dotted lines indicate the results of Langevin dynamics simulations. Analytical results for the configurations (22,5) and (35,5) are not available or too low to be apparent in the figure, respectively.*

In the third case, $N = 40$, bottom part of Fig. 6.9, one generally sees the same trend. The metastable state (33,7) has a high degeneracy and frequency factor, cf. Tab. 6.5, and thus it becomes more probable than the ground state already for $T \geq 0.01$ (0.015 in the MC simulations).

Let us now compare the analytical and MC results in more detail. Good agreement is found for $N = 31$ up to $T \sim 0.02$, cf. full lines and symbols. For $N = 27$ the agreement between MC and the analytical theory is good for $T < 0.012$ but only if the effect of the eigenfrequencies is neglected, cf. dashed lines. With eigenfrequencies included the theory shows deviations for low temperatures but better agreement for higher temperatures. For the cluster with 40 particles moderate agreement is observed for the configurations (34,6) and (33,7) up to $T = 0.015$ whereas the deviations from MC for the remaining two are rather large. This overall agreement is quite satisfactory keeping in mind that the melting temperature of these clusters is typically below $T = 0.015$ [64, 82, 83].

The discrepancies are due to the limitations of the simple harmonic model [the good agreement between the completely independent MC and Langevin MD results for $N = 27$, cf. top part of Fig. 6.9, confirms the reliability of the simulations]. Since the discrepancies are growing with temperature, the main reason is probably the neglect of anharmonic effects. In some cases, when the barriers of the potential energy surface are low, these effects might already occur at low temperatures. Changing the limits of allowed particle motion in the integration of Eq. (6.6) may help reduce the deviations. A further reason for deviations from MC results could be an insufficient number of stationary states being taken into account. It is not clear if all stationary states have been found (they were pre-computed with MD simulations) and used in the partition function. To ensure a high probability more than 10^4 independent runs were performed. For example, for the cluster with 40 particles one observes 9 states, but it was difficult to identify the states with 5 particles on the inner shell because they were found only a few times and were energetically close. The larger number of states given in Ref. [32] also suggests that a few states could be missing. Nevertheless, the effect originating from these states should give only a small statistical contribution to the probabilities.

6.6. Comparison with dusty plasma experiments

To compare with the experiments explained in Section 6.2 the relation between the chosen system of units and the experimental parameters must be establish. The temperature unit $k_B T_0 = E_0 = (\alpha Q^4/2)^{1/3}$ [in SI units $E_0 = (\alpha Q^4/32\pi^2\epsilon_0^2)^{1/3}$] depends on the trap parameter $\alpha = m\omega_0^2$ and the dust charge. Since the charge is not known very accurately the errors could be rather large. With $Z = 2000\,e$ and $\alpha = 5.2 \times 10^{-11}\,\mathrm{kg\,s^{-2}}$ given in Ref. [3], room temperature (300 K) corresponds to $T_{\mathrm{room}} \approx 0.0015$. Also, the experimental screening parameter is known only approximately. From previous comparisons with simulations [29] it is expected to be in the range of $0.5 < \kappa < 1$.

The reported measurements on the probability of metastable states for the clusters with $N = 27$ and $N = 31$ [3] will now be used for comparison with the MD and MC simulations and the analytical model. More recent experimental results are presented in Ref. [79].

6.6.1. MD results vs. experiment

The molecular dynamics simulations model a situation which is closest to the experiment. In contrast to the experiment which is performed at room temperature, the present simulations correspond to a Langevin dynamics simulation at $T = 0$ (the system is cooled to almost zero kinetic energy). The influence of the final temperature was verified by performing additional Langevin simulations for the cluster with 27 particles and $\kappa = 0.6$ with temperatures up to $T = 0.0035$ (Fig. 6.10), which is more than twice the experimental temperature. Apart from a finite temperature the simulations were done in the same way as explained in Section 6.3, but with a predefined simulation time. For high temperatures one has to pay attention to the time after which the configuration is determined since then transitions between states can easily occur. This can be seen in Fig. 6.9 where for $T > 0.01$ metastable states have a non-vanishing probability. In the present Langevin simulations a simulation time of $t_{\mathrm{end}} = 400\,\omega_0^{-1}$ was used, which corresponds to $t_{\mathrm{end}} \approx 10\,\mathrm{s}$ for a dust particle mass of $m = 3.3 \times 10^{-14}\,\mathrm{kg}$. No systematic deviation from the results at zero temperature can be observed. The slight deviations for the configurations (23,4) and (24,3) are probably due to the insufficiently long simulation time with the same explanation as given at the end of Section 6.4.2. This leads to the conclusion that for the present analysis an MD simulation without fluctuations and cooling towards zero temperature is adequate.

The data for comparison with the experimental results is shown in Figs. 6.3 and 6.4. The friction parameter in the experiments is expected to be in the range $\nu = 3 \ldots 6$ [3]. This means the system is overdamped and any value above $\nu = 2$ will not change the results significantly, cf. Fig. 6.3. So in Fig. 6.4 a value of 3.2 was used. The MD simulations agree well with the experiment in the case of screening parameters in the range $0.6 < \kappa < 0.8$ (for $N = 31$) and $0.4 < \kappa < 0.6$ ($N = 27$), for details cf. Tab. 6.7. The lower screening parameter in the latter case is a consequence of the lower plasma density in the experiment, compared to the conditions under which the cluster with 31 particles was produced. This was also found in the MD simulations performed in Ref. [3]. The present simulations, being much more extensive, confirm these results. It should be noted that this comparison allows one to determine the screening parameter in the experiment.

Comparison for the cluster with 190 particles

Unfortunately the occurrence probabilities of the $N = 190$ cluster have not been measured in the experiment. Previous comparisons between experiment and simulation were based on the ground state shell occupation [29], which coincides with the experimental

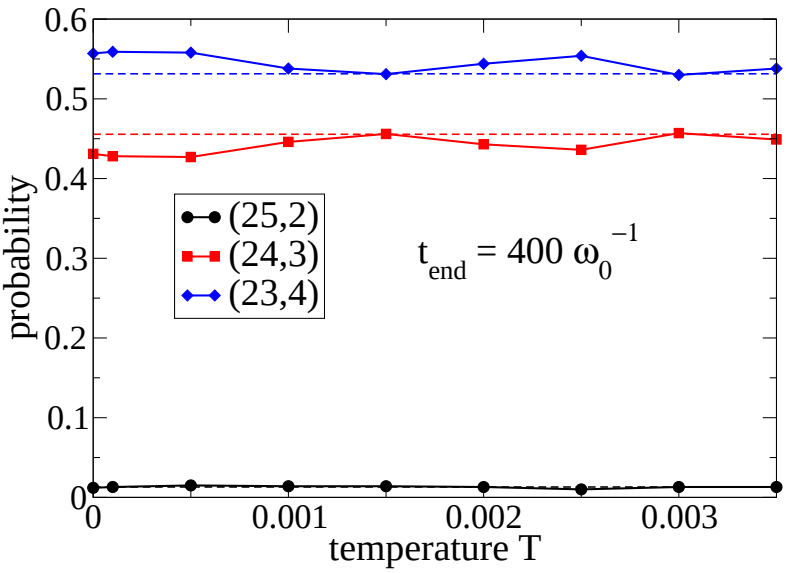

Figure 6.10.: *Langevin dynamics simulation for $N = 27$, $\kappa = 0.6$ and $\nu = 3.2$. Horizontal lines indicate results of Section 6.4.2, Fig. 6.4.*

configuration for $\kappa = 0.58 \ldots 0.63$. From Table 6.2 one can see that the experimental configuration has a non-vanishing probability only for $\kappa \approx 0.45 \ldots 0.65$ (with a maximal probability at $\kappa \approx 0.5$) which is in good agreement with the ground state considerations.

Since the probabilities have not been measured, one can only narrow down the possible values of the experimental screening to $0.45 \lesssim \kappa^{\mathrm{exp}} \lesssim 0.65$. This includes the previously considered interval where the experimental configuration is the ground state. However, also lower screening values are permitted here. This shows that determining the experimental screening parameter from a comparison with the ground state of the simulations may lead to a (systematic) error.

This is not surprising since often a state with more particles on the inner shell(s) than the ground state achieves a comparable or higher probability. The change of the configuration with the highest probability usually occurs prior to the change of the ground state configuration as κ is increased. In addition, finite temperature effects will play a more dominant role for large clusters since the energy differences between metastable states are much lower than for small clusters. This might further increase the probability of metastable states.

6.6.2. Analytical and MC results vs. experiment

A comparison of the analytical model and the MC simulations with the experiment is disappointing. From Fig. 6.9 it is evident that at room temperature the ground states

always have a probability of almost 100 % which is in striking contrast to the experiment and the MD results. This is not surprising since the dust comprises a dissipative system and the clusters are created under nonequilibrium conditions. In contrast, both Monte Carlo and the analytical model are based on the canonical partition function and assume thermodynamic equilibrium. Thus, at first sight, there seems to be no way to explain the experiment with the analytical model or with Monte Carlo methods. However, this is not true. As will be shown below, there is a way to apply equilibrium methods to the problem of metastable states.

6.6.3. Time scales of the cluster dynamics

Let us have a closer look at the nonequilibrium dynamics of the cluster during the cooling process. It is particularly interesting to analyze on what time scales the different relaxation processes occur. In a weakly coupled plasma there are three main time scales [84, 85]: first, the buildup of binary correlations which occurs for times shorter than the correlation time τ_{cor}, which is typically of the order of the inverse plasma frequency [86]. Second, the relaxation of the velocity distribution towards local equilibrium due to collisions, for $\tau_{\mathrm{cor}} \leq t \leq t_{\mathrm{rel}}$ (kinetic phase) and third, hydrodynamic relaxation, $t_{\mathrm{rel}} \leq t \leq t_{\mathrm{hyd}}$. This behavior has so far not been analyzed for strongly correlated Yukawa clusters.

To get first insight, the quantities of central interest are the kinetic energy and the velocity distribution function $f(v,t)$ of the cluster particles. These quantities are easily computed in the MD simulations of the cooling process, as explained in Section 6.4. To obtain the velocity distribution 420 runs with different randomly chosen initial conditions were performed and the data was collected for each time step. The results for the kinetic energy evolution and for $f(v_x,t)$ at six different times are shown in Fig. 6.11, parts a)–f) [the other velocity components show the same behavior]. The solid curves indicate the best fit to a Maxwellian, the obtained 'temperatures' are shown in Fig. 6.11 g) by the crosses.

Four main relaxation stages can be observed. Stages two to four are analogous to the ones discussed above. However, there is an additional stage at very short times which is due to strong friction effects in the present system:

1. $0 \leq t \leq 0.1$, initial stage: A rapid thermalization of the initial randomly chosen velocity distribution f_0 is observed which is due to strong friction in this overdamped system. This leads to the formation of a Maxwellian distribution even before the particles substantially 'feel' the confinement potential and binary forces.

2. $0.1 \leq t \leq 0.5$, correlation buildup: Rapid particle acceleration is observed which accompanies the build up of binary correlations in the initially random (uncorrelated) particle system. This is also seen in the appearance of superthermal particles, see Fig. 6.11, parts b) – d). This behavior is typical for any rapid change of the interparticle forces and proceeds on time scales of the order of the correlation time, see Refs. [86–88].

3. $0.5 \leq t \leq 1.3$, competition between correlations and dissipation: The kinetic energy increase saturates and cooling starts. This means, at $t \gtrsim 1$ correlation build up is finished and dissipation due to neutral gas friction dominates the behavior.

4. $t > 1.3$, local equilibrium: the mean kinetic energy decreases approximately exponentially, i.e. $\langle E_{\mathrm{kin}} \rangle(t) \propto e^{-2\gamma t}$ where the decay constant is found to be $\gamma \approx 0.65 \approx \nu/5$.

The behavior on the last stage resembles a single (Brownian) particle in a dissipative medium where γ is the velocity relaxation rate corresponding to a relaxation time of $t_{\mathrm{rel}} = \gamma^{-1} = 1.54$. In the case of Brownian particles, the velocity distribution rapidly relaxes towards a Maxwellian for $t \leq t_{\mathrm{rel}}$. At early times high velocities are efficiently suppressed by the high damping coefficient. The particles are then being accelerated towards the center of the trap and increasingly interact with each other giving rise to a non-thermal velocity distribution. The subsequent evolution towards a Maxwellian is evident in Figs. 6.11 d) – f) which is established around $t = 2.5$.

This allows to conclude that, after an initial period (phases 1 – 3), the cluster has reached an equilibrium velocity distribution and the subsequent cooling process, ultimately leading to freezing into a spherical Yukawa crystal, is well described by local thermodynamic equilibrium: the time-dependent velocity distribution is given by $f(v,t) \sim \exp\{-\frac{mv^2}{2k_B T(t)}\}$ with $k_B T(t) = 2\langle E_{\mathrm{kin}} \rangle(t)/3$. Thus, the system evolves from one equilibrium state to another which differ only by temperature.

6.6.4. Application of equilibrium theories to the probability of metastable states of Yukawa balls

Based on the results of Section 6.6.3, one can expect that equilibrium methods such as Monte Carlo or the analytical model are applicable to the final (fourth) relaxation stage. Thereby one has to use the equilibrium result for the current temperature $T(t)$. Using temperature dependent results such as in Fig. 6.9, allows one to reconstruct the time-dependence of various quantities from the known dynamics of the kinetic energy: $T(t) = T(t_{\mathrm{rel}}) e^{-2\gamma(t - t_{\mathrm{rel}})}$.

Now, the key point is that this local (time-dependent) Maxwellian is established long before the particles are in a strongly coupled state, i.e. the potential energy U of the trap and of the pair interaction does not exceed the thermal energy. For example, at $t \approx t_{\mathrm{rel}}$, the temperature is around 0.15, which is about a factor 100 higher than room temperature and one order of magnitude higher than the freezing point. In the case of very rapid cooling beyond the freezing point the particles will settle (with a certain probability) in the stationary state 's' and will not have time to escape it since further cooling removes the necessary kinetic energy (i.e. the escape probability will be low). This means that the decision about what stationary state the system will reach is made at a time when the system's temperature is close to the melting temperature.

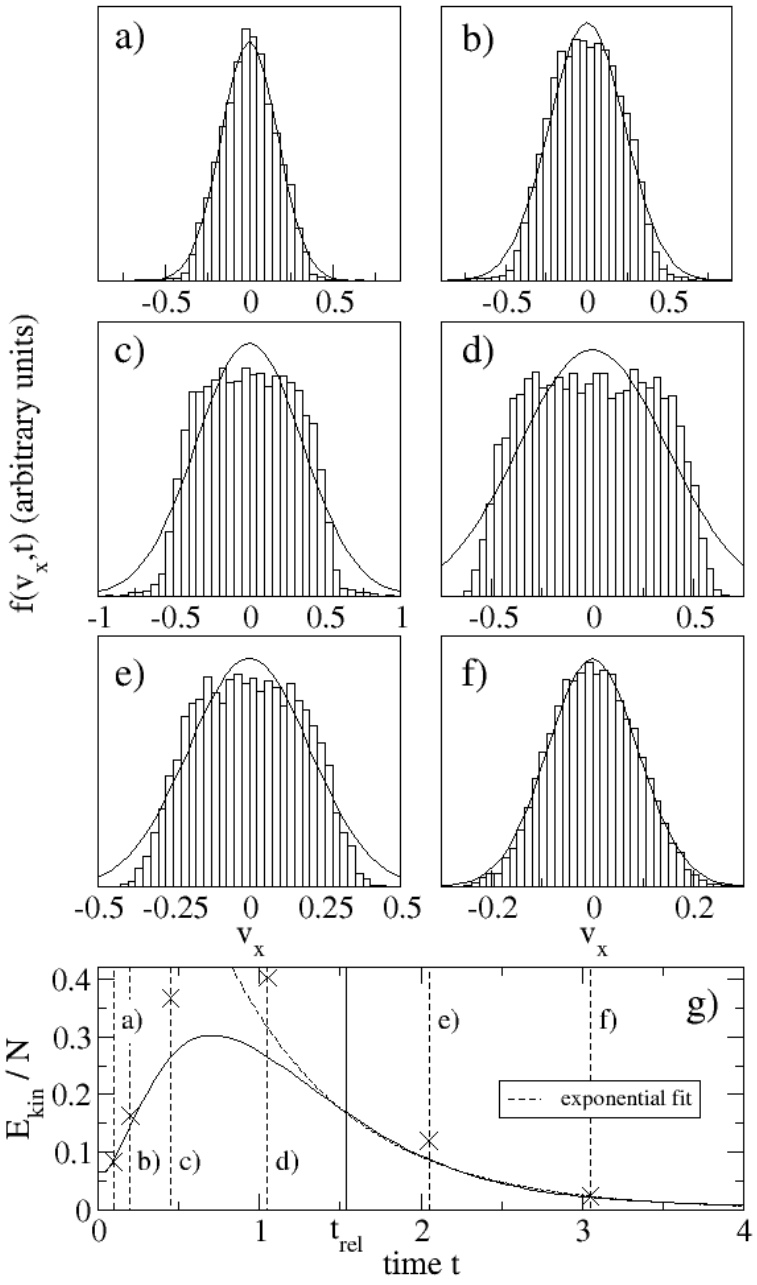

Figure 6.11.: *a) – f) Velocity distribution function $f(v_x, t)$ for different times [a): $t = 0.1$, b): $t = 0.2$, c) $t = 0.4$, d) $t = 1.0$, e) $t = 2.0$, f) $t = 3.1$, as indicated in h) by the vertical dashed lines.] for $N = 27$, $\kappa = 0.6$, $\nu = 3.2$. Solid lines show the best Maxwellian fit. The initial velocity distribution at $t = 0$ is chosen randomly and thermalizes rapidly until $t = 0.1$. g) Averaged kinetic energy as a function of time. Crosses denote the averaged kinetic energy obtained from the best fit using the equipartition theorem. The distributions are averaged over 420 MD runs.*

Table 6.7.: *Comparison of experimental results for $N = 27$ and $N = 31$ with MD and MC simulations (MC results are given for the temperatures $T = 0.02$ and $T = 0.04$). Also shown are the results of the analytical model ("AM") for $T = 0.02$ and with the Boltzmann factor being neglected ($T \to \infty$). For $N = 27$ ($N = 31$) the simulation results are shown for $\kappa = 0.6$ ($\kappa = 0.8$).*

$N = 27$	$P(24,3)$	$P(23,4)$	$P(25,2)$
Experiment	0.46 ± 0.14	0.46 ± 0.14	0.08 ± 0.06
MD	0.46	0.53	0.01
MC(0.02)	0.56	0.43	0.01
MC(0.04)	0.43	0.45	0.04
AM(0.02)	0.67	0.33	0.00
AM(∞)	0.12	0.64	0.24
$N = 31$	$P(27,4)$	$P(26,5)$	$P(25,6)$
Experiment	0.35 ± 0.10	0.62 ± 0.13	0.03 ± 0.03
MD	0.30	0.59	0.11
MC(0.02)	0.40	0.55	0.04
MC(0.04)	0.33	0.50	0.14
AM(0.02)	0.44	0.53	0.03
AM(∞)	0.02	0.60	0.38

Using this idea the probability of metastable states are computed from the Monte Carlo simulations for two temperatures $T = 0.02$ and $T = 0.04$, cf. Fig. 6.9 (at the higher temperature, due to intershell transitions, shell configurations can be identified only with an error of about 8%). The probability at $T = 0.02$ is also calculated within the analytical model. Finally the high-temperature limit is considered which is obtained by neglecting the Boltzmann factor in the probability ratios. The corresponding results are presented in Table 6.7. The overall agreement with the experiment is much better than the results for room temperature which confirms the correctness of the above arguments. Evidently, the Boltzmann factor is crucial and cannot be neglected, cf. last lines in Table 6.7. The best results are observed for temperatures around $T = 0.04$ which is about two to three times higher than the melting temperature where the system is in the moderately coupled liquid state. This shows that it is indeed possible to predict, at least qualitatively, the probabilities of metastable states in dissipative nonequilibrium Yukawa crystals within equilibrium models and simulations. This is possible in the overdamped limit as is the case in dusty plasmas.

6.7. Discussion

In summary simulation results for the probabilities of Yukawa balls with four different numbers of particles and a broad range of screening parameters and damping coefficients were presented. In addition the most probable states were determined for $0 \leq \kappa \leq 2$ and $10 \leq N \leq 50$. It was shown by extensive molecular dynamics and Langevin dynamics

simulations that the cooling speed (damping coefficient) strongly affects the occurrence probabilities of metastable states even if the interaction and the confinement remain the same. This is similar to the liquid solid transition in macroscopic systems where rapid cooling may give rise to a glass-like disordered solid rather than a crystal with lower total energy. The same scenario is also observed in the present finite crystals. While slow cooling leads predominantly to the lowest energy state, strong damping gives rise to an increased probability of metastable states. These states may have an up to five times higher probability than the ground state, which is fully consistent with the recent observation of metastable states in dusty plasma experiments [3]. These metastable states are not an artifact of an imperfect experiment or due to fluctuations of experimental parameters, but are an intrinsic property of finite Yukawa balls.

Furthermore it was shown that screening strongly alters the results compared to Coulomb interaction. Generally increased screening leads to a higher probability of states with more particles on inner shells due to the shorter interaction range. An analytical theory for the ground state density profile of a confined one-component Yukawa plasma [2, 38], cf. Section 3.3, also showed that decreasing the screening length (increasing κ) leads to a higher particle density in the center of the trap. This would correspond to a higher population of inner shells in the present case.

An analytical model based on the canonical partition function and the harmonic approximation for the total potential energy was presented. This model allowed for a physically intuitive explanation of the observed high probabilities of metastable configurations. The Boltzmann factor (which always favors the ground state relative to higher lying states), competes with two factors that favor metastable states: the degeneracy factor [favoring states with more particles on the inner shell(s)] and the local curvature of the potential minimum. Low curvature (low eigenfrequency) corresponds to a broad minimum and a large phase space volume attracting particles. Among all normal modes the dominant effect is due to the energetically lowest modes. The thermodynamic results from Monte Carlo simulations and the analytical theory are in reasonable agreement with each other at low temperatures, as expected. For higher temperatures anharmonic effects such as barrier heights will be equally important.

It was shown that in thermodynamic equilibrium the abundances of metastable states are much lower than observed in dusty plasma experiments at the same temperature. The reason is that, in equilibrium, the particles are given infinitely long time to escape a local potential minimum and they will always visit the ground state more frequently than any metastable state. In contrast, in the limit of strong damping the particles are being trapped in the first minimum they visit. Thus the decision about the final stationary state is made early during the cooling process, when the temperature is of the order of two to three times the melting temperature. Therefore, equilibrium theories without dissipation may be successfully applied to strongly correlated and strongly damped nonequilibrium systems. A systematic derivation from a time-dependent theory is still lacking and will be subject of further analysis.

7. Modification of eigenfrequency spectrum in the presence of friction

7.1. Introduction

In dusty plasma experiments the dust particles are subject to friction with the ambient neutral gas. From the simple theory of a damped harmonic oscillator it is known that the oscillation frequency is changed by the friction force. The same applies to the normal modes of the dust particles. This chapter reviews the theory of normal mode oscillations and specifically studies the aspects related to damping. Furthermore the modification of the power spectrum is discussed.

7.2. Small oscillations with damping

Linearized equation of motion

The starting point is the linearization of the equation of motion[1]

$$m\ddot{\mathbf{r}}_i = -\nabla_i U(\mathbf{r}_1, ..., \mathbf{r}_N) - \nu m\dot{\mathbf{r}}_i \tag{7.1}$$

around the equilibrium positions $\mathbf{r}_i^0$ according to $\mathbf{r}_i(t) = \mathbf{r}_i^0 + \delta\mathbf{r}_i(t)$. The potential energy U, which includes the external potential and the particle interaction, is approximated by its Taylor expansion up to second order, cf. Eq. (6.3). For the component α of the displacement vector $\delta\mathbf{r}_i(t)$ this yields the equation of motion

$$\delta\ddot{\mathbf{r}}_{i,\alpha} + \nu\delta\dot{\mathbf{r}}_{i,\alpha} + m^{-1}\sum_{j=1}^{N}\sum_{\beta=1}^{3}\left.\frac{\partial^2 U(\mathbf{r})}{\partial\mathbf{r}_{i,\alpha}\partial\mathbf{r}_{j,\beta}}\right|_{\mathbf{r}=\mathbf{r}^0}\delta\mathbf{r}_{j,\beta} = 0, \tag{7.2}$$

which comprises a set of coupled linear differential equations for the $\{\delta\mathbf{r}_i(t)\}$. As in Section 6.5.1, $\mathbf{r}^0 = (\mathbf{r}_1^0, \ldots, \mathbf{r}_N^0)$ denotes the vector of the particles' equilibrium positions.

[1] This procedure can be found in any textbook on Classical Mechanics, e.g. Ref. [50]

Eigenfrequencies

One now searches for solutions of the form $\delta\mathbf{r}_i(t) \sim \mathbf{A}_i e^{-i\lambda t}$. Inserting this ansatz into Eq. (7.2) yields a homogeneous system of linear equations for the coefficients $\mathbf{A}_i$,

$$\underbrace{\left[\frac{U_{(i\alpha),(j\beta)}}{m} - (\lambda^2 + i\nu\lambda)\delta_{(i\alpha),(j\beta)}\right]}_{M_{(i\alpha),(j\beta)}} \mathbf{A}_{j,\beta} = 0, \tag{7.3}$$

with the unknown 'eigenfrequencies' λ, see also Ref. [89]. The summation over the repeated pair of indices j, β is assumed. Recall the definition of the Hessian matrix

$$U_{(i\alpha),(j\beta)} = \left.\frac{\partial^2 U(\mathbf{r})}{\partial\mathbf{r}_{i,\alpha}\partial\mathbf{r}_{j,\beta}}\right|_{\mathbf{r}=\mathbf{r}^0}. \tag{7.4}$$

The existence of a non-trivial solution requires the vanishing of the determinant of the system's matrix $M_{(i\alpha),(j\beta)}$. Basically it is the Hessian matrix (7.4) with a prefactor m^{-1} and the additional term $-(\lambda^2 + i\nu\lambda)$ on the diagonal. This yields the condition for the new 'eigenfrequencies' λ,

$$\det\left[\frac{U_{(i\alpha),(j\beta)}}{m} - (\lambda^2 + i\nu\lambda)\delta_{(i\alpha),(j\beta)}\right] = 0. \tag{7.5}$$

By making the substitution $\omega^2 = \lambda^2 + i\nu\lambda$ one can derive a relation between the eigenfrequencies with and without dissipation. One has $\omega^2 \geq 0$ since $\mathbf{r}_0$ is chosen to be a stable local minimum. This yields

$$\det\left[\frac{U_{(i\alpha),(j\beta)}}{m} - \omega^2\delta_{(i\alpha),(j\beta)}\right] = 0. \tag{7.6}$$

Eq. (7.6) is simply the equation for the eigenfrequencies ω of the *undamped* system as in Section 6.5.1. Thus the eigenfrequencies in a damped system are related to those in an undamped system by

$$\lambda = -\frac{i\nu}{2} \pm \sqrt{\omega^2 - \left(\frac{\nu}{2}\right)^2}. \tag{7.7}$$

Solution

If all eigenfrequencies of the undamped system are different (non-degenerate), the general solution is a superposition of $3N$ damped normal modes. The eigenvectors $\mathbf{Q}_i = (\mathbf{A}_1^i, \ldots, \mathbf{A}_N^i)$, $i \in \{1, \ldots, 3N\}$, are the same as in the undamped case since they are the solutions of Eq. (7.3), which has exactly the same coefficient matrix as the undamped system if $\omega^2 = \lambda^2 + i\nu\lambda$ is substituted. Since the Hessian matrix is symmetric, eigenvectors $\mathbf{Q}_i$ corresponding to different eigenfrequencies ω_i are orthogonal.

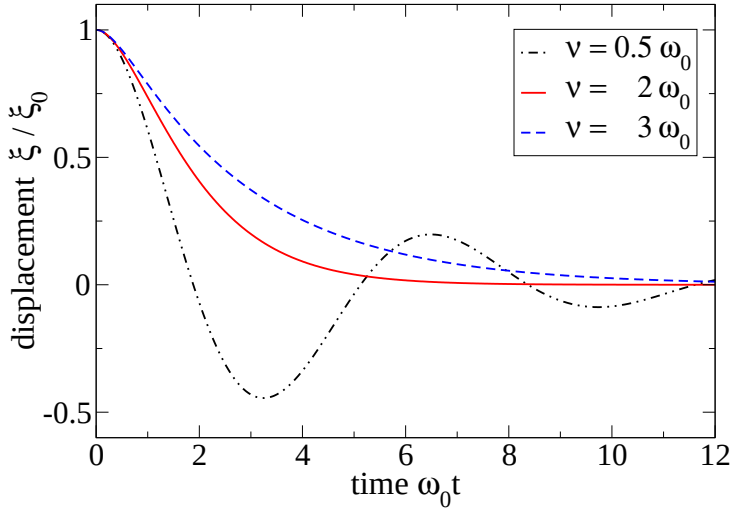

Figure 7.1.: *Trajectories of a damped harmonic oscillator with eigenfrequency ω_0 for different ν. The initial conditions are $\xi(0) = \xi_0$ and $\dot{\xi}(0) = 0$.*

Now let $\delta\mathbf{R}_i(t) = (\delta\mathbf{r}_1^i(t), \ldots, \delta\mathbf{r}_N^i(t))$ denote the normal mode $i \in \{1, \ldots, 3N\}$ and $\mathbf{q}_i = (\mathbf{a}_1^i, \ldots, \mathbf{a}_N^i)$ the orthonormal basis vectors, where $\mathbf{q}_i$ corresponds to the eigenfrequency ω_i. The general solution of Eq. (7.2) can be written as

$$\delta\mathbf{R}(t) = \sum_{i=1}^{3N} \delta\mathbf{R}_i(t) = \sum_{i=1}^{3N} \xi_i(t)\mathbf{q}_i, \tag{7.8}$$

where the $\{\xi_i(t)\}$ denote the normal coordinates. In this system of coordinates the equations of motion (7.2) are decoupled and read

$$\ddot{\xi}_i + \nu\dot{\xi}_i + \omega_i^2\xi_i = 0, \tag{7.9}$$

i.e. each eigenmode separately obeys the equation of motion of a damped harmonic oscillator.

There are three kinds of solutions, see Fig. 7.1. In the following the constants a_i, b_i must be chosen to match the initial conditions.

- $\nu < 2\,\omega_i$ (underdamping):

  $$\xi_i(t) = e^{-\nu t/2}\left[a_i \sin\tilde{\omega}_i t + b_i \cos\tilde{\omega}_i t\right]$$

  The oscillations are damped with a factor $e^{-\nu t/2}$ and have an oscillatory part with a frequency $\tilde{\omega}_i = \sqrt{\omega_i^2 - \left(\frac{\nu}{2}\right)^2}$. For very small damping, $\nu \ll \omega_i$, the frequency changes only slightly and is given by $\tilde{\omega}_i \approx \omega_i\left[1 - \frac{1}{8}\left(\frac{\nu}{\omega_i}\right)^2\right]$.

- $\nu = 2\,\omega_i$ (critical damping):

$$\xi_i(t) = e^{-\nu t/2}\,[a_i + b_i t] = e^{-\omega_i t}\,[a_i + b_i t]$$

The square root term in Eq. (7.7) vanishes and oscillatory particle motion is effectively suppressed. The displacement readily goes to zero.

- $\nu > 2\,\omega_i$ (overdamping):

$$\xi_i(t) = e^{-\nu t/2}\left[a_i e^{-\tilde{\lambda} t} + b_i e^{\tilde{\lambda} t}\right]$$

The square root term becomes imaginary which makes the particle motion non-oscillatory as in the previous case. Here $\tilde{\lambda} = \sqrt{\left(\frac{\nu}{2}\right)^2 - \omega_i^2}$. The amplitude only slowly goes to zero for $t \to \infty$, which is due to the second term where the 'decay constant' is $-\nu/2 + \tilde{\lambda} \approx -\omega_i^2/\nu$ for $\nu \gg \omega_i$.

7.3. Power spectrum

For undamped systems the spectrum of the eigenmodes shows sharp peaks at the eigenfrequencies since the motion is strictly sinusoidal. In damped systems the spectrum is altered in two ways:

- Line broadening occurs due to damping and consequently the non-periodic motion.
- The maximum of the power spectrum is shifted to a lower $\omega_{\max}$ due to the friction force. This is especially apparent for the underdamped case where the sinusoidal part has a shifted frequency of $\tilde{\omega}_i = \sqrt{\omega_i^2 - \left(\frac{\nu}{2}\right)^2}$.

The spectrum will be studied by starting from the uncoupled equations of motion for the damped eigenmodes,

$$\ddot{\xi}_i + \nu\dot{\xi}_i + \omega_i^2 \xi_i = 0. \tag{7.10}$$

In the following the index i will be dropped and the eigenfrequencies will be denoted by $\omega_i \equiv \omega_0$.

The goal is to calculate the quantity

$$\tilde{\xi}(T,\omega) = \int_0^T \xi(t) e^{-i\omega t} dt, \tag{7.11}$$

which is essentially the Fourier transform of $\xi(t)$ for $T \to \infty$. The lower integration limit is chosen as $t_0 = 0$ since $\xi(t) \equiv 0$ for $t < 0$.

The transformation (7.11) is applied to the equation of motion (7.10). Thereby one has to solve the integrals

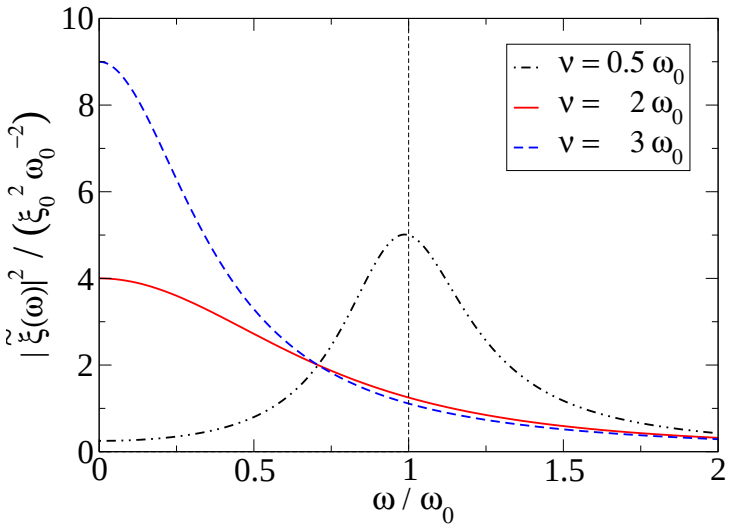

Figure 7.2.: *Power spectrum (7.16) of the damped oscillator for different ν. The initial conditions are $\xi(0) = \xi_0$ and $\dot{\xi}(0) = 0$.*

$$\int_0^T \dot{\xi}(t) e^{-i\omega t} dt = \xi(T) e^{-i\omega T} - \xi_0 + i\omega \tilde{\xi}(T,\omega), \tag{7.12}$$

$$\int_0^T \ddot{\xi}(t) e^{-i\omega t} dt = \dot{\xi}(T) e^{-i\omega T} - \dot{\xi}_0 + i\omega \int_0^T \dot{\xi}(t) e^{-i\omega t} dt, \tag{7.13}$$

which is easily achieved by integration by parts. Here the abbreviations $\xi(0) = \xi_0$ and $\dot{\xi}(0) = \dot{\xi}_0$ are used to denote the initial conditions. Collecting terms one arrives at

$$\tilde{\xi}(T,\omega) = \frac{\dot{\xi}_0 + \xi_0[\nu + i\omega] - \left[\dot{\xi}(T) + \xi(T)[\nu + i\omega]\right] e^{-i\omega T}}{(\omega_0^2 - \omega^2) + i\nu\omega}. \tag{7.14}$$

In the limit $T \to \infty$ one has $\xi(T) \to 0$, $\dot{\xi}(T) \to 0$ and the result reduces to

$$\tilde{\xi}(T \to \infty, \omega) \equiv \tilde{\xi}(\omega) = \frac{\dot{\xi}_0 + \xi_0[\nu + i\omega]}{(\omega_0^2 - \omega^2) + i\nu\omega}. \tag{7.15}$$

The spectral power density is then given by

$$|\tilde{\xi}(\omega)|^2 = \frac{\left[\dot{\xi}_0 + \nu\xi_0\right]^2 + \omega^2\xi_0^2}{(\omega_0^2 - \omega^2)^2 + \nu^2\omega^2}. \tag{7.16}$$

For large ω one calculates the asymptote $|\tilde{\xi}(\omega)|^2 \sim \xi_0^2/\omega^2$.

In contrast to the undamped case where the spectrum is peaked at a single frequency ω_0 [for a continuous signal $\xi(t) \sim \sin(\omega_0 t)$, $t \in (-\infty, \infty)$], the power density of a damped signal shows line broadening and a shifted maximum at

$$\omega_{\max} = \left[\sqrt{(z_0^2 + \nu z_0 + \omega_0^2)(z_0^2 + 3\nu z_0 + 2\nu^2 + \omega_0^2)} - (z_0 + \nu)^2 \right]^{1/2},$$

where $z_0 = \dot{\xi}_0/\xi_0$. The maximum vanishes (i.e. it becomes a maximum at $\omega = 0$) at some critical value ν_{crit} as ν is increased.

The spectrum is shown in Fig. 7.2 for different ν with the initial condition $\dot{\xi}_0 = 0$. In this particular example the maximum is located at

$$\omega_{\max} = \sqrt{\omega_0 \sqrt{2\nu^2 + \omega_0^2} - \nu^2}$$

and vanishes at $\nu_{\text{crit}} = \sqrt{1 + \sqrt{2}}\,\omega_0 \approx 1.55\,\omega_0$, i.e. even before the system is overdamped.

7.4. Discussion

In the strong damping regime, as is the case in the experiments on spherical Yukawa balls, many eigenmodes will 'vanish' because the friction coefficient is too large. For $\nu \geq 2\,\omega_i$ the eigenfrequencies (7.7) become purely imaginary and the motion is overdamped so any kind of periodic motion is suppressed.

As one can see in Fig. 6.7, showing a typical spectrum with experimentally relevant parameters, only a few modes will actually be in the underdamped regime, since ν is typically of the order $3 \ldots 6$ (in units of the trap frequency). This is why it would be difficult to examine and study the eigenfrequency spectrum in these systems. In addition the maximum of the power spectrum for the eigenmodes can vanish even before the mode is overdamped and this particular feature of the signal is lost.

8. Summary and outlook

8.1. Summary of the work

This work was concerned with classical, strongly correlated finite systems in external traps and their static and dynamic properties.

After a discussion of some of the aspects related to strongly coupled Coulomb systems, the focus was laid on dusty plasmas, especially so-called Yukawa balls. The model for the theoretical description in this work was based on a spherical harmonic confinement and a statically screened Coulomb potential for the particle interaction. Next, molecular dynamics, Langevin dynamics and Monte Carlo simulation methods were introduced as the required tools for studying the model system.

The first aspect was the investigation of an improved shell model for Yukawa balls. There the ground states were found by the method of simulated annealing using a Metropolis Monte Carlo procedure. A fit parameter in the model was determined to match the exact ground state energies found in MD simulations. It was shown that for low screening the occupation numbers in the shell model were comparable to the exact results, but showed substantial deviations for larger screening and higher particle numbers. The radii could be reproduced with a good accuracy, except for the innermost shell. An improvement was possible by allowing for different correlation parameters for different shells. Here the occupation numbers and radii are well predicted for larger clusters, but the energy deviates from the exact value.

Molecular dynamics and Langevin dynamics simulations were used to investigate the occurrence probabilities of Yukawa balls in damped systems. It was found that the damping strength strongly influences the abundances of metastable states. While slow cooling generally leads to a high probability of the ground state, strong friction is responsible for the high abundances of metastable states in dusty plasma experiments. The screening parameter, and thus the range of the interaction potential, strongly affects the shell occupation. In Coulomb systems with long range interaction, states with only a few particles on the inner shells have a high probability. The probability of states that have more particles on the inner shell was shown to increase with the screening parameter. A physically intuitive explanation for the probabilities was given in terms of a simple model based on the canonical partition function. The temperature dependent results from this model were compared to exact Monte Carlo simulations and reasonable agreement was found for low temperatures. The application of the equilibrium model to the nonequilibrium process that leads to the formation of a Yukawa ball was achieved by considering the time evolution of the velocity distribution function. It readily relaxes

towards a Maxwellian distribution during the cooling process and thus local thermodynamic equilibrium. In this case the analytical theory is applicable and the probabilities are determined when the particles have a temperature around the melting point.

In the last part of this work the eigenmodes of damped systems were investigated. After a review of the relevant theory the power spectrum of damped oscillations was derived and the influence of friction was demonstrated. Damping was shown to lead to line broadening and a shift of the maximum in the power spectrum. The maximum can vanish even before the system is in the overdamped regime.

8.2. Outlook

Several aspects of this work could be improved or extended.

The correlation term in the Yukawa shell model has been added without a rigorous derivation – only based on the analogy with the Coulomb model. The primary goal of future analysis should be to derive an energy expression for a shell model with Yukawa interaction without making further assumptions regarding the correlation energy. Even though the form of the correlation term is well justified for Coulomb interaction, as was shown in Ref. [75], this is not necessarily the case for the Yukawa potential. As already mentioned the cohesive (correlation) energy of a two-dimensional Yukawa lattice could be used to approximate the correlation energy in the present shell model [76].

An improvement of the analytical model for the probability of stationary states is possible by including anharmonic effects, as was done in Ref. [78] by allowing for temperature dependent eigenfrequencies. An alternative approach taken by Schweigert and Peeters [81] changes the limits of allowed particle motion in the integration of the partition function. However, both methods require additional parameters such as a measure of the anharmonicity or the barrier heights between different states.

Another possible extension of the present work is further analysis of the time evolution of the distribution function (short-time behavior) during the cooling process. This would be possible by means of a Fokker Planck equation that directly takes into account the effect of the confinement potential and the particle interaction. In this framework it should be possible to directly study the relaxation processes and further determine the relevant time scales of the dynamics. The Fokker Planck equation directly yields the relevant ensemble averages.

The theoretical model system could be improved by means of *dynamically* shielded pair potentials. These potentials take into account the effects of external fields on the ion (and electron) distribution functions which determine the effective interaction between the dust grains. In the presence of an electric field, as encountered in the sheath region above the lower electrode in dusty plasma experiments, there is a strong downward ion flow. This makes the potential anisotropic and the dynamics of the dust particles becomes non-Newtonian (non-reciprocal forces). With these methods it would be possible to further account for the surrounding plasma environment and include

several new effects such as Landau damping or ion-neutral collisions, which are missing in the present model.

A. Calculation of shell radii for Yukawa interaction

The shell radii $\{R_\nu\}$ in the Yukawa shell model must be determined from the system of equations (5.7). Explicitly, the equations are given by (after rearrangement of terms)

$$\begin{aligned} & 2\left(\frac{R_\nu}{r_0}\right)^3 - e^{-\kappa R_\nu}\left[\left(\frac{N_\nu - \epsilon_\nu(N,\kappa)\sqrt{N_\nu}}{2}\right)\left(\sinh(\kappa R_\nu)\left(1+\frac{2}{\kappa R_\nu}\right) - \cosh(\kappa R_\nu)\right)\right. \\ & \left. + (1+\kappa R_\nu)\left(\xi + \sum_{\mu<\nu} N_\mu \frac{\sinh(\kappa R_\mu)}{\kappa R_\mu}\right)\right] \\ & + [\cosh(\kappa R_\nu)\kappa R_\nu - \sinh(\kappa R_\nu)] \sum_{\mu=\nu+1}^{L} N_\mu \frac{e^{-\kappa R_\mu}}{\kappa R_\mu} = 0. \end{aligned} \tag{A.1}$$

Here the number of shells is denoted by L and $\nu \in \{1, \ldots, L\}$. This system of coupled nonlinear equations can be solved with the Newton-Raphson method [51].

The equations (A.1) have the form

$$F_\nu(R_1, \ldots, R_L) = 0, \qquad \nu \in \{1, \ldots, L\}.$$

Now let $\mathbf{F} = (F_1, \ldots, F_L)$ denote the vector of the functions $\{F_\nu\}$ and let $\mathbf{R} = (R_1, \ldots, R_L)$ be an initial 'guess' of the solution. In the local neighborhood of the point $\mathbf{R}$ one can expand $\mathbf{F}$ in a Taylor series according to

$$\mathbf{F}(\mathbf{R} + \delta\mathbf{R}) \approx \mathbf{F}(\mathbf{R}) + J \cdot \delta\mathbf{R} + \mathcal{O}(\delta\mathbf{R}^2).$$

Here J denotes the Jacobian matrix

$$J = \frac{\partial F_\nu}{\partial R_\mu}, \qquad \nu, \mu \in \{1, \ldots, L\},$$

that contains the partial derivatives of $\mathbf{F}$. Terms of higher than linear order in $\delta\mathbf{R}$ are neglected. The idea is to solve

$$\begin{aligned} & \mathbf{F}(\mathbf{R} + \delta\mathbf{R}) &&= 0 \\ \Longleftrightarrow \qquad & J \cdot \delta\mathbf{R} &&= -\mathbf{F}, \end{aligned} \tag{A.2}$$

for the correction $\delta\mathbf{R}$ to the initial guess of the solution. Eq. (A.2) is only a system of

linear equations which can be solved by Gaussian elimination. The corrected solution is then given by $\mathbf{R}_{\mathrm{corr}} = \mathbf{R} + \delta\mathbf{R}$. Depending on the initial value of the solution vector the procedure has to be repeated several times to obtain the solution with a certain degree of accuracy.

The convergence of the iteration procedure is only guaranteed if the initial guess of the solution is sufficiently close to the exact solution. This is not a problem here since the radii for Coulomb interaction are known analytically [Eq. (5.8)] and change only slightly in the case of Yukawa interaction and low screening. Thus one can choose the Coulomb radii as the initial values to get an accurate starting point. The convergence of the method can further be improved by rescaling the Coulomb radii by a factor $s < 1$ to account for the smaller radii in the Yukawa model.

B. Derivation of partition function

The first step in evaluating the partition function in the harmonic approximation is to write down the Hamiltonian for each energy contribution. Thereby one has to choose appropriate generalized coordinates. In the following the 's', denoting the local minimum, will be dropped for simplicity, but one has to keep in mind that the chosen coordinates are specific for each state.

For the vibrational part the normal coordinates ξ_i are chosen as generalized coordinates [78]. Then the Hamiltonian takes the well known form of f decoupled harmonic oscillators and reads

$$H^{\mathrm{vib}}(\xi_i, p_{\xi_i}) = \sum_{i=1}^{f} \left\{ \frac{p_{\xi_i}^2}{2m} + \frac{m}{2}\omega_i^2 \xi_i^2 \right\}. \tag{B.1}$$

Here the p_{ξ_i} are the conjugate momenta of the coordinates ξ_i.

The corresponding part of the partition function can now be evaluated. The integrals are all of the Gaussian type $\int_{-\infty}^{\infty} e^{-a^2x^2} dx = \frac{\sqrt{\pi}}{a}$ and one obtains from (6.6)

$$\begin{aligned} Z^{\mathrm{vib}} &= \frac{1}{(2\pi\hbar)^f} \prod_{i=1}^{f} \int_{-\infty}^{\infty} \exp\left[-\left(\frac{p_{\xi_i}^2}{2m} + \frac{1}{2} m\omega_i^2 \xi_i^2 \right) / k_B T \right] dp_{\xi_i}\, d\xi_i \\ &= \prod_{i=1}^{f} \frac{k_B T}{\hbar\omega_i} = \left(\frac{k_B T}{\hbar\Omega} \right)^f, \end{aligned}$$

where $\Omega = \left(\prod_{i=1}^{f} \omega_i \right)^{1/f}$ is the mean geometric eigenfrequency.
The evaluation of the rotational part is more involved [80]. Here one chooses the Euler angles θ, ϕ, ψ as the generalized coordinates. For this choice of coordinates and with the principal moments of inertia I_1, I_2, I_3 the Lagrangian for a rigid rotator only consists of kinetic energy and reads

$$L^{\mathrm{rot}}(\phi, \theta, \psi, \dot{\phi}, \dot{\theta}, \dot{\psi}) = \frac{L_1^2}{2I_1} + \frac{L_2^2}{2I_2} + \frac{L_3^2}{2I_3}. \tag{B.2}$$

The L_1, L_2, L_3 denote the angular momenta with respect to the associated principal

axes. In terms of the Euler angles they can be written as

$$\begin{aligned} L_1 &= I_1(\dot{\phi}\sin\theta\sin\psi + \dot{\theta}\cos\psi) \\ L_2 &= I_2(\dot{\phi}\sin\theta\cos\psi - \dot{\theta}\sin\psi) \\ L_3 &= I_3(\dot{\phi}\cos\theta + \dot{\psi}). \end{aligned} \tag{B.3}$$

The conjugate momenta can easily be calculated according to

$$\begin{aligned} p_\phi &= \frac{\partial L^{\mathrm{rot}}}{\partial\dot{\phi}} = L_1\sin\theta\sin\psi + L_2\sin\theta\cos\psi + L_3\cos\theta \\ p_\theta &= \frac{\partial L^{\mathrm{rot}}}{\partial\dot{\theta}} = L_1\cos\psi - L_2\sin\psi \\ p_\psi &= \frac{\partial L^{\mathrm{rot}}}{\partial\dot{\psi}} = L_3. \end{aligned} \tag{B.4}$$

To get the Hamiltonian one has to perform the Legendre transformation $H^{\mathrm{rot}} = p_\phi\dot{\phi} + p_\theta\dot{\theta} + p_\psi\dot{\psi} - L^{rot}$ and write the $\dot{\phi}, \dot{\theta}, \dot{\psi}$ in terms of the generalized coordinates and their conjugate momenta. In the case of a rigid rotator the Hamiltonian and the Lagrangian are the same [80]. Thus one can directly proceed to the evaluation of the partition function

$$\begin{aligned} Z^{\mathrm{rot}} &= \frac{1}{(2\pi\hbar)^3}\int e^{-\beta H^{rot}}\,d\phi\,d\theta\,d\psi\,dp_\phi\,dp_\theta\,dp_\psi \\ &= \frac{1}{(2\pi\hbar)^3}\int e^{-\beta H^{rot}}\left|J\left(\frac{p_\phi,p_\theta,p_\psi}{L_1,L_2,L_3}\right)\right|d\phi\,d\theta\,d\psi\,dL_1\,dL_2\,dL_3 \\ &= \frac{1}{(2\pi\hbar)^3}\int_0^{2\pi}d\phi\int_0^{\pi}\sin\theta d\theta\int_0^{2\pi}d\psi\int_{-\infty}^{\infty}\exp\left(-\frac{L_1^2}{2I_1k_BT}\right)dL_1 \\ &\quad\times\int_{-\infty}^{\infty}\exp\left(-\frac{L_2^2}{2I_2k_BT}\right)dL_2\int_{-\infty}^{\infty}\exp\left(-\frac{L_3^2}{2I_3k_BT}\right)dL_3. \end{aligned} \tag{B.5}$$

In the second line of Eq. (B.5) $\left|J\left(\frac{p_\phi,p_\theta,p_\psi}{L_1,L_2,L_3}\right)\right|$ denotes the determinant of the Jacobian matrix of the transformation (B.4). The remaining integrals can easily be solved and give the final result

$$Z^{\mathrm{rot}} = \left(\frac{2\pi^{1/3}k_BT\bar{I}}{\hbar^2}\right)^{3/2}, \tag{B.6}$$

where $\bar{I} = (I_1I_2I_3)^{1/3}$ denotes the mean geometric moment of inertia.

C. Publications

- H. Baumgartner, H. Kählert, V. Golobnychiy, C. Henning, S. Käding, A. Melzer, and M. Bonitz, *Shell Structure of Yukawa Balls*, Contributions to Plasma Physics **47**, 281 (2007)
- S. Käding, D. Block, A. Melzer, A. Piel, H. Kählert, P. Ludwig, and M. Bonitz, *Shell transitions between metastable states of Yukawa balls*, Physics of Plasmas **15**, 073710 (2008).
- H. Baumgartner, D. Asmus, V. Golubnychiy, P. Ludwig, H. Kählert, and M. Bonitz, *Ground state of finite spherical Yukawa crystals*, New Journal of Physics **10**, 093019 (2008)
- H. Kählert, P. Ludwig, H. Baumgartner, M. Bonitz, D. Block, S. Käding, A. Melzer, and A. Piel, *Probability of metastable states in spherical three-dimensional Yukawa crystals*, Physical Review E **78**, 036408 (2008)

References

[1] O. Arp, D. Block, A. Piel, and A. Melzer, *Dust Coulomb Balls: Three-Dimensional Plasma Crystals*, Physical Review Letters **93**, 165004 (2004)

[2] C. Henning, H. Baumgartner, A. Piel, P. Ludwig, V. Golubnichiy, M. Bonitz, and D. Block, *Ground state of a confined Yukawa plasma*, Physical Review E **74**, 056403 (2006)

[3] D. Block, S. Käding, A. Melzer, A. Piel, H. Baumgartner, and M. Bonitz, *Experiments on metastable states of three-dimensional trapped particle clusters*, Physics of Plasmas **15**, 040701 (2008)

[4] V. Fortov, I. Iakubov, and A. Khrapak, *Physics of Strongly Coupled Plasma* (Oxford University Press, New York, 2006)

[5] S. Hamaguchi, R. T. Farouki, and D. H. E. Dubin, *Triple point of Yukawa systems*, Physical Review E **56**, 4671 (1997)

[6] P. Hartmann, G. J. Kalman, Z. Donkó, and K. Kutasi, *Equilibrium properties and phase diagram of two-dimensional Yukawa systems*, Physical Review E **72**, 026409 (2005)

[7] M. Bonitz, P. Ludwig, H. Baumgartner, C. Henning, A. Filinov, D. Block, O. Arp, A. Piel, S. Käding, Y. Ivanov, et al., *Classical and quantum Coulomb crystals*, Physics of Plasmas **15**, 055704 (2008)

[8] E. Wigner, *On the Interaction of Electrons in Metals*, Physical Review **46**, 1002 (1934)

[9] D. J. Wineland, J. C. Bergquist, W. M. Itano, J. J. Bollinger, and C. H. Manney, *Atomic-Ion Coulomb Clusters in an Ion Trap*, Physical Review Letters **59**, 2935 (1987)

[10] M. Drewsen, C. Brodersen, L. Hornekær, J. S. Hangst, and J. P. Schiffer, *Large Ion Crystals in a Linear Paul Trap*, Physical Review Letters **81**, 2878 (1998)

[11] A. V. Filinov, M. Bonitz, and Y. E. Lozovik, *Wigner Crystallization in Mesoscopic 2D Electron Systems*, Physical Review Letters **86**, 3851 (2001)

[12] P. Ludwig, A. Filinov, M. Bonitz, and Y. Lozovik, *Ground state and structural transitions in mesoscopic electron hole bilayers*, Contributions to Plasma Physics **43**, 285 (2003)

[13] C. K. Goertz, *Dusty Plasmas in the Solar System*, Reviews of Geophysics **27**, 271 (1989)

[14] F. Verheest, *Waves and instabilities in dusty space plasmas*, Space Science Reviews **77**, 267 (1996)

[15] H. Ikezi, *Coulomb solid of small particles in plasmas*, Physics of Fluids **29**, 1764 (1986)

[16] J. H. Chu and L. I, *Direct observation of Coulomb crystals and liquids in strongly coupled rf dusty plasmas*, Physical Review Letters **72**, 4009 (1994)

[17] H. Thomas, G. E. Morfill, V. Demmel, J. Goree, B. Feuerbacher, and D. Möhlmann, *Plasma Crystal: Coulomb Crystallization in a Dusty Plasma*, Physical Review Letters **73**, 652 (1994)

[18] A. Melzer, T. Trottenberg, and A. Piel, *Experimental determination of the charge on dust particles forming Coulomb lattices*, Physics Letters A **191**, 301 (1994)

[19] G. Morfill, V. Tsytovich, and H. Thomas, *Complex plasmas: II. Elementary processes in complex plasmas*, Plasma Physics Reports **29**, 1 (2003)

[20] J. Goree, *Charging of particles in a plasma*, Plasma Sources Science and Technology **3**, 400 (1994)

[21] H. Löwen, *Kolloide–auch fur Physiker interessant*, Physikalische Blätter **51**, 165 (1995)

[22] P. K. Shukla and N. N. Rao, *Coulomb crystallization in colloidal plasmas with streaming ions and dust grains*, Physics of Plasmas **3**, 1770 (1996)

[23] G. Joyce, M. Lampe, and G. Ganguli, *Instability-Triggered Phase Transition to a Dusty-Plasma Condensate*, Physical Review Letters **88**, 095006 (2002)

[24] D. Tskhakaya and P. Shukla, *Theory of dust crystal and its oscillations in plasmas*, Physics Letters A **286**, 277 (2001)

[25] O. Arp, D. Block, M. Klindworth, and A. Piel, *Confinement of Coulomb balls*, Physics of Plasmas **12**, 122102 (2005)

[26] K. Takahashi, T. Oishi, K.-i. Shimomai, Y. Hayashi, and S. Nishino, *Analyses of attractive forces between particles in Coulomb crystal of dusty plasmas by optical manipulations*, Physical Review E **58**, 7805 (1998)

[27] G. E. Morfill, H. M. Thomas, U. Konopka, H. Rothermel, M. Zuzic, A. Ivlev, and J. Goree, *Condensed Plasmas under Microgravity*, Physical Review Letters **83**, 1598 (1999)

[28] H. Rothermel, T. Hagl, G. E. Morfill, M. H. Thoma, and H. M. Thomas, *Gravity Compensation in Complex Plasmas by Application of a Temperature Gradient*, Physical Review Letters **89**, 175001 (2002)

[29] M. Bonitz, D. Block, O. Arp, V. Golubnychiy, H. Baumgartner, P. Ludwig, A. Piel, and A. Filinov, *Structural Properties of Screened Coulomb Balls*, Physical Review Letters **96**, 075001 (2006)

[30] P. Ludwig, S. Kosse, and M. Bonitz, *Structure of spherical three-dimensional Coulomb crystals*, Physical Review E **71**, 046403 (2005)

[31] O. Arp, D. Block, M. Bonitz, H. Fehske, V. Golubnychiy, S. Kosse, P. Ludwig, A. Melzer, and A. Piel, *3D Coulomb balls: experiment and simulation*, Journal of Physics: Conference Series **11**, 234 (2005)

[32] S. W. S. Apolinario, B. Partoens, and F. M. Peeters, *Structural and dynamical aspects of small three-dimensional spherical Coulomb clusters*, New Journal of Physics **9**, 283 (2007)

[33] H. Baumgartner, D. Asmus, V. Golubnychiy, P. Ludwig, H. Kählert, and M. Bonitz, *Ground states of finite spherical Yukawa crystals*, New Journal of Physics **10**, 093019 (2008)

[34] H. Baumgartner, *Monte-Carlo Simulation von Coulomb balls* (diploma thesis, University of Kiel, 2006)

[35] O. S. Vaulina and S. A. Khrapak, *Scaling Law for the Fluid-Solid Phase Transition in Yukawa Systems (Dusty Plasmas)*, Soviet Journal of Experimental and Theoretical Physics **90**, 287 (2000)

[36] S. W. S. Apolinario and F. M. Peeters, *Melting transitions in isotropically confined three-dimensional small Coulomb clusters*, Physical Review E **76**, 031107 (2007)

[37] S. W. S. Apolinario and F. M. Peeters, *Melting of anisotropically confined Coulomb balls*, Physical Review B **78**, 024202 (2008)

[38] C. Henning, P. Ludwig, A. Filinov, A. Piel, and M. Bonitz, *Ground state of a confined Yukawa plasma including correlation effects*, Physical Review E **76**, 036404 (2007)

[39] D. Wales and J. Doye, *Global Optimization by Basin-Hopping and the Lowest Energy Structures of Lennard-Jones Clusters Containing up to 110 Atoms*, Journal of Physical Chemistry A **101**, 5111 (1997)

[40] T. Fließbach, *Lehrbuch zur Theoretischen Physik: Statistische Physik* (Spektrum Akademischer Verlag, Heidelberg, Berlin, 2006)

[41] D. Rapaport, *The Art of Molecular Dynamics Simulation* (Cambridge University Press, 2004)

[42] K. Binder, *Computersimulationen*, Physik Journal **3**, 25 (2004)

[43] Z. Donkó, J. Goree, P. Hartmann, and K. Kutasi, *Shear Viscosity and Shear Thinning in Two-Dimensional Yukawa Liquids*, Physical Review Letters **96**, 145003 (2006)

[44] T. Ott, M. Bonitz, Z. Donkó, and P. Hartmann, *Superdiffusion in quasi-two-dimensional Yukawa liquids*, Physical Review E **78**, 026409 (2008)

[45] M. Sekine, K. Yasuoka, T. Kinjo, and M. Matsumoto, *Liquid–vapor nucleation simulation of Lennard-Jones fluid by molecular dynamics method*, Fluid Dynamics Research **40**, 597 (2008)

[46] M. Karplus and J. Kuriyan, *Chemical Theory and Computation Special Feature: Molecular dynamics and protein function*, Proceedings of the National Academy of Sciences **102**, 6679 (2005)

[47] J. Kohanoff and J.-P. Hansen, *Statistical properties of the dense hydrogen plasma: An ab initio molecular dynamics investigation*, Physical Review E **54**, 768 (1996)

[48] P. Hartmann, Z. Donko, P. Bakshi, G. Kalman, and S. Kyrkos, *Molecular Dynamics Studies of Solid–Liquid Phase Transition in 2-D Yukawa Systems*, IEEE Transactions on Plasma Science **35**, 332 (2007)

[49] A. V. Filinov, V. O. Golubnychiy, M. Bonitz, W. Ebeling, and J. W. Dufty, *Temperature-dependent quantum pair potentials and their application to dense partially ionized hydrogen plasmas*, Physical Review E **70**, 046411 (2004)

[50] T. Fließbach, *Lehrbuch zur Theoretischen Physik: Mechanik* (Spektrum Akademischer Verlag, Heidelberg, Berlin, 2006)

[51] W. Press, B. Flannery, S. Teukolsky, and W. Vetterling, *Numerical recipes* (Cambridge University Press, New York, 1986)

[52] P. Ludwig, *Mesoskopische Exzitonencluster in gekoppelten Quantenpunkten* (diploma thesis, University of Rostock, 2003)

[53] M. Allen and D. Tildesley, *Computer Simulation of Liquids* (Oxford University Press, USA, 1989)

[54] R. Zwanzig, *Ensemble Method in the Theory of Irreversibility*, The Journal of Chemical Physics **33**, 1338 (1960)

[55] R. Zwanzig, in *Lectures in Theoretical Physics*, edited by W. Brittin (Wiley, New York, 1961)

[56] R. Zwanzig, *Memory Effects in Irreversible Thermodynamics*, Physical Review **124**, 983 (1961)

[57] H. Mori, *Transport, Collective Motion, and Brownian Motion*, Progress of Theoretical Physics **33**, 423 (1965)

[58] H. Mori, *A Continued-Fraction Representation of the Time-Correlation Functions*, Progress of Theoretical Physics **34**, 399 (1965)

[59] R. Mannella, *Quasisymplectic integrators for stochastic differential equations*, Physical Review E **69**, 041107 (2004)

[60] W. Coffey, Y. Kalmykov, and J. Waldron, *The Langevin equation* (World Scientific River Edge, New Jersey, 1996)

[61] N. Metropolis, A. W. Rosenbluth, M. N. Rosenbluth, A. H. Teller, and E. Teller, *Equation of State Calculations by Fast Computing Machines*, The Journal of Chemical Physics **21**, 1087 (1953)

[62] G. Danese, I. De Lotto, A. De Marchi, F. Leporati, T. Bellini, M. Buscaglia, and F. Mantegazza, *Monte Carlo Metropolis simulation of interacting anisotropic polarizable spins on a lattice*, Computer Physics Communications **134**, 47 (2001)

[63] S. Do Hong and M. Shik Jhon, *Calculation of excess free energy from the averaged effective acceptance ratio for the Lennard-Jones fluid and the inverse twelve fluid*, Chemical Physics Letters **273**, 79 (1997)

[64] J. Böning, A. Filinov, P. Ludwig, H. Baumgartner, M. Bonitz, and Y. Lozovik, *Melting of Trapped Few-Particle Systems*, Physical Review Letters **100**, 113401 (2008)

[65] A. Voter, in *Radiation Effects in Solids*, edited by K. Sickafus and E. Kotomin (Springer, Dordrecht, 2005)

[66] A. Filinov and M. Bonitz, in *Introduction to Computational Methods in Many-Body Physics*, edited by M. Bonitz and D. Semkat (Rinton Press, Princeton, 2006)

[67] V. S. Filinov, H. Fehske, M. Bonitz, V. E. Fortov, and P. Levashov, *Correlation effects in partially ionized mass asymmetric electron-hole plasmas*, Physical Review E **75**, 036401 (2007)

[68] A. Filinov, J. Böning, M. Bonitz, and Y. Lozovik, *Controlling the spatial distribution of superfluidity in radially ordered Coulomb clusters*, Physical Review B **77**, 214527 (2008)

[69] M. Holzmann and W. Krauth, *Kosterlitz-Thouless Transition of the Quasi-Two-Dimensional Trapped Bose Gas*, Physical Review Letters **100**, 190402 (2008)

[70] S. Kirkpatrick, C. Gelatt, and M. Vecchi, *Optimization by Simulated Annealing*, Science **220**, 671 (1983)

[71] R. W. Hasse and V. V. Avilov, *Structure and Madelung energy of spherical Coulomb crystals*, Physical Review A **44**, 4506 (1991)

[72] H. Baumgartner, H. Kählert, V. Golobnychiy, C. Henning, S. Käding, A. Melzer, and M. Bonitz, *Shell Structure of Yukawa Balls*, Contributions to Plasma Physics **47**, 281 (2007)

[73] W. Kraeft and M. Bonitz, *Thermodynamics of a Correlated Confined Plasma II. Mesoscopic System*, Journal of Physics: Conference Series **35**, 94 (2006)

[74] K. Tsuruta and S. Ichimaru, *Binding energy, microstructure, and shell model of Coulomb clusters*, Physical Review A **48**, 1339 (1993)

[75] J. Cioslowski and E. Grzebielucha, *Parameter-free shell model of spherical Coulomb crystals*, Physical Review E **78**, 026416 (2008)

[76] H. Totsuji, T. Ogawa, C. Totsuji, and K. Tsuruta, *Structure of spherical Yukawa clusters: A model for dust particles in dusty plasmas in an isotropic environment*, Physical Review E **72**, 036406 (2005)

[77] H. Kählert, P. Ludwig, H. Baumgartner, M. Bonitz, D. Block, S. Käding, A. Melzer, and A. Piel, *Probability of metastable configurations in spherical three-dimensional Yukawa crystals*, Physical Review E **78**, 036408 (2008)

[78] F. Baletto and R. Ferrando, *Structural properties of nanoclusters: Energetic, thermodynamic, and kinetic effects*, Reviews of Modern Physics **77**, 371 (2005)

[79] S. Käding, D. Block, A. Melzer, A. Piel, H. Kählert, P. Ludwig, and M. Bonitz, *Shell transitions between metastable states of Yukawa balls*, Physics of Plasmas **15**, 073710 (2008)

[80] E. Desloge, *Classical partition function of a rigid rotator*, American Journal of Physics **52**, 261 (1984)

[81] V. A. Schweigert and F. M. Peeters, *Spectral properties of classical two-dimensional clusters*, Physical Review B **51**, 7700 (1995)

[82] V. Golubnychiy, H. Baumgartner, M. Bonitz, A. Filinov, and H. Fehske, *Screened Coulomb balls, structural properties and melting behaviour*, Journal of Physics A: Mathematical and General **39**, 4527 (2006)

[83] S. W. S. Apolinario and F. M. Peeters, *Melting transitions in isotropically confined three-dimensional small Coulomb clusters*, Physical Review E **76**, 031107 (2007)

[84] M. Bonitz, *Quantum Kinetic Theory* (Teubner, Stuttgart, Leipzig, 1998)

[85] D. Semkat, D. Kremp, and M. Bonitz, *Kadanoff-Baym equations with initial correlations*, Physical Review E **59**, 1557 (1999)

[86] M. Bonitz, *Correlation time approximation in non-Markovian kinetics*, Physics Letters A **221**, 85 (1996)

[87] H. Haberland, M. Bonitz, and D. Kremp, *Harmonics generation in electron-ion collisions in a strong laser pulse*, Physical Review E **64**, 026405 (2001)

[88] D. Gericke, M. Murillo, D. Semkat, M. Bonitz, and D. Kremp, *Relaxation of strongly coupled Coulomb systems after rapid changes of the interaction potential*, Journal of Physics A: Mathematical and General **36**, 6087 (2003)

[89] G. Piacente, F. M. Peeters, and J. J. Betouras, *Normal modes of a quasi-one-dimensional multichain complex plasma*, Physical Review E **70**, 036406 (2004)